

STUDY OF SOFT MATERIALS, FLEXIBLE ELECTRONICS, AND MACHINE
LEARNING FOR FULLY PORTABLE AND WIRELESS BRAIN-MACHINE
INTERFACES

A Dissertation
Presented to
The Academic Faculty

by

Musa Mahmood

In Partial Fulfillment
of the Requirements for the Degree
Doctor of Philosophy in Bioengineering in the
George W. Woodruff School of Mechanical Engineering

Georgia Institute of Technology

December 2021

Copyright © Musa Mahmood 2021

STUDY OF SOFT MATERIALS, FLEXIBLE ELECTRONICS, AND MACHINE
LEARNING FOR FULLY PORTABLE AND WIRELESS BRAIN-MACHINE
INTERFACES

Approved by:

Dr. Woon-Hong Yeo, Advisor
School of Mechanical Engineering
Georgia Institute of Technology

Dr. Minoru Shinohara
School of Biological Sciences
Georgia Institute of Technology

Dr. Frank Hammond
School of Mechanical Engineering
Georgia Institute of Technology

Dr. Audrey Duarte
School of Psychology
University of Texas

Dr. Todd Sulchek
School of Mechanical Engineering
Georgia Institute of Technology

Date Approved: December 7, 2021

ACKNOWLEDGEMENTS

I would like to sincerely thank my thesis advisor Dr. Woon-Hong Yeo. I appreciate that he elected to work with me and provided me the freedom to explore the fields of research that I am interested in. I'd like to thank Dr. Saswat Mishra and Dr. Yongkuk Lee who introduced me to the research process and advised me early in my undergraduate studies – their mentorship was invaluable to my progress as a researcher. I'd also like to thank my colleagues, mentors and collaborators for their valuable input towards my research, including but not limited to:

Dr. Yun-Soung Kim, Dr. Hojoong Kim, Dr. Young-Tae Kwon, Dr. Hyo-Ryoung Lim, Dr. Jinwoo Lee, Dr. Hyeonseok Kim, Dr. Chee Siang Ang, Dr. Amir A Toor, Shinjae Kwon, Robert Herbert, Nathan Zavanelli, Nathan Rodeheaver, Jihoon Kim, Sung Hoon Lee, Carl Demolder, Sehyun Park, Jongsu Kim, Panote Siriaraya, Deogratias Mzurikwao, Riccardo Goldoni, Bryan Starbuck, Noah Kim, Andrew Short, Salman Salman, Badar Abdul Razzaq, Muhammad Mahmood, Jonathan Bardwell, Matthew Piper, Mark Reyes and Nicolas Agee.

I'd also like to thank the many people who generously contributed their time in order to participate as a research subject. Your time and patience are greatly appreciated.

I would like to thank my family for all their love and support; particularly my parents, who's advice and wisdom is infinitely valuable.

Finally, I would like to express my gratitude to my committee members, Dr. Frank Hammond, Dr. Todd Sulchek, Dr. Minoru Shinohara, and Dr. Audrey Duarte, for their valuable feedback during this process.

TABLE OF CONTENTS

ACKNOWLEDGEMENTS	iii
LIST OF TABLES	vi
LIST OF FIGURES	vii
LIST OF SYMBOLS AND ABBREVIATIONS	xv
SUMMARY	xvii
Chapter 1. Introduction	1
1.1 Overview	1
1.2 Problem Statement and Objectives	4
1.3 Thesis Organization	9
Chapter 2. Literature Review	11
2.1 Locked-In Syndrome	11
2.2 Brain-Machine Interfaces (BMI)	11
2.2.1 Invasive vs. Non-invasive Signal Acquisition	12
2.3 Electroencephalography-based BMI	12
2.3.1 Paradigms: Exogenous Stimulation	13
2.3.2 Paradigms: Endogenous Stimulation	14
2.4 Flexible Electronics	15
2.4.1 Fabrication Methods	15
Chapter 3. Brain-Machine interface based on Motor imagination	19
3.1 Background and Overview	19
3.2 Skintronics Concept and Design Principles	21
3.3 Methods for MI-based BMI	24
3.3.1 Electrode reduction via input perturbation analysis	24
3.3.2 Flexible microneedle electrodes	28
3.3.3 Flexible and stretchable interconnects	37
3.3.4 Flexible Skintronics data acquisition device	42
3.3.5 Experimental setup	45
3.4 Preprocessing and classification of MI brain activity with CNNs	46
3.4.1 Feature extraction and classification	49
3.4.2 Cross-validation of classification algorithms	50
3.5 Results of MI-based BMI	50
3.5.1 Demonstration of real-time control of VR video game	54
3.6 Conclusion	57
Chapter 4. SSVEP-Based BMI for Wheelchair control	60
4.1 Background and overview	60

4.2	Development of 5-target SSVEP-based motor wheelchair interface	61
4.2.1	Quantitative study of device mechanics and reliability	70
4.2.2	Analysis of device performance	78
4.2.3	Grid-search optimization of CNN	89
4.3	Results of 5-target SSVEP-based navigation interface	94
4.4	Discussion and Analysis	96
4.5	Conclusion	98
Chapter 5. SSVEP-Based VR Text Speller for Communication		99
5.1	Virtual Reality Environment	99
5.1.1	Stage 1: 11-target stimulus environment	100
5.1.2	Stage 2: 9-target dual-stimulus concept	101
5.1.3	Stage 3: Final 33-target Text Speller	103
5.2	Tangle-resistant high-throughput interconnects	103
5.2.1	Performance analysis	105
5.3	Biocompatible, flexible epoxy microneedle	105
5.3.1	Performance analysis	106
5.4	Results	107
5.5	Conclusion	113
Chapter 6. Future Work		115
6.1	Summary and original contribution	115
6.1.1	Novelties – Overall	115
6.1.2	Novelties – Chapter 3	116
6.1.3	Novelties – Chapter 4	116
6.1.4	Novelties – Chapter 5	117
6.1.5	Future Direction	117
Appendix		121
A.1	Calculation of Information Transfer Rate	121
A.2	Topographic Scalp Mapping using Deep Learning	122
A.3	Device Fabrication Process	124
A.4	Fabrication of Skin Electrodes via Aerosol Jet Printing	126
A.5	Frequency component analysis with CCA	128
References		129

LIST OF TABLES

Table 1	Comparison of impedance and impedance density of microneedle electrodes of varying height, with fixed base width of 200 μ m, and pitch of 500 μ m (14x14 array).	28
Table 2	PSDA and Cubic SVM Classification Results, Ag/AgCl with Conductive Paste Electrodes, 4-second time windows.	48
Table 3	Performance comparison between the <i>Skintronics</i> and reported values for EEG-based MI classification.	59
Table 4	2-CNN-Mapping: Convolutional Neural Network Model for Weight Extraction from 32-channel SSVEP Datasets. Using time domain data, we are able to optimize classification of real-time EEG data. Although the average accuracy was low across six subjects, we can generate mappings consistent with published literature regarding SSVEP.	65
Table 5	List of EEGs and Cable Length for Each System.	82
Table 6	Subject Information: Ethnicity and Hair Conditions. This table demonstrates the variety of hair conditions among the subjects and shows the consistent SNR achieved using the SKINTRONICS system.	96
Table 7	Comparison of information transfer rate (ITR) between the SKINTRONICS and reported values.	97
Table 8	List of Targets and Stimuli for Stage 1 VR Training Setup	101
Table 9	Demonstration of cross-fold validation of 11-class Stage 1 dataset using Spatial CNN with 1-second windows.	101
Table 10	List of Targets and Stimuli for Stage 2 (per-eye) VR Training Setup	102
Table 11	Demonstration of cross-fold validation of 9-class Stage 2 dataset using Spatial CNN with 1-second windows.	102
Table 12	Comparison of electrode characteristics used in testing.	107
Table 13	Comparison of information transfer rate (ITR) between the new VR-based SKINTRONICS and reported values.	112
Table 14	Overall results from 33-class VR-text speller directed training task.	112
Table 15	Select Companies Developing BMIs and related technologies. Bold text indicates an implanted device. Adapted from Smalley[96].	119

LIST OF FIGURES

Figure 1	Photo of subject with locked in syndrome wearing hair cap with electrodes.	2
Figure 2	AEIOU alphabet board. The assistant calls out the colors and the patient signals the required color by an eye movement. The assistant then sequentially calls out the letters on that line. The chosen letters are written down to formulate a sentence, question, or statement (adapted under fair use[17])	5
Figure 3	Overview of conventional EEG setups. (A) Demonstration of applying gel to one of many electrode locations on a conventional haircap EEG. (B) Conventional bench-top EEG with long electrode lead wires and haircap setup. (C) Wireless, wearable headset-based EEG with minimal wiring and dry electrodes.	7
Figure 4	Overview of the wireless scalp system for motor imagery brain signal detection, featuring fully portable electronics, stretchable interconnectors, and flexible microneedle arrays. A) An illustration of a subject wearing scalp electronics and a VR headset with a close-up of stretchable interconnectors (top-right photo) and a flexible microneedle electrode (bottom-right photo). B) A zoomed-in photo of an array of microneedles along with a magnified SEM image of the needles (inset). C) A picture of a flexible wireless circuit with integrated chips, showing mechanical compliance of the membrane circuit. D) Locations (top view) of the microneedle electrodes for classification of motor imagery brain signals, including six recording channels, one reference (REF) and one ground (GND). E) A flow chart describing the entire data processing sequence from EEG recording to the control of targets in a virtual reality system via a machine learning classification algorithm (convolutional neural network, CNN).	20
Figure 5	An illustrative overview of the <i>Skintronics</i> -based BMI. Subjects are trained on various BMI paradigms in an immersive virtual reality environment and wear a minimalist headgear with flexible hybrid electronics for the data acquisition, with flexible microneedle electrodes, and stretchable interconnectors.	23
Figure 6	Optimized channel selection process. (A) A complete 44-channel MI dataset is (B) trained on a spatial-CNN model. (C) A generator is used to cycle through the channel, setting the remaining channels as inactive, and (D) passed through the trained classifier. (E) The output perturbations are then compared with the true outputs, resulting in the relative perturbation, (F) which is summed over the classes to get the per-class perturbations for each channel. (G) A bar chart of each channel's relative perturbations is shown with the top-6 channels labeled.	26
Figure 7	Demonstration of channel reduction based on input perturbation analysis. Using a known dataset of 44 channels (left), we perform input perturbation analysis and rank the top-6 and top-4 channels (right), demonstrating the results of $81.70 \pm 3.17\%$ from the top-6, and $78.70 \pm 2.87\%$ from the top-4; a relatively small performance penalty based on the original $84.88 \pm 2.30\%$ from	27

44 channels.

Figure 8	Locations of electrodes, including Fz, C5, C3, C4, C6, and POz, with the reference electrode at Cz, and the ground electrode placed at the mastoid.	27
Figure 9	Fabrication process of an array of flexible microneedle electrodes	29
Figure 10	(A) Photos of electrode fabrication processes and (B) a collage of optical images of the finalized electrodes from various angles. The impedance and impedance density of microneedles are summarized in Table 1.	30
Figure 11	Flexibility evaluation of a microneedle electrode. (A) Photo of a test specimen structure for microneedle electrode cyclic bending test. (B) Schematic of a cross-section of the test specimen. (C) Picture of cyclic bending test setup in which the motorized testing rig continuously bends and un-bends the test specimen over a cylinder with a 5 mm bending radius. (D) Resistance data over 100 bending cycles (top), and a close-up of data over three cycles (bottom), showing the minimal fluctuation of resistance in the microneedle electrode.	33
Figure 12	A series of SEM close-up images microneedle electrode tip: unused (left, inset: zoom-in view of the tip), after ten insertions into porcine skin (middle), and after 100 insertions into the tissue (right).	34
Figure 13	Buckling force evaluation of a single microneedle electrode. (A) Buckling force testing setup in which the motorized force gauge applies an axial force upon a single microneedle electrode and measures the axial force until its fracture. (B) Photos of a single microneedle before (left) and after (right) the buckling test. (C) The buckling test data of five different single microneedle test specimens where buckling fracture begins at the peak force value.	34
Figure 14	Cytotoxicity results. (A) Immunofluorescent Hoescht labeling of human keratinocyte cells after 5-day culture experiment in contact with Gold-coated FMNA electrode. (B) Control experiment data of immunofluorescent Hoescht labeling of human keratinocyte cells after 5-day culture. (C) Fluorescence measurements that quantify cytotoxicity with cell viability reagent for FMNA electrodes vs. control.	35
Figure 15	Microneedle electrode wearing results. (A) Photo of redness on skin after 48-hours continuous wear of gold flexible microneedle electrode (left) and fading redness after 1-hour post release (right). (B) Thermal image (FLIR) showing skin temperature after 1 hour of wearing microneedle electrode behind the ear. (C) Thermal image showing skin temperature after 48 hours of wearing microneedle electrode on the skin (wrist).	36
Figure 16	A) Skin–electrode contact impedance that compares the performance between FMNE and conventional Ag/AgCl cup electrodes (error: standard deviation with $n = 4$ subjects). B) Calculated impedance density from data (A), showing a dramatic increase of the impedance change from the conventional electrode. C) SNR comparison of EEG alpha rhythms measured by FMNE (top) and	37

conventional Ag/AgCl electrodes (bottom).

Figure 17	Overview of stretchable interconnector fabrication process.	39
Figure 18	Characterization of stretchable EEG interconnectors. A) Photos of stretching of a stretchable EEG interconnector up to 100%. B) Electrical measurement of resistance change of the interconnector with 60% strain for 100 cycles, showing negligible changes in resistance. The inset shows the resistance change over a single stretch cycle. C) Measurement of electrical resistance change of the interconnector, showing mechanical fracture after 250% of tensile stretching.	40
Figure 19	Experimental setup of a stretching test. (A) Motorized test stand (ESM303, Mark-10), multimeter, and laptop data acquisition setup for stretch testing of stretchable interconnects. (B) A two-inch segment of stretchable interconnects secured between two binder clips pre-strain (left), and at 60% strain (right). (C) Change in resistance over 100 stretching cycles with 60% strain.	41
Figure 20	Close-up photos of a flexible interconnector with an excessive strain. (A) An entire view of an interconnector at 275% strain. (B) Close-up of the failure point near the contact pad.	41
Figure 21	Fabrication process of a flexible wireless <i>Skintronics</i> circuit using conventional cleanroom fabrication techniques.	43
Figure 22	Mechanical characterization of a flexible circuit. (A) Computational mechanics modeling data of a circuit bent at the location with components and interconnects, demonstrating 180° bending with a radius of curvature of 1.5 mm. (B) Close-up area from (A). (C) Photos of a circuit undergoing bending by following the computational modeling. (D) Mechanical test stand setup for cyclic bending, with multimeter and laptop for measuring resistance. (E) Resistance data over 100 bending cycles (top), and a close-up of data over a single cycle (bottom), showing the minimal fluctuation of resistance.	44
Figure 23	Comparison of CNN architectures and performance. (A) CNN architecture featuring multiple spatial convolution operations (Spatial-CNN), indicated with a ‘*’ symbol. (B) Standard CNN architecture with normal convolution operations along with the time-domain signals (Standard-CNN). (C) Confusion matrix demonstrating Spatial-CNN classifier performance on the FMNE dataset ($n = 2240$ samples from 4 subjects, 560 samples per subject, window length $w = 4$ s). (D) Confusion matrix demonstrating Standard-CNN classifier performance on the FMNE dataset ($n = 2240$ samples from 4 subjects, 560 samples per subject, window length $w = 4$ s).	47
Figure 24	PSDA feature comparison of four EEG classes, demonstrating the presence of ERS/ERD in the form of power spectrum shifts for many of the samples shown ($n=112$ samples).	49
Figure 25	Comparison of classification results with PSDA and SVM with a cubic kernel function on conventional Ag/AgCl electrodes and FMNEs, showing a better	51

accuracy from the FMNE dataset (4-second windows).

- Figure 26 Preprocessing and classification of motor imagery brain signals with CNNs. 52
 A) Detailed illustration of a spatial CNN model with hidden layers of brain signals acquired from six EEG channels. This model demonstrates the capability of decomposing spatial features from multiple dipolar sources of the motor cortex. B) Comparison of spatial-CNN classification accuracy of four cases, including raw data, high-pass filtered data (HPF), band-pass filtered data (Bandpass), and power spectral density analysis (PSDA) across multiple window lengths (1, 2, and 4 s). Error bars show a standard error from four subjects. C) Comparison of spatial-CNN classification accuracy between the conventional Ag/AgCl gel electrodes and the newly developed FMNE across multiple window lengths (1, 2, and 4 s). Error bars show a standard error from four subjects. D) A confusion matrix representing results from the real-time accuracy test of motor image brain data, acquired by conventional Ag/AgCl electrodes, with an overall accuracy of 89.65% ($N = 2,240$ samples, window length = 4 seconds, and 4 human subjects). E) A confusion matrix representing results from the real-time accuracy test of motor image brain data, acquired by FMNE, with an overall accuracy of 93.22% ($N = 2,240$ samples, window length = 4 seconds, and 4 human subjects).
- Figure 27 Comparison of the performance between Ag/AgCl electrodes and FMNEs 53
 across multiple window lengths (1, 2, and 4 seconds).
- Figure 28 Android interface demonstrating real-time data plotting. 55
- Figure 29 Virtual reality (VR) implementation for motor imagery training and real-time 56
 control of a video game demonstration. A) An overview of a study setup, including a subject wearing the *Skintronics*, real-time EEG data measured from six electrodes (top inset), an example of a VR interface (middle inset), and a photo of a subject wearing a VR headset (bottom-right inset). (B-D) Examples of the training and testing processes of a VR game. B) A modified view of VR visuals provided to test a subject with text and animation prompts. C) A video game interface designed for MI response testing with clear color-coded visual cues as well as a text prompt. D) An example of evaluation output according to the target class. E) An accuracy comparison between non-VR setup and VR setup (two types of electrodes) classified with Spatial-CNN model, demonstrating superior performance of VR as a training implement ($n = 2240$ samples from 4 subjects, 560 samples per subject, window length $w = 4$ s).
- Figure 30 Overview of the system architecture featuring fully portable, wireless scalp 63
 electronics. (A) Photo of a subject who has flexible wireless electronics (SKINTRONICS) conformed to the back of the neck with dry hair electrodes under a fabric headband and a membrane electrode on the mastoid, connected via thin film cables. (B) Neural network-based topographical map that indicates EEG signal amplitudes. (C) Photo capturing the ultrathin, flexible wireless electronics on skin, with an inset demonstrating device flexibility while handling. (D) Aerosol-jet printed stretchable, skin-like electrode with an open-mesh structure (inset). (E) Images showing gentle splaying of the conductive flexible elastomer legs of a dry hair electrode when slight

downward pressure is applied, allowing the legs to separate the hair and the Ag/AgCl tipped legs to achieve good contact with the scalp. (F) Illustration (left) showing electrode positions on a posterior view of the brain and highlighted occipital lobe and flow chart (right) describing the entire process of EEG-enabled brain-machine interfaces.

- Figure 31 Topographical mapping of EEG signals using convolutional neural networks. (a) 32-channel cap EEG setup on test subject. (b) Weights extracted from the 2-CNN-Mapping convolutional neural network. From 32 convolutional filters used across all channels, the average weights for each point are summed, resulting in the weight mappings for each of the six subjects as illustrated in (c). The color scale represents the rescaled average neural network weights based on $n=200$ samples (40 samples per class). (d) shows the mappings generated for all 6 subjects, labeled correspondingly. 66
- Figure 32 Antenna Matching Circuitry for SKINTRONICS wireless EEG. (A) shows the components in the antenna matching configuration optimized for use with the thin multilayer flexible SKINTRONICS format. (B) Shows reflection coefficient (S_{11}) measurement with a network analyzer in air, with the device placed flat on a glass slide. 67
- Figure 33 A schematic representation of the microfabrication and the assembly processes. Conventional microfabrication processes are used to construct the flexible circuit board. The PDMS-coated wafer surface allows the completed circuit boards to be peeled off and transferred onto a glass slide, where the reflow soldering of the chip components is carried out. The soldered board is detached from the glass slide and fully encapsulated with elastomer. 69
- Figure 34 Mechanical flexibility and stretchability of the scalp electronics. (A) Photo of the electronics bent at first location along the vertical axis, as shown in the inset photo, between microcontroller and ADC integrated circuits, demonstrating 180° bending (radius of curvature: 1.3 mm). (B) FEA of fine mesh structure simulating 180° bending in (A) with same radius resulting in minimal strain at the interconnects (scale bar: maximum principal strain). (C) Measurement of electrical resistance for the device in (A) under cyclic bending between 0 and 180° , showing negligible changes in resistance. (D) RSSI response at 0° and 180° with different distances up to 15 meters ($n = 3$ samples). (E) Device bent at the second location along the vertical axis, as shown in the inset photo, between ADC and amplifiers (radius of curvature: 1.3 mm). (F) FEA of the flexible structure simulating 180° bending with minimal strain (scale bar: maximum principal strain). (G) Measurement of cyclic bending effect on the device in (E) by recording the change of electrical resistance. (H) RSSI response up to 15 meters at 0° and 180° bending. (I) 15.2 Hz SSVEP data recorded without (top) and with 180° bending (bottom). (J) Hair-based elastomer electrode under compression. (K) Corresponding load and unload curves showing a negligible peak change in resistance over a 6-second cycle. (L) Subunit of a skin-mounted electrode under 100% stretching in experiment and FEA, showing no mechanical failure. (M) 180° bending test of the electrode, showing less than 2% strain in FEA and no mechanical defects in experimental observation. 72

Figure 35	Mechanical Testing Setup and Additional Results. (A) Picture of device conformed to skin, with lines indicating the two locations of bending. (B) 180° bending test setup, with the device attached to glass slides, and attached wires for resistance measurements. (C) Resistance measurements on cyclic bending after 100 cycles completed at two bending locations, indicated by the legend.	74
Figure 36	Compression Test Setup for Elastomeric Hair-based Electrodes. (A) Motorized tension/compression test stand setup with benchtop digital multimeter and laptop to measure resistance. (B) Placement of elastomeric hair-based electrodes between compression plates of test device.	75
Figure 37	Data from Compression Test of Elastomeric Hair-based Electrodes. (a) Resistance data measured across single leg of the elastomeric hair-based electrodes, with (b) showing a representative resistance curve for a single compression cycle. (c) is a smoothed curve computed from a moving average of (a), using a 6-second (90 sample) moving average, showing the drift in resistance over extensive mechanical usage.	76
Figure 38	Biaxial Stretching Test Setup for Skin Electrodes. (a) Custom device for biaxial stretching with a flexible skin-based electrode on an elastomer placed between the 4 clamps. (b) shows a close-up of the device with attached copper wire (using silver paste) for resistance measurement	77
Figure 39	Data from Biaxial Stretching and Bending of Skin Electrodes. (a) electrode near 60% biaxial stretching before fracturing, as shown in (b). (c) experimental stretching shows deformation of the silver causing an increase in resistance. (d) Bending 180° increases the resistance due to the deformation of the skin-electrode but releasing that stress brings the resistance back down.	78
Figure 40	Analysis of the device performance in signal quality, feature extraction and classification accuracy. Three data sets for a conventional hair cap system (ActiveTwo; <i>1st column</i>), bulky clip-on wireless system (BioRadio; <i>2nd column</i>), and our 2-channel SKINTRONICS (<i>3rd column</i>). (A-C) Periodograms of 50 samples from 12.5 Hz SSVEP signals overlaid over each other, with peaks highlighted with red circles; this comparison illustrates our device's ability to target and capture SSVEP signals without excessive noise precisely and consistently. (D-F). Average signal-to-noise ratio (SNR) with four SSVEP classes, across all six tested subjects. Error bars represent standard error of the mean (n=60 recordings; 6 subjects, 10 recordings each). (G) Two-channel SSVEP data at 12.5 Hz in time domain by using 4 Hz Butterworth high-pass filter and removed baseline drift. (H) Further preprocessing in the form of frequency-analysis including a single-window periodogram. (I) Welch power-spectral density analysis (PSDA) overlapping periodogram. (J) Cross-spectral density analysis (CSDA) of both channels. Note that the cross-spectral input includes the normal Welch power spectrum, resulting in three feature sets to the 1-layer CNN. (K) Comparison of classification accuracy between four preprocessing methods, shown in (G-J). The points on the graph are the mean accuracies from 36 trials from all 6 test subjects. Error bars represent standard error of the mean (n = 36 trials).	80

- Figure 41 Feature representations using power and cross-spectral analyses. (A) A filtered EEG sample encoded with a noisy 15.2 Hz SSVEP signal in channels O1 and O2. (B) A simple periodogram using a window of equivalent length (single window periodogram). (C) The cross-spectral estimate of the single-windowed periodograms. This result may be improved by using windows of 0.5-second length with 50% overlap (Welch's method), as seen in (D). Now, the 15.2 Hz peak is better represented, but still contains a peak around 11Hz. Taking the cross spectral estimate with Welch's method gives us (E), which most closely represents the intended frequency content. In this example, the baseline CNN trained for classifying cross-spectral density data predicts the correct class. The labels show the predicted class and softmax output probabilities, where red represents a false classification output, and green represents the correct output. 84
- Figure 42 Hyperparameter Optimization of 1 Layer Convolutional Neural Network. (A) Different learning rates between $1e-2$ and $1e-4$ were tested in, followed by number of units in the fully connected layer in (B). (C) Dropout regularization in between 25% and 75% is then added and analyzed. (D) Different activations in the fully connected layer are added. It appears that ReLU activation performs more optimally in the fully connected layer. (E) The activations following the convolution operation were varied, with LeakyReLU performing most optimally. (F) The number of filters was varied from 1 to 32, with 5 filters providing the most optimal performance with $92.53 \pm 1.01\%$. 88
- Figure 43 EEG classification with CNN. (A) High-pass filtered raw EEG data in time domain with features linearly rescaled between 0 and 1, labeled as SSVEP class '12.5 Hz', along with a representative greyscale image. (B) Greyscale representation of output weights in the two layers of CNN as well as in the fully connected layer using the 2-CNN model for time domain data. (C) Table of softmax class outputs, indicating a correct choice with 99.89% probability. (D) CNN and SVM classification test accuracy using time domain data and cross-validating across all subjects. (E) CNN and SVM test accuracy on frequency-domain data, cross-validating across all subjects, with window lengths from 0.512 to 2.048 seconds. The displayed results are from the strongest SVM of the four tested (cubic kernel). (F) Confusion matrix representing results from offline accuracy test of time-domain data of data window length $w=0.512s$, with an overall accuracy of 94.54% ($n=2700$ samples; 6 subjects, 450 samples each). (G) Confusion matrix representing results from real-time accuracy test of time-domain data of length $w=0.512s$, with an overall accuracy of 94.01% ($n=2700$ samples; 6 subjects, 450 samples each). 91
- Figure 44 *In vivo* demonstration of wireless, portable BMI with human subjects. (A) Subject seated in a powered wheelchair with the LED stimulus array (B) and SKINTRONICS secured and conforming to the back of the neck (C). (D) Android user interface during training and evaluation, showing time-domain data, corresponding power spectrum, and output class. (E) EEG data recorded at each state, labeled as alpha rhythms, 11.1 Hz, 15.2 Hz, 12.5 Hz, 16.7 Hz SSVEP respectively. (F-H) Three target machines to control via SSVEP signals, including a wireless electronic wheelchair (F) with 5 classes (no action, forward, rotate counterclockwise, rotate clockwise, and reverse, and 93

wireless vehicle (G) with the same commands as the wheelchair, and PowerPoint presentation (H) with 5-class actions (no action, begin presentation, next slide, previous slide, and end presentation, respectively). To compare SKINTRONICS to commercial systems, the same optimized CNN procedure was performed on data from the BioRadio and ActiveTwo systems.

A plot comparing the data from all three systems is shown in Figure 45, showing a clear gulf between the accuracies of the SKINTRONICS and the other two systems. This data is supported by the difference in SNR, as discussed previously.

Figure 45	Comparison of classification accuracies of time domain data from SKINTRONICS, BioRadio and ActiveTwo systems using optimized CNN model.	94
Figure 46	Flowchart demonstrating information flow for training environment	100
Figure 47	Default text speller interface layout. (A) Frequency of each stimulus tile in Hz and (B) corresponding command on default English keyboard.	103
Figure 48	Characterization of stretchable EEG interconnectors. A) Photos showing test setup with benchtop DMM connected to sample. The sample is connected using ACF cables using silver paint. B) Measurement of electrical resistance change showing mechanical fracture after ~65% of tensile stretching. C) Cyclic tensile stretching of up to 20% strain for 100 cycles, with minimal resistance changes. D) Peak resistance change per cycle over 100 cycles.	
Figure 49	Overview of refined <i>Skintronics</i> system. (A) Subject wearing <i>Skintronics</i> EEG interface and VR headset. (B) Cropped screenshot of VR text speller interface (C) closeup of new epoxy microneedle electrode (uncoated). (D) closeup of tangle-resistant interconnector peeling from substrate. (E) closeup photo showing <i>Skintronics</i> EEG flexibility. (F) demonstration stretching from relaxed state (left) to 40% strain on interconnector (right).	109
Figure 50	Relative electrode positions of 4-channel bilateral SSVEP setup.	110
Figure 51	Spatial-CNN architecture and revealed hidden layers, as well as output demonstrating accurate classification from a 33-class dataset.	111
Figure 52	User interface demonstrating a potential use for an SSVEP-based BMI, allowing a user to browse the web through their VR headset; in this example, watching a video online.	114
Figure 53	Proposed advanced manufacturing techniques for future <i>Skintronics-type</i> and flexible hybrid electronics.	118

LIST OF SYMBOLS AND ABBREVIATIONS

ACF	Anisotropic Conductive Film
AEIOU	Acronym for alphabet board method for communication. Letters represent vowels in English language from the first column.
AJP	Aerosol-Jet Printing
BMI	Brain-Machine Interface
CCA	Canonical correlation analysis
CNN	Convolutional neural network
CSDA	Cross-spectral density analysis
DMM	Digital multimeter
ECoG	Electrocorticography
EEG	Electroencephalography
ERD	Event-related desynchronization
ERP	Event-related potential
ERS	Event-related synchronization
FEA	Finite element analysis
FMNE	Flexible microneedle electrode
GND	Ground
HPF	High-pass filter
IJP	Inkjet printing
IPA	Isopropyl alcohol
IRB	Institutional review board
LED	Light emitting diode
LIS	Locked-in Syndrome
MI	Motor imagination or motor imagery
MN	Microneedle
NMP	<i>N</i> -Methyl-2-pyrrolidone
P300	P300 wave, an event-related potential
PA	Pneumatic Atomizer
PDMS	Polydimethylsiloxane
PI	Polyimide

PSDA	Power spectral density analysis
REF	Reference
REM	Replica molding
RSSI	Received signal strength indication
RVS	Repetitive visual stimulus
<i>Skintronics</i>	Skin-like Electronics
SNR	Signal-to-noise ratio
SSVEP	Steady-state visually evoked potentials
SVM	Support vector machine
TRCA	task-related component analysis
UA	Ultrasonic atomizer
UV	Ultraviolet
VR	Virtual reality

SUMMARY

Advancing technology has increasingly allowed for individuals suffering from severe disabilities (e.g. locked-in syndrome) to allow for movement or communication. These technologies include low-power wireless protocols, wearable, battery powered devices, flexible electronics, biocompatible skin-interfaced materials and advanced machine learning techniques. Current non-invasive brain-machine interfaces are limited in scope, have limited functionality, and primarily only used in research environments. The more recent move towards wearable, wireless system has enabled greater mobility. However, issues remain – these systems are bulky, uncomfortable to wear, and often involve the use of messy conductive pastes and gels.

In this dissertation, we introduce a flexible electronics platform, *SKINTRONICS*, with a comprehensive redesign of an EEG-based brain-machine interface with novel implementation of flexible EEG, flexible and stretchable interconnects, replica-molded microneedle electrodes, and advanced machine learning techniques for improved signal to noise ratio and reduced noise and motion artefacts. A set of general improvements and novel advancements are examined and applied in real-world electroencephalography-based brain-machine interfaces. These real-world improvements and applications show potential for restoring function to and improving quality of life of severely disabled subjects. Wireless, wearable electroencephalograms and dry non-invasive electrodes can be utilized to allow recording of brain activity on a mobile subject to allow for unrestricted movement. Additionally, multilayer microfabricated flexible circuits, combined with a soft materials platform, provide imperceptible wearable electronics for

wireless, portable, long-term recording of brain signals. This dissertation focuses on sharing the study outcomes in soft materials, flexible electronics, and machine learning for universal brain-machine interfaces that could offer remedies in communication and movement for these individuals.

INTRODUCTION

1.1 Overview

Locked-in syndrome (LIS) is one of the greatest misfortunes a person can suffer. LIS describes a state of complete paralysis apart from blinking and eye movement[1]. Here, brain activity and cognitive function are usually unaffected, resulting in a state of pseudo-coma where a subject can neither move nor communicate, but are perfectly aware of their consciousness and environment (Figure 1A). Despite apparently normal cortical brain activity, the brain is cut off from accessing motor function, typically due to injury to the lower brain and brainstem. There are several causes of LIS in humans, including but not limited to: stroke of the brainstem, traumatic brain injury or hemorrhage, poisoning, and drug overdose. Diagnosis of LIS is enabled using brain activity analysis with instruments such as EEG to observe the sleep-wake patterns of the affected individuals.



Figure 1. Photo of subject with locked in syndrome wearing hair cap with electrodes.

LIS cases are relatively rare, with occurrences of less than 1 in 100,000 in the Netherlands [2]. Based on this estimate, a rough estimate of the total number of occurrences in the world is likely no more than 80,000 individuals. However, due to the severity of the condition and lack of available therapeutics, it is considered a valuable endeavor to pursue technological advancement to allow these individuals to move or communicate. The research generated towards this end has provided, and will continue to provide, valuable information about the nature of brain and its activity. Furthermore, breakthroughs in this field will allow for dramatic improvements in quality-of-life for these afflicted individuals. There is additionally great potential to spawn technological advancements which may be utilized by a much greater population, potentially allowing for improvements in communication throughput. These advances may further improve quality of life and productivity for future generations.

One of the most important developments is that of the brain-machine interface (BMI). A BMI utilizes measurements of brain activity in order to bypass motor function to control machines such as computers or prosthetic devices. BMIs offer a potential solution to subjects with severe physical disability such as LIS or quadriplegia, restoring some level of movement and communication to these individuals, improving quality of life.

Recent advances in technology have allowed for the use of lightweight flexible electronics and dry compliant electrodes for improved biopotential signal acquisition. EEG design has trended towards wearables with wireless functionality since the standardization of common wireless protocols such as Bluetooth [3]. In general, a combination of miniaturization and other improvements have led away from benchtop amplifiers and electrode cap EEGs, favoring compact, battery-powered designs. Dry electrodes offer excellent, consistent long term performance compared with gel-based electrodes[4-6]; provided the skin preparation, and amplifier, shielding and electrode configurations are adequate [5, 7]. Lightweight sensors with minimal cabling also greatly reduces dragging or movement artefacts that are common with poorly configured conventional EEG [8].

Further advancements include that of flexible electronics, soft materials, and advanced electronics fabrication techniques that provide additional functionality while also reducing production costs. Initially, flexible hybrid electronics were fabricated using conventional microfabrication techniques such as sputter material deposition and photolithography. New methods for additive manufacturing (such as aerosol jet printing), and alternate etching methods (e.g. femtosecond laser micromachining) greatly improve

process speed and potential throughput [9-11]. Additionally, use of materials such as polydimethylsiloxane (PDMS) allows for fast high-quality replica-molding of conventionally expensive cleanroom-based microfabricated structures for higher component production rates[12]. Advancements in computing power have allowed for processing of real-time environments for wearable and wireless virtual reality headsets. The use of virtual reality allows researchers to tackle specific problems where the interface user's attention needs to be maximized, or where immersion is critical[10, 13, 14]. Computational advances, combined with advanced machine learning techniques, such as convolutional neural networks [15, 16], also allow for real-time classification of highly complex problems for real-time control of interfaces. In this thesis, we will explore how these advancements are integrated into a single, robust, multifaceted BMI system.

1.2 Problem Statement and Objectives

In order to communicate with LIS subjects, current communication schemes involve the use of AEIOU boards or similar non-technological approaches as shown in Figure 2, where a caretaker uses the limited eye movement of a subject to select letters, by calling out the rows, and then letters and looking for an affirmative eye motion. Such methods are slow and tedious, with a subject only being able to spell a few words per minute. This greatly limits the ability of subjects to communicate their intentions and can be vastly improved with brain-machine interfaces (BMI).

A	B	C	D	End of word	
E	F	G	H	End of sentence	
I	J	K	L	M	N
O	P	Q	R	S	T
U	V	W	X	Y	Z

Figure 2. AEIOU alphabet board. The assistant calls out the colors and the patient signals the required color by an eye movement. The assistant then sequentially calls out the letters on that line. The chosen letters are written down to formulate a sentence, question, or statement (adapted under fair use[17]).

Electroencephalography (EEG) is a common non-invasive method of acquiring brain electrical activity, which results in a few critical tradeoffs when compared with invasive interfacing methods (e.g. implanted electrodes; electrocorticography). Most importantly, signal quality is greatly diminished when compared to electrodes implanted directly into brain or nerve tissue. Additionally, there is a significant reduction in spatial resolution due to the physical distance as well as multiple barriers (brain fluids, skull, skin, etc.), between the signal source and electrodes. With EEG, electrical activity records the summation of excitatory and inhibitory postsynaptic potentials in apical dendrites of pyramidal neurons in the more superficial layers of the cortex. Large areas of the cortex must be activated synchronously to generate enough of a potential change to be measured at the scalp. This problem is intuitively understood through the inverse square law[18]. Based on these limitations, neurons deep in the cortex are unable to significantly influence scalp EEG signals, limiting the range of EEG-based BMI paradigms[19].

Currently available mobile EEG systems[20-22] are still limited by their bulky size and use rigid electronics and housings with a great number of electrodes. Conventional EEG used in research and medical application typically involve bulky headgear and interface with the scalp through cluster of metal electrodes (Figure 3). These systems are often bulky, heavy and uncomfortable to wear. They often require large, rigid electronics either attached to the system, or connected to benchtop electronics using long lead wires. Often, electrodes are interfaced with the scalp using conductive gels or pastes to adequately capture the signal. These gels and pastes are messy and experience signal degradation over time, preventing long-term use. Further, hair thickness and density and skin quality cause significant impedance variation between subjects and even between electrode locations the same subject. Overall, conventional systems require extensive time for setup and are inconvenient and uncomfortable to use.

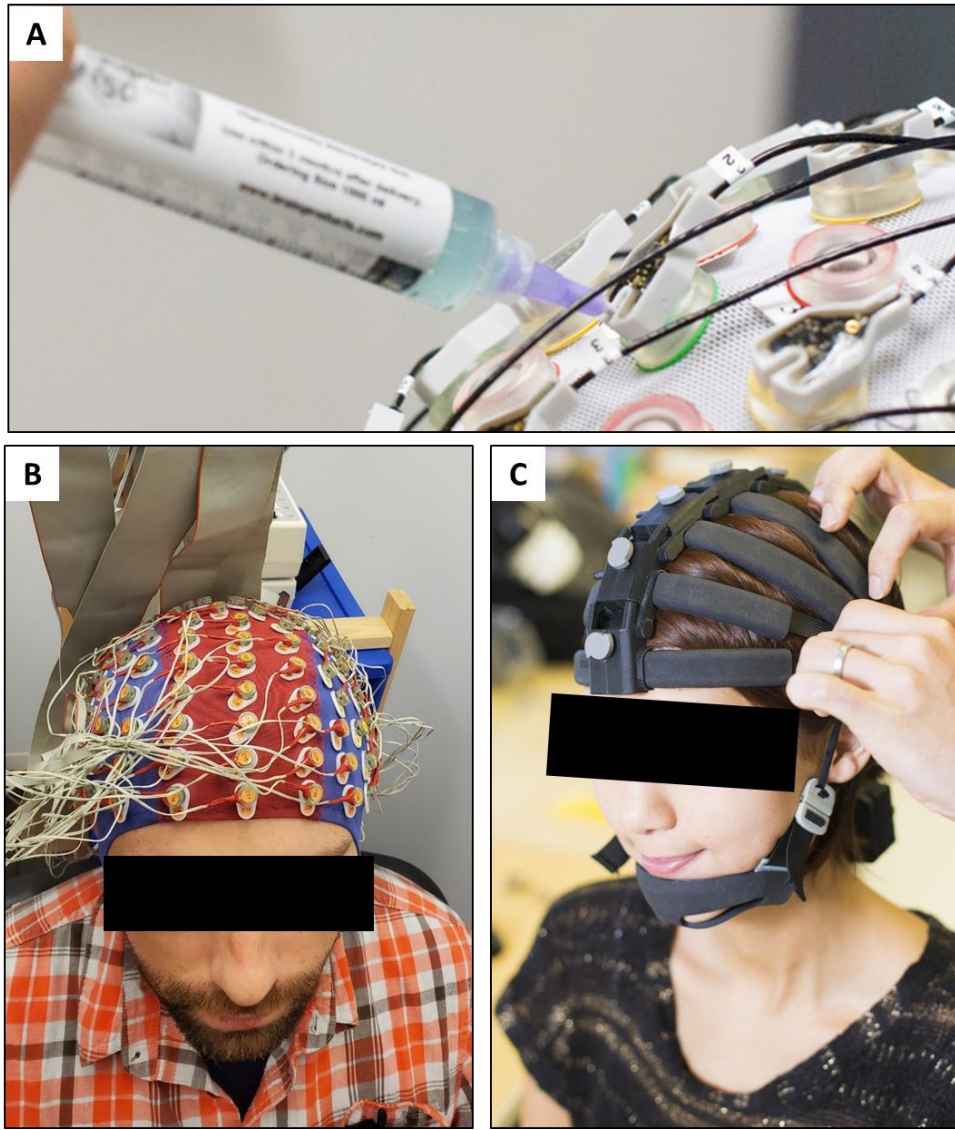


Figure 3. Overview of conventional EEG setups. (A) Demonstration of applying gel to one of many electrode locations on a conventional haircap EEG. (B) Conventional bench-top EEG with long electrode lead wires and haircap setup. (C) Wireless, wearable headset-based EEG with minimal wiring and dry electrodes.

In order to be considered a viable alternative to non-technical solutions (e.g. AEIOU board), the interface must allow for significantly advanced information transfer rates and must also not be a burden on the subject or caretakers (which are not always professionals, e.g. family members). The AEIOU board uses 28 targets. From this we can estimate a range for potential information transfer rates based on the communicators'

abilities and a range of cognitive states available, we can estimate a range of average target selection times of between 5 and 15 seconds per target. Assuming perfect accuracy, we can use the formula in the Appendix chapter *Calculation of Information Transfer Rate* to calculate the potential information throughput to be between 19-60 bits/min, with 60 being exceptionally fast performance, and the average being around 24 bits/min. As a result, this system sets the bar for brain-machine interface performance. At a minimum, BMIs can offer the ability to replace such systems, allowing for more free-flowing communication at similar bit rates. However, BMIs have demonstrated the potential for much higher information throughputs with the ability to allow for up to 40 targets at intervals of 0.8s, for transfer rates up to 325 bits/min[23].

As stated in the problem statement, the objective of the research was to enhance the performance of brain-machine interfaces by studying the performance benefits of flexible electronics, soft skin-compliant materials, advanced machine learning techniques. Based on the literature review, analysis of the capabilities of the available technology, certain requirements and specifications were created in order to maximize the performance of an EEG-based interface. First, gel or paste based electrodes were excluded in favor of dry electrodes, due to vastly improved long-term impedance consistency, and potentially improved impedance density. Dry electrodes also provide the added benefit of requiring less time to setup and clean and is therefore more convenient to an EEG operator. Dry electrodes allow for a “set-and-forget” type EEG system that requires minimum maintenance once setup and can be used for extended periods of times, with some dry electrode systems allowing for weeks of continuous wear[24]. Second, flexible electronics were preferred for all components including electrodes and electrode

leads. Flexible electrodes allow for conformal skin-contact, typically resulting in improved signal to noise ratio, reduced motion artefacts and improved performance[25]. Additionally, it was hypothesized that device miniaturization could improve performance due to fewer sources of noise across the entire device and reducing the distance between the data acquisition and signal source is crucial to high-quality data recordings[26].

Further, advanced machine learning techniques, such as deep convolutional neural networks, would be evaluated for their potential to improve feature extraction and classification of subtle components within time-domain EEG signals. Additionally, the implementation of virtual reality as a means of immersive subject training and its potential use as a unique stimulus platform is explored in this thesis. Overall, the goal of this thesis is to use to create new technologies for a non-invasive BMI system for at-home use allowing for control of devices such as computers or electric wheelchairs on a day-to-day basis. Such a system has the potential to greatly improve the quality of life of individuals with LIS, by providing them with much needed ability to move and connect with others.

1.3 Thesis Organization

This thesis is organized into a literature review chapter, and chapters corresponding to each major experiment performed as a part of this thesis. The next chapter, Chapter 2, will cover the literature review, covering topics such as the target demographic for this research (Locked-in Syndrome), and exploration of each of the individual technologies used in this thesis (Brain-machine interfaces, electroencephalography (EEG), EEG electrodes, and soft, flexible electronics). Chapter 3

describes an attempt to design a BMI based on motor imagination (MI) using flexible hybrid electronics and a VR immersive training environment. Chapter 4 demonstrates a 5-class SSVEP-based BMI for the purposes of accurate control of an electric wheelchair. Chapter 5 expands greatly upon the research from Chapter 4, using 33 targets in order to control a VR-based text speller for communication. Finally, the thesis is ended with a summary detailing the novelties introduced and proposal of future work that may expand upon this research. After the references section, an Appendix chapter contains text, tables and figures that were extraneous to the dissertation's main text.

LITERATURE REVIEW

2.1 Locked-In Syndrome

Locked-in syndrome is a serious syndrome of an underlying disease, typically injury to the ventral pons, and typically an infarction, hemorrhage or trauma of some kind[17]. LIS is characterized by quadriplegia and anarthria (inability to speak or vocalize)[17]. The subject's consciousness is otherwise normal, and they can slowly communicate via blinks or eye movements. Without technological assistance, communication with these patients is very slow, typically making use of an AEIOU board, where the subject indicates the row and column of the letter or symbol they would like to communicate as the communicator reads them out (see Chapter 1 for more details). Overall, quality of life for LIS subjects is poor, and there is no standard treatment or cure for the condition. Out of 105 cases examined by Das et al., only 29 showed some form of recovery and two showed complete recovery, although this is anomalous and not well understood[27].

2.2 Brain-Machine Interfaces (BMI)

A brain machine interface (BMI) is a communication system using data acquired directly from brain activity which allows humans to interact with their surroundings without the involvement of peripheral nerves and muscles. BMI can be used to relay a person's intentions to external devices such as computers, speech synthesizers, assistive appliances, and neural prostheses, which is highly attractive for helping patients with severe disabilities, like LIS. There are two broad categories used to classify BMIs: invasive and non-invasive.

2.2.1 Invasive vs. Non-invasive Signal Acquisition

Invasive methods include electrode implants, such as a microelectrode arrays[28], or electrodes placed deep in the cortex[29]. However, invasive systems are costly to develop and highly risky to patients. In this thesis, non-invasive EEG-based BMIs will be the primary focus, as implanted devices are outside of the scope of this research.

2.3 Electroencephalography-based BMI

Most current BMIs obtain brain activity through electroencephalography (EEG). EEG is the most widely used neuroimaging modality, due to its high temporal resolution, portability, low cost, and low user risk. BMIs based on EEG consist of a set of sensors that acquire electroencephalography signals from different brain areas. However, the quality of electroencephalography signals is affected by scalp, skull, and many other layers as well as background noise. Reducing noise is critical to recording representative EEG signals which reflect localized brain activity. The primary challenge to designing high quality EEG is the reduction of noise introduction, and removal of common mode noise using driven right-leg circuitry, passive or active shielding and other design methods.

These noninvasive approaches have successfully been applied to severely and partially paralyzed patients allowing for basic communication and control[30]. Despite the outstanding utility of non-invasive approaches in BMI applications, full motor recovery has been limited, due to the limit resolution of brain information acquired from noninvasive EEG. Invasive recording methods such as electrocorticography or intracortical neuron recording improve the quality of brain signals monitored by BMIs.

Most researchers agree that movement restoration through prostheses with multiples degrees of freedom can only be achieved through invasive approaches[31]. Due to fundamental physical limitations based on the inverse square law, it is likely that non-invasive modalities can never be as powerful as invasive ones. Further refinement in recording, processing and analysis will likely improve performance of both invasive and non-invasive methods. The latest research shows that invasive modalities have inherent advantages in neuroprosthesis control applications[32].

2.3.1 Paradigms: Exogenous Stimulation

P300

P300 is an event-related potential (ERP) that may be utilized in BMIs as it provides an easy-to-discern amplitude fluctuation that lasts about 300ms, hence the name[33]. In a synchronized system, P300 can be used in a text-speller type interface by sequentially flashing letters. A P300 is elicited when a viewed letter flashes, the timing of which helps the classification algorithm indicate which target was selected[34]. P300 has been well explored in the field of BMI[33], and is outside the scope of this dissertation.

SSVEP

An SSVEP-based BMI enables the user to select one of numerous application-dependent commands, for example, moving a cursor on a computer screen. Each command is associated with a visual stimulus with distinctive properties such as frequency or phase. The stimuli are simultaneously presented to the user who selects a command by focusing attention on the corresponding stimulus. When the user focuses their attention on the

stimulus, an SSVEP is elicited which manifests as oscillatory components in the user's EEG, localized from the primary visual cortex, matching the frequency or harmonics of that stimulus frequency [35]. SSVEPs can be detected by preprocessing (e.g., band-pass filtering), removing artifacts, and extracting features (e.g., using power spectral analysis), and then classification. BMI performance is assessed in terms of classification accuracy, selection time, and the number of available targets. These can be aggregated into a single indicator, namely the information transfer rate [36, 37]. In SSVEP-based BMIs, the classification accuracy is mostly influenced by the signal-to-noise ratio (SNR), and the separability in the properties of the stimuli. The classification speed depends on the time it takes for the signal to be recognizable as belonging to a unique target and is highly limited by noise. Increasing the number of targets increased the number of possible commands at the cost of classification accuracy and speed.

2.3.2 Paradigms: Endogenous Stimulation

Motor Imagery

Motor imagery, also called motor imagination is a useful BMI paradigm as it does not require any external stimulus for a BMI user to control the interface. There is now sufficient evidence that MI, the mental rehearsal of physical movement tasks, when combined with physical therapy leads to enhanced motor outcomes for stroke survivors and may represent a new approach to functional recovery after stroke[38]. EEG-based BMI can provide real-time measure and classification of MI as a neurofeedback to aid motor task execution [39]. These sensorimotor rhythms are oscillations in the EEG in the alpha (8 to 12 Hz) and beta (18 to 26 Hz) bands. Modulations in these bands are observed

during motor action, mentally rehearsal, or imagined movements. Distinct phenomena such as event-related desynchronization (ERD) and synchronization (ERS) are clearly detectable on EEG during MI in healthy subjects[40]. Recent studies demonstrate that ERD and ERS can be enhanced by closing the sensorimotor loop using proprioceptive [41] or haptic feedback [42].

Motor imagery is somewhat controversial due to the wide variance in subject performance. Allison and Neuper discuss the limitations in dealing with motor imagery performance in detail [43]. Performance predictors for different control paradigms have been documented in the literature [44]. Within the same BMI system, especially with MI, some subjects cannot achieve satisfactory performance, which is referred to as BMI “illiteracy”. Therefore, it is necessary to understand why different subject groups perform achieve different BMI performance outcomes. Allison and Neuper[43] also reported that subjects with low performance show fewer prominent features than those who perform better, thus resulting in poor class recognition. Overall, the literature demonstrates that motor imagery can be functional to a reasonable segment of the general population, but for those with poor response, alternative paradigms should be sought.

2.4 Flexible Electronics

2.4.1 Fabrication Methods

In this section, various fabrication methods are discussed regarding the production of flexible electronics and flexible components. There are two main branches of fabrication processes: additive and subtractive. In the following sections, a few of these are analysed

with a focus on processes that are significant towards development of a brain-machine interface.

Conventional Cleanroom-based Methods

Microfabrication and photolithography methods involve a meticulous series of cleaning, metallization, oxidation, spin casting, light exposure, and etching and developing. These processing steps create possibilities for contamination. Successful fabrication results in the completion of a device capable of sensing, stimulating, or communicating signals.

Common procedure for soft electronic fabrication involves starting with a silicon wafer by cleaning and spin coating several layers of polymers, such as a sacrificial polymer. Afterwards, e-beam evaporation or sputtering deposition is used for metal deposition. A layer of positive or negative photoresist is spun atop this layer, then exposed with ultraviolet (UV) light through a chrome photomask. Next, the metal is etched using a wet etching process, resulting in metal ion waste while the patterns on the substrate remain. The photoresist is cleaned off and the process continues or is completed and ready for the transfer process.

Microfabrication and photolithography are robust fabrication methods which result in significant material waste. This can have far reaching environmental effects [45] and may well be financially detrimental[46]. This process is also time consuming due to the many adding and subtracting processing steps. Therefore, additive methods are preferable as an alternative by streamlining the process and reducing harmful environmental waste. These methods must be adequately assessed for its advantages and disadvantages in the fields of speed, resolution, and reliability.

Additive Manufacturing: Aerosol-Jet Printing

Aerosol jet printing (AJP) uses mass flow controllers to direct nitrogen gas into either ultrasonic or pneumatic atomizers. This inert gas enables transportation of aerosolized inks for deposition through a nozzle without affecting the inks' properties. An ultrasonic atomizer (UA) relies on excitation from a piezoelectric transducer, transferring the energy through a temperature-controlled water bath medium. This allows for reliable atomization of inks of varying viscosities; up to 5 cP. This range may be expanded using higher bath temperatures.

Alternatively, pneumatic atomizers (PA) can atomize inks up to 1000 cPs. This allows for far greater versatility than UA printing or inkjet printing. A PA pushes nitrogen down a stem out of a diffuser using high velocity flow, while the ink is sucked up through the diffuser hole. This process creates ink agglomerates of various size that are filtered through a virtual impactor and HEPA filter. The smaller agglomerates pass through the deposition head onto the substrate.

Most polymers consist of very low surface energy particles which requires precise tailoring of the surface tension of the ink that is deposited on a polymer. Other materials, like metals, have relatively high surface energy which allow for easier ink deposition. Therefore, inks must be tailored to wet the surface properly to prevent breaks or disconnections by utilizing either a low surface tension ink or a high energy substrate. High throughput deposition with AJP requires fine control over multiple variables. Many researchers working on microscale devices like antennas[47], strain sensors[48], and biological samples[49] do not require rapid deposition rates or platen velocities. In this

thesis, fabrication of thin, skin-based Ag electrodes is discussed. A materials characterization study of AJP inks after sintering is also investigated for its electrical conductivity and mechanical elastic modulus.

Replica Molding

Replica molding (REM) is a form of soft lithography utilizing materials like polydimethylsiloxane (PDMS) to create microscale devices by duplicating the structure of a mold[50]. REM is typically used to efficiently mold patterns with features up to a nano-scale (≤ 100 nm)[51] that often are difficult to replicate for other forms of molding, such as injection molding. The most commonly used organic polymer for REM is PDMS. A range of products ranging from CDs to biomedical devices are fabricated using REM.

The most significant advantage to REM is that you can create many replica devices from one master mold. This means that the process can be scaled up very quickly with very few master molds; which often are created using the slower and more expensive conventional lithography-based methods. As a result, REM greatly increases production and fabrication throughput. Another major advantage is that REM is compatible with a wide variety of polymers and compounds, making it highly versatile and flexible. REM can also create molds that cover a wide range of nonlinear surfaces and is also not limited by size constraints (e.g. wafer sizes). Therefore, REM is a very valuable structure replicating technique capable of a wide array of materials for a wide variety of uses[50, 52, 53].

BRAIN-MACHINE INTERFACE BASED ON MOTOR IMAGINATION

3.1 Background and Overview

In this chapter, we focus on the application of *Skintronics* to a Motor Imagery-based BMI. An overview of this *Skintronics* system is shown in Figure 4. The complete interface in Figure 4A-B includes a flexible wireless circuit, placed on top of the elastomeric band on the crown of the head for maximized isolation from the body. A fabricated soft circuit in Figure 4C demonstrates high mechanical flexibility when mounted on an index finger. A combination of metallization, laser-cutting process, and transfer-printing step allows fabricating reliable membrane interconnectors. A robust connection between the circuit and multiple FMNEs is enabled by stretchable interconnectors. A schematic illustration in Figure 4D shows the optimized locations of FMNEs based on the analysis of publicly available MI data and experimental results. A flowchart of the overall setup and data flow are shown in Figure 4E, towards control of a VR game via real-time MI data.

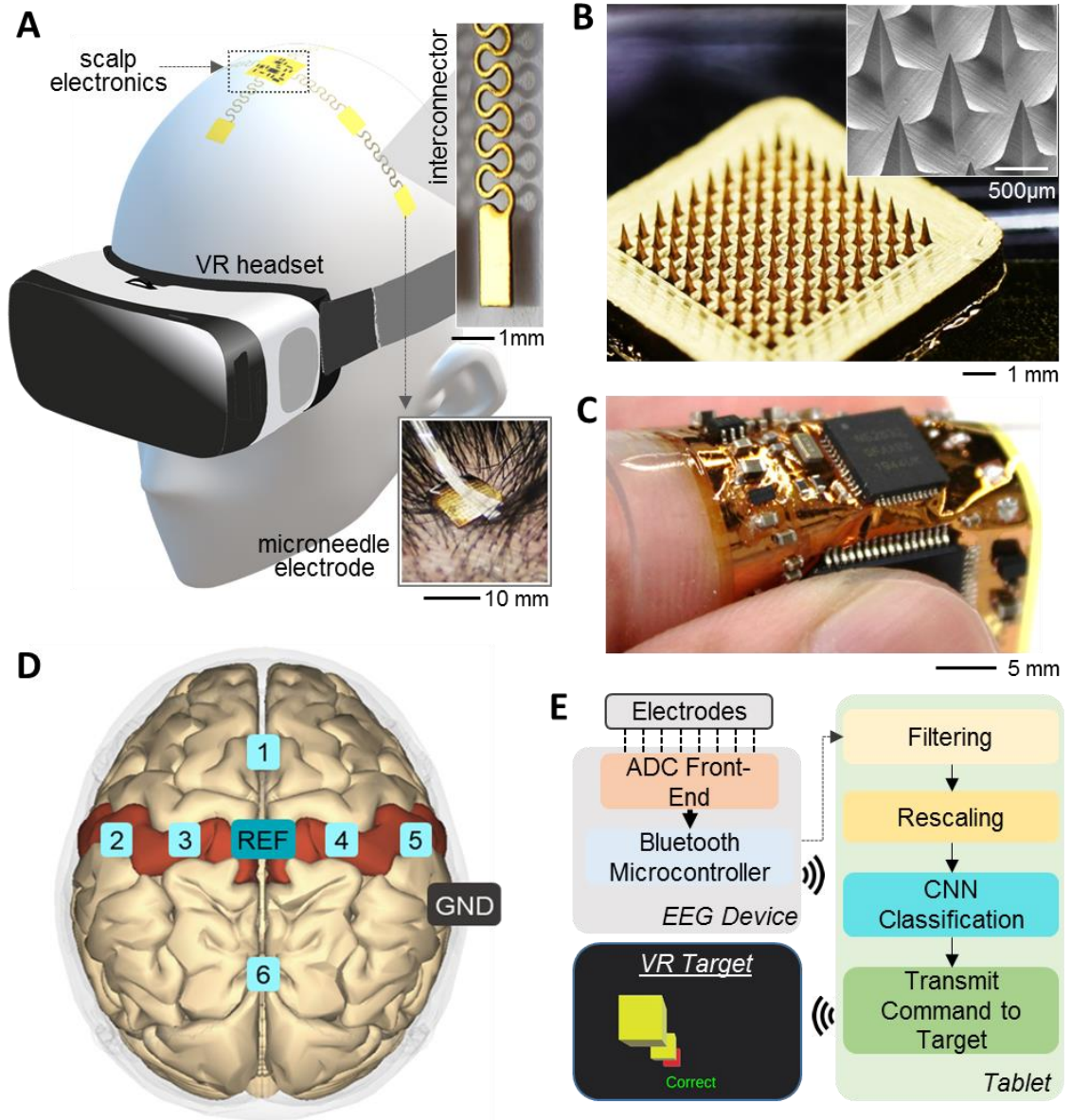


Figure 4. Overview of the wireless scalp system for motor imagery brain signal detection, featuring fully portable electronics, stretchable interconnectors, and flexible microneedle arrays. A) An illustration of a subject wearing scalp electronics and a VR headset with a close-up of stretchable interconnectors (top-right photo) and a flexible microneedle electrode (bottom-right photo). B) A zoomed-in photo of an array of microneedles along with a magnified SEM image of the needles (inset). C) A picture of a flexible wireless circuit with integrated chips, showing mechanical compliance of the membrane circuit. D) Locations (top view) of the microneedle electrodes for classification of motor imagery brain signals, including six recording channels, one reference (REF) and one ground (GND). E) A flow chart describing the entire data processing sequence from EEG recording to the control of targets in a virtual reality system via a machine learning classification algorithm (convolutional neural network, CNN).

As mentioned in Chapter 2, Motor imagery offers a strong stimulus-free paradigm for BMIs. The primary advantage is that there is no requirement for obtrusive stimuli in the way of the BMI user, resulting in more precise visual closed-loop interfaces. We demonstrate this principle by having subjects control a simple rhythm-based video game. Here, the interface's performance is greatly enhanced using soft, compliant electronics, flexible PI-based microneedles, allowing for reduced skin-electrode impedance density, resulting in improved SNR and classification accuracy. Virtual reality addresses subject variance in detectable EEG response to motor imagery by providing clear, consistent visuals and instant biofeedback. The combination with convolutional neural network-machine learning provides a real-time, continuous motor imagery-based brain-machine interface. With four human subjects, the scalp electronic system offers a high classification accuracy ($93.22 \pm 1.33\%$ for four classes), allowing wireless, real-time control of a virtual reality game.

3.2 Skintronics Concept and Design Principles

In conventional EEG, large rigid electronics and housings cause discomfort and inconvenience, long lead wires lead to motion and dragging artefacts, and finally, gel electrodes show significant depreciation in impedance and signal quality over time. The concept behind *Skintronics* is a fully flexible and fully conformal EEG system, aiming to improve on each of these points. First, miniaturization reduces noise sources by reducing the locations from which noise can be introduced, while also minimizing electrode leads and distance between the signal source and data acquisition device. When wires are used, only compliant, flexible and stretchable microfabricated interconnectors are used to prevent dragging or motion artefacts, as they stretch and bend with subject movement.

All electrodes are based on dry, capacitive measurement, and are optimized to flex in order to maximize contact on curved surfaces, such as the scalp.

Towards this end, we introduce *SKINTRONICS*, a skin-like flexible electronics platform, enabling seamless, portable EEG recording with enhanced signal quality performance over a multitude of commercial systems. An illustrative overview is presented in Figure 5. Addition of novel time-domain analysis using convolutional neural networks allows for real-time, accurate classification of various SSVEP and MI data, as will be shown in later chapters. As previously mentioned, the philosophy of this design includes application of all-flexible components and reduced size, weight and distance between components in order to significantly reduce locations where noise could be introduced and insulated the device components from noise sources.

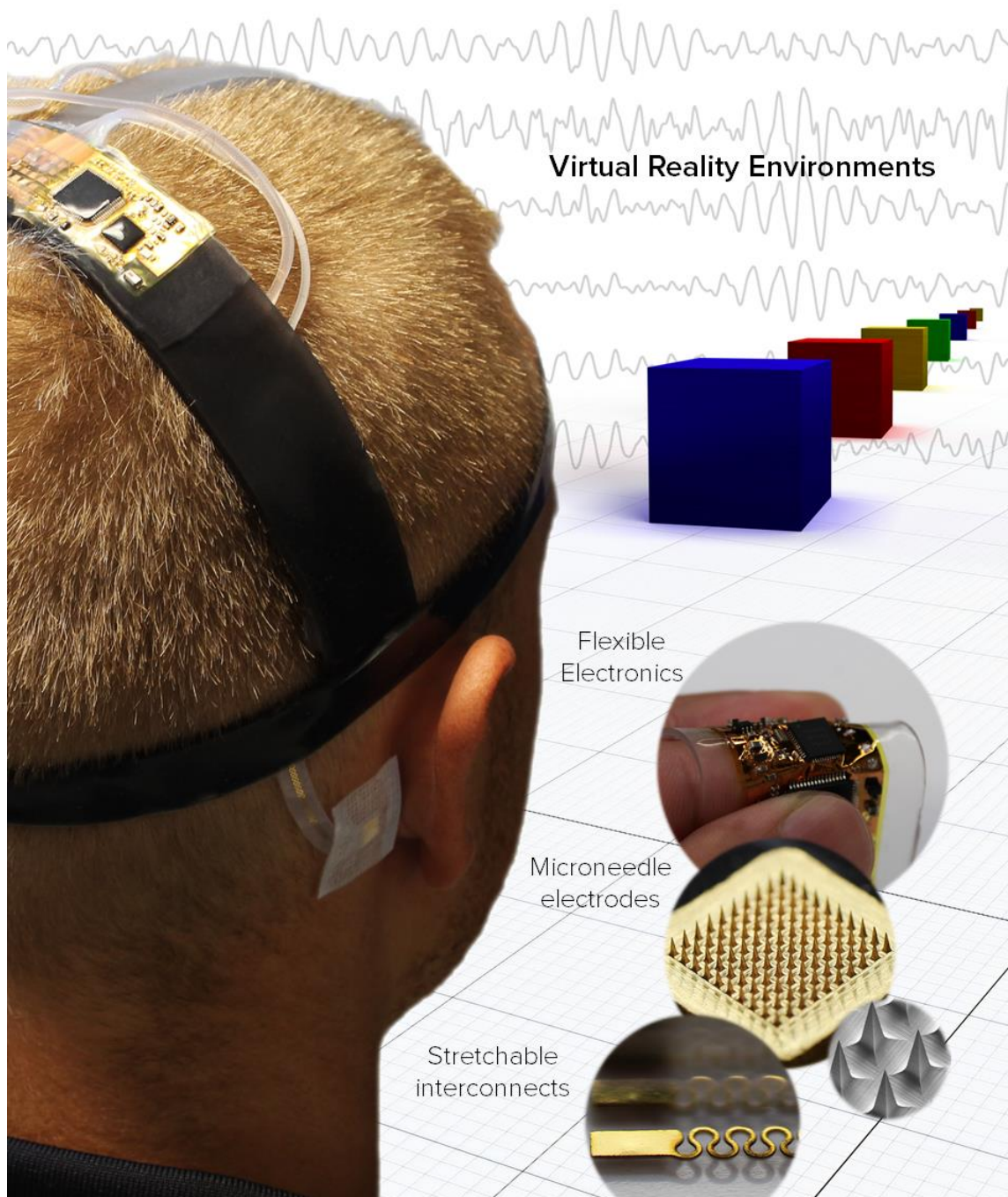


Figure 5. An illustrative overview of the *Skintronics*-based BMI. Subjects are trained on various BMI paradigms in an immersive virtual reality environment and wear a minimalist headgear with flexible hybrid electronics for the data acquisition, with flexible microneedle electrodes, and stretchable interconnectors.

3.3 Methods for MI-based BMI

3.3.1 *Electrode reduction via input perturbation analysis*

As described in the literature review, motor imagery activity is primarily focused in the motor cortex region, requiring electrodes in various locations of the temporal lobe. As mentioned in the stated goals of this research, reducing the system complexity is a desired goal, and reducing the number of required measurement electrodes is a process towards that end. However, this is largely non-trivial. Some of the best performance from MI interfaces comes from large EEG clusters of a dozen or more electrodes. In this section, demonstration of reduction of number of measurement electrodes through the analysis of large EEG clusters using input perturbation analysis is discussed.

44-channels data out of 128 channels from 13 subjects were considered, as performed in the prior work (High-Gamma Dataset) [16]. A flow-chart demonstrating the data flow process is shown in Figure 6. The full dataset is simply preprocessed using a 3rd-order Butterworth bandpass filter, with corner frequencies at 4 Hz and 30 Hz, and split into windows of 4 seconds (Figure 6A). A convolutional neural network (CNN) with standard convolutions on the first layer, with a filter size of (10, 1), followed by four spatial convolutional layers, is used to train the full dataset (Figure 6B). A generator then cycles through the data channels, eliminating the remaining channels in order to calculate the output perturbation on the selected channels (Figure 6C). This data is then fed into the trained network, and the output perturbations are compared (Figure 6D) with the true expected outputs to generate the relative perturbations for that channel (Figure 6E). These relative perturbations are summed by the channel to generate a final perturbation value

(Figure 6F), for each of the channels to be compared and ranked, as demonstrated in (Figure 6G). These electrode positions correspond with custom positions on the 128-channel system (waveGuard, ANT Neuro) used in the referenced paper [16].

The classification accuracy for 44 channels was $84.88 \pm 2.30\%$. Using the input perturbation analysis described, the classification accuracy was calculated again using the top-6 and top-4 channels with the same network architecture, resulting in accuracies of $81.70 \pm 3.17\%$, and $78.70 \pm 2.87\%$ (Figure 7). The final electrode positions for our main study was based on analysis of this and other public motor imagery datasets, as well as some empirical experimentation to determine the optimal 6-electrode setup, shown in Figure 8. The approximate positions of the electrodes corresponding with the standard 10-10 electrode placement system [54] are Fz, C5, C3, C4, C6, and POz, with the reference electrode at Cz, and the ground electrode placed at the mastoid. This setup is optimized for capturing event-related synchronization and desynchronization relating to separate hands and both feet, as well as capturing overall alpha rhythm activity. The setup was determined to reduce the number of electrodes and complexity of the setup as much as possible without significant reduction in classification performance.

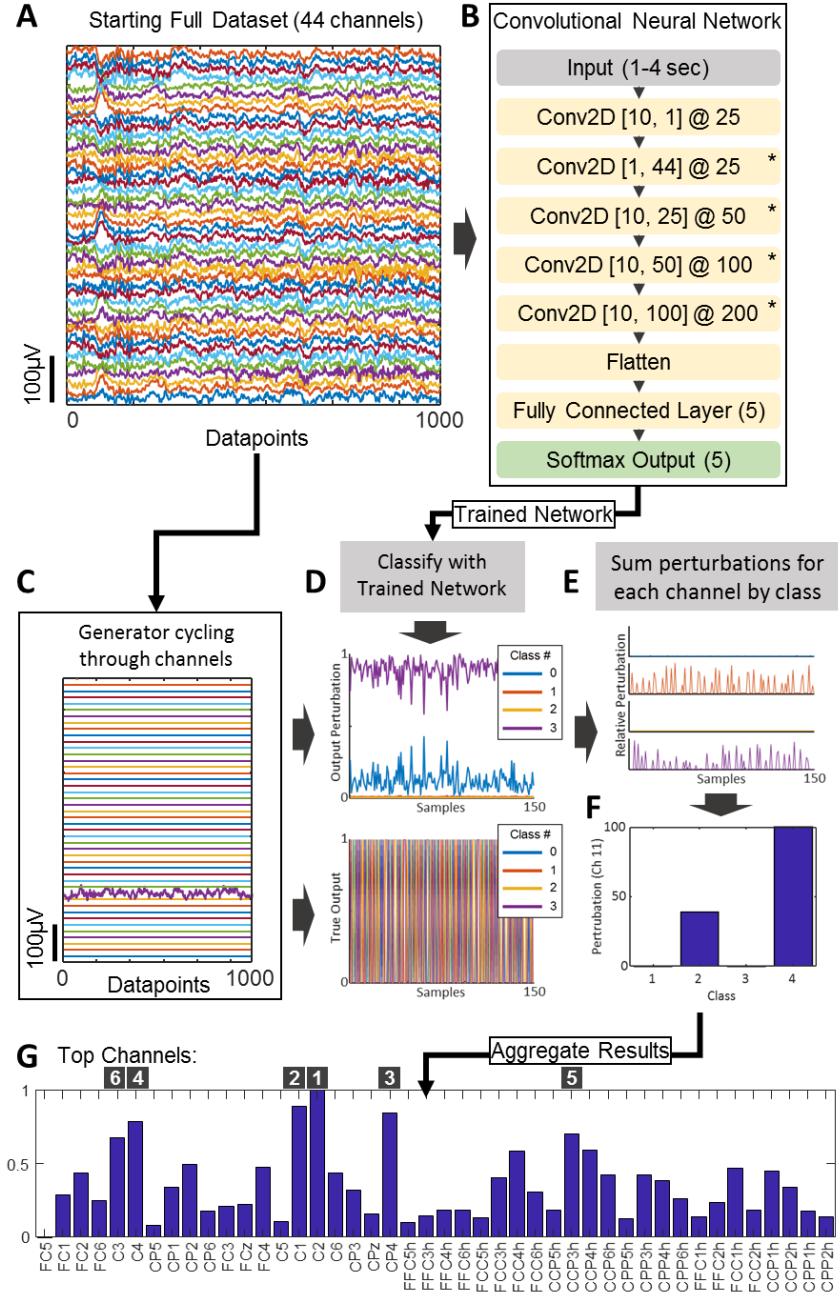


Figure 6. Optimized channel selection process. (A) A complete 44-channel MI dataset is (B) trained on a spatial-CNN model. (C) A generator is used to cycle through the channel, setting the remaining channels as inactive, and (D) passed through the trained classifier. (E) The output perturbations are then compared with the true outputs, resulting in the relative perturbation, (F) which is summed over the classes to get the per-class perturbations for each channel. (G) A bar chart of each channel's relative perturbations is shown with the top-6 channels labeled.

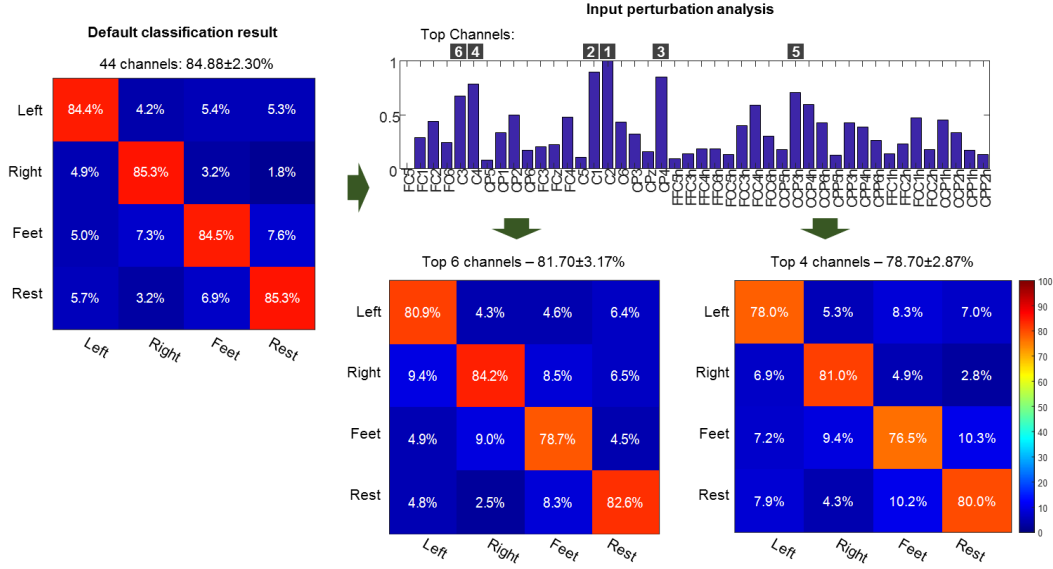


Figure 7. Demonstration of channel reduction based on input perturbation analysis. Using a known dataset of 44 channels (left), we perform input perturbation analysis and rank the top-6 and top-4 channels (right), demonstrating the results of $81.70 \pm 3.17\%$ from the top-6, and $78.70 \pm 2.87\%$ from the top-4; a relatively small performance penalty based on the original $84.88 \pm 2.30\%$ from 44 channels.

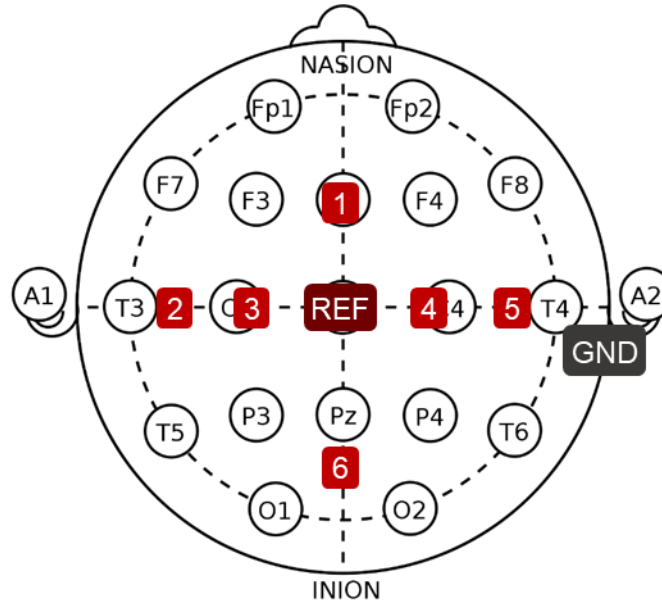


Figure 8. Locations of electrodes, including Fz, C5, C3, C4, C6, and POz, with the reference electrode at Cz, and the ground electrode placed at the mastoid.

3.3.2 Flexible microneedle electrodes

Here we introduced the components for the *Skintronics* fully portable scalp-based electronics system optimized for capture of motor imagination data. The component interfacing the human body with the electronics is the electrode, therefore it was the component of primary focus. The objective was to reduce electrode impedance density, a relative measure of impedance based on surface contact area typically measured in $\text{k}\Omega\cdot\text{cm}^2$. Here, we introduce a novel flexible microneedle electrode design (FMNE). In this study, we compared performance of conventional paste-based EEG electrodes with optimized dry electrodes. This serves to demonstrate advantages of using dry electrodes on hairy scalp areas. Optimal parameters for potential microneedle electrodes were selected based on a review of literature (Chapter 2), and experiments varying parameters on a square-pyramid needle design (summarized in Table 1).

Table 1. Comparison of impedance and impedance density of microneedle electrodes of varying height, with fixed base width of $200\mu\text{m}$, and pitch of $500\mu\text{m}$ (14×14 array).

Electrode	500um MN	600 μm MN	700 μm MN	800 μm MN	MVAP electrode	Flat gold film
Area (mm^2)	49	49	49	49	96	49
Impedance ($\text{k}\Omega$)	43.6	35.7	29.7	23.3	20.8	129.3
Impedance Density ($\text{k}\Omega\cdot\text{cm}^2$)	21.4	17.5	14.6	11.4	20.0	63.4

The determined optimal parameters include a high-aspect-ratio needle of a square-pyramid shape with a height of $850\mu\text{m}$ and base width of $350\mu\text{m}$. This design allows for successful penetration of the stratum corneum, significantly reducing contact impedance, and reducing variance of surface skin condition. An array of FMNEs are constructed via

a micro-replica-molding process on polyimide, followed by a coating of thin-film conductive metals (Cr and Au). The fabrication process is discussed in the following subsection and illustrated in Figure 9 with photos of the process and close-up photos of the finalized microneedle electrodes in Figure 10.

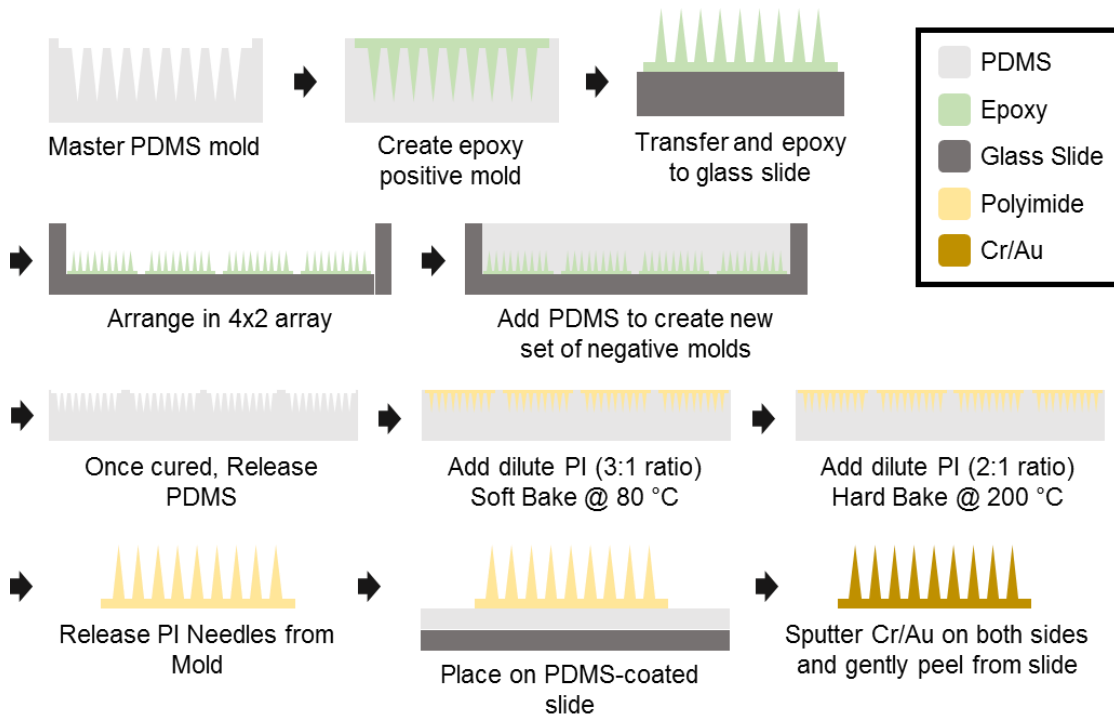


Figure 9. Fabrication process of an array of flexible microneedle electrodes

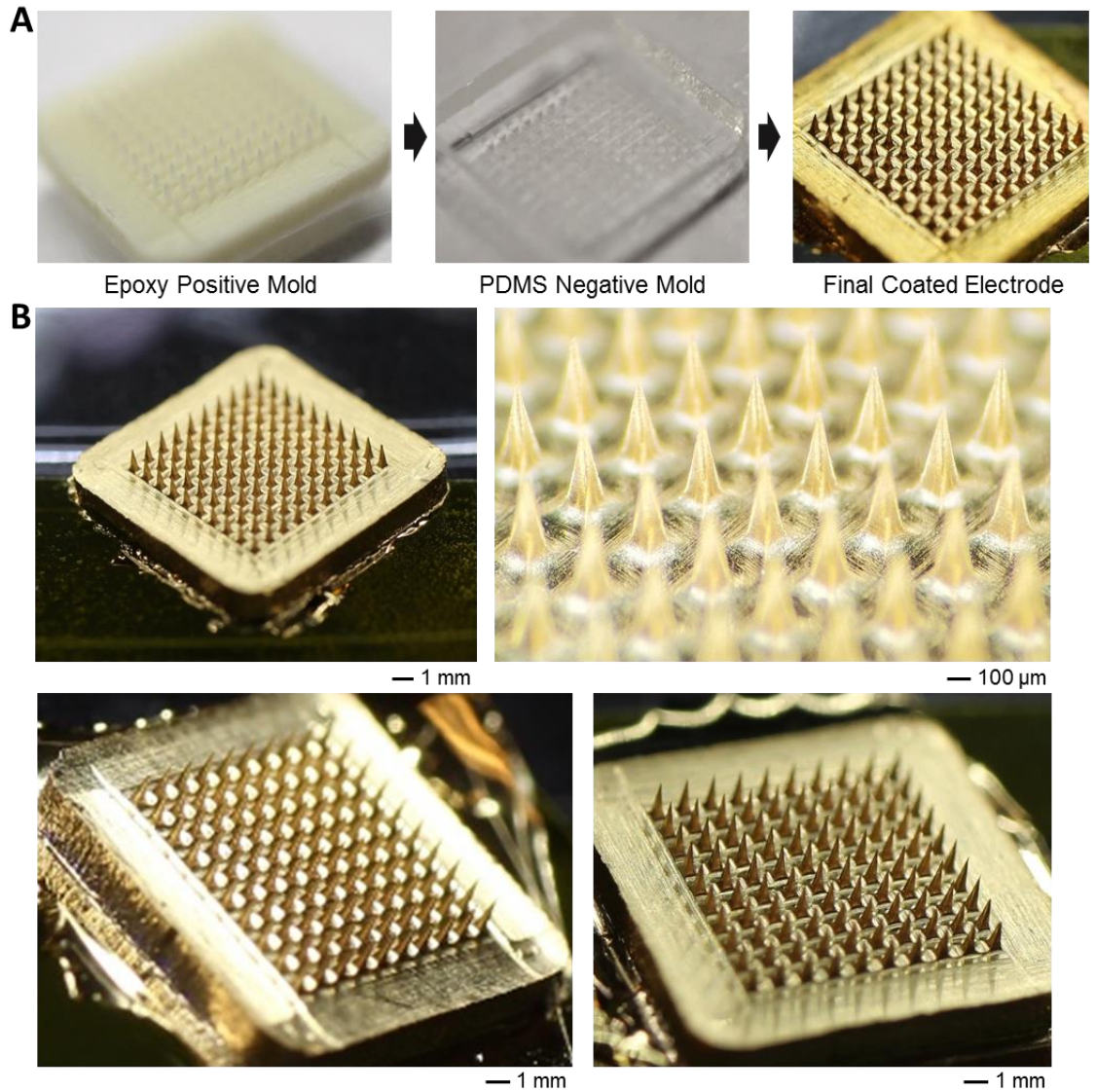


Figure 10. (A) Photos of electrode fabrication processes and (B) a collage of optical images of the finalized electrodes from various angles. The impedance and impedance density of microneedles are summarized in Table 1.

Fabrication of flexible microneedle electrodes

Fabrication involves cleaning a negative PDMS microneedle array mold (MicroPoint, Singapore) with IPA and drying at 60 °C for 10 minutes. Positive mold is made from negative PDMS mold using epoxy resin (ExpoxAcast, Smooth On, Inc). From the epoxy resin positive mold, arrays of multiple PDMS (Sylgard 184, Dow Corning)

negative molds are made in order to increase production throughput. PDMS negative molds are bonded to glass slides using a thin layer of PDMS. PDMS molds are then treated with ambient air plasma for 2 minutes. From here, polyimide (PI 2610, HD Microsystems) diluted at a ratio of 4:1 in N-Methyl-2-pyrrolidone are applied and cured in very thin layers. The PI is compressed flat in the mold with a small fitted weight. The layers are then soft-baked at 100°C for 10 minutes, and hard-baked at 200°C for 1 hour before applying a new coating of PI. This process is completed for a total of four layers, before the PI flexible microneedle array can be removed from the mold. Last, Cr/Au (5 nm/200 nm) is sputtered on both sides of the needles in order to produce the final needles. The entire process takes over 6 hours for a set of 16 needles, making the throughput relatively low for a micro-replica molding process. Improvements to microneedle production using process and material optimizations are discussed in later chapters.

Flexible microneedle electrode performance assessment

Experimental studies demonstrate the mechanical and electrical characteristics of the fabricated FMNE. High resolution close-up photos are given in Figure 12, showing the needle tip, before and after tissue insertion. In this study, a porcine skin was used to test the mechanical robustness with 100 insertions. Aside from cosmetic blemishes due to porcine tissue fluids, the FMNE tips' shape and electrical coating remained intact. A quantitative mechanical test in Figure 13 validates the SEM observation by measuring the required fracture force in buckling. A total of five fabricated FMNEs could withstand an averaged applied force up to 626 mN, which is well above the skin insertion force (20 – 167 mN) of a single microneedle [55, 56]. Another mechanical test of cyclic bending of

FMNEs (Figure 11) supports the mechanical robustness in tissue insertion. The needle electrode was continuously bent up to 100 times with a radius of curvature of 5 mm while measuring the change of electrical resistance. The result shows a negligible resistance shift of less than 0.6 Ω . The prior works [25, 57] proved that gold-based electrodes, mounted on the skin surface, are safe to use due to their excellent biocompatibility.

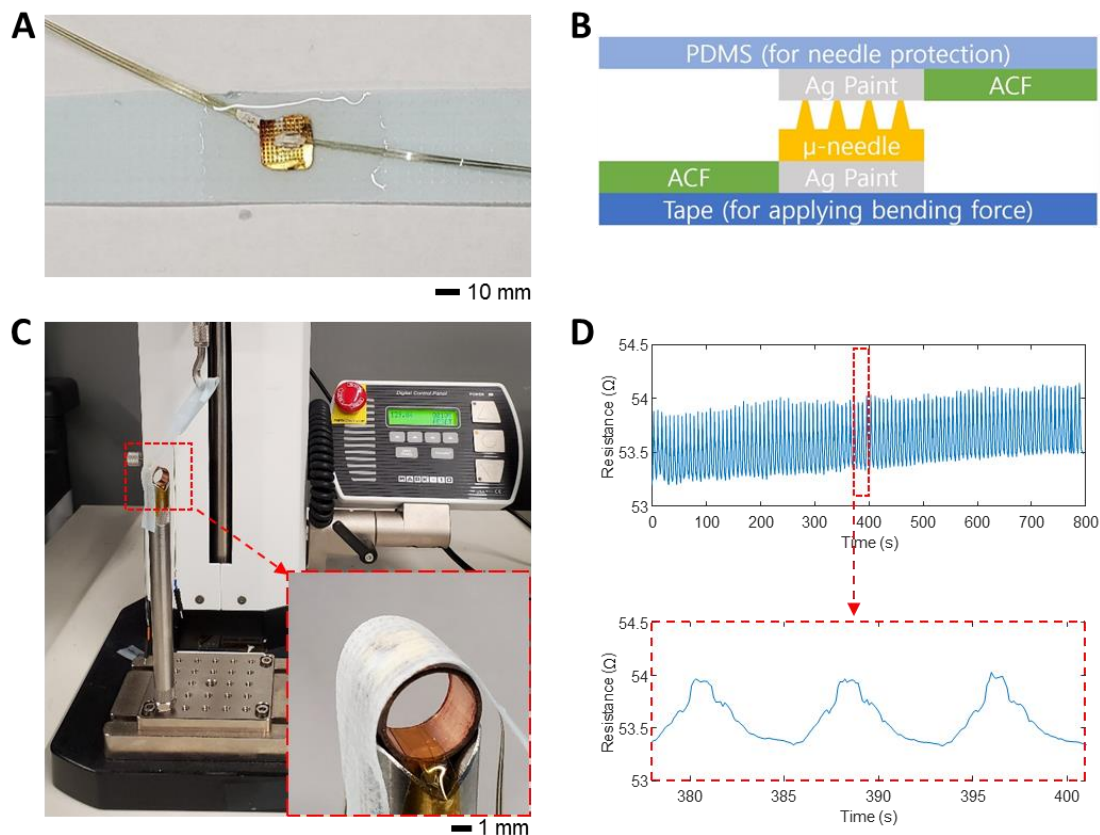


Figure 11. Flexibility evaluation of a microneedle electrode. (A) Photo of a test specimen structure for microneedle electrode cyclic bending test. (B) Schematic of a cross-section of the test specimen. (C) Picture of cyclic bending test setup in which the motorized testing rig continuously bends and un-bends the test specimen over a cylinder with a 5 mm bending radius. (D) Resistance data over 100 bending cycles (top), and a close-up of data over three cycles (bottom), showing the minimal fluctuation of resistance in the microneedle electrode.

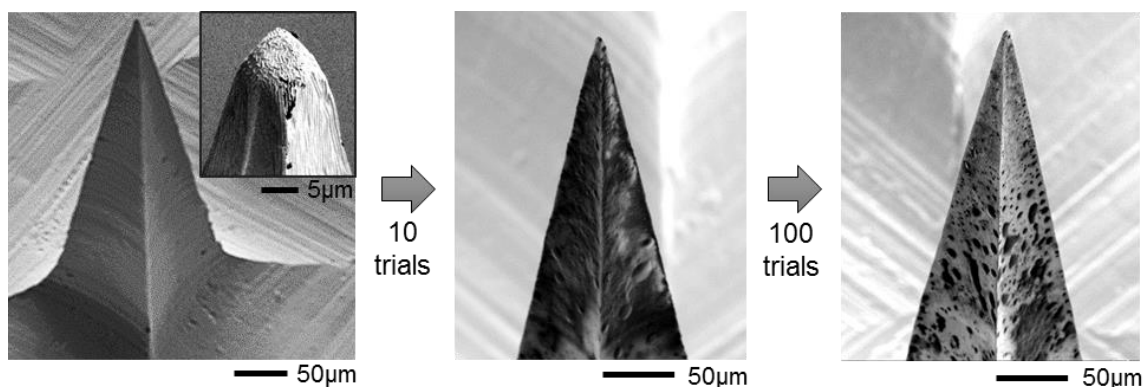


Figure 12. A series of SEM close-up images microneedle electrode tip: unused (left, inset: zoom-in view of the tip), after ten insertions into porcine skin (middle), and after 100 insertions into the tissue (right).

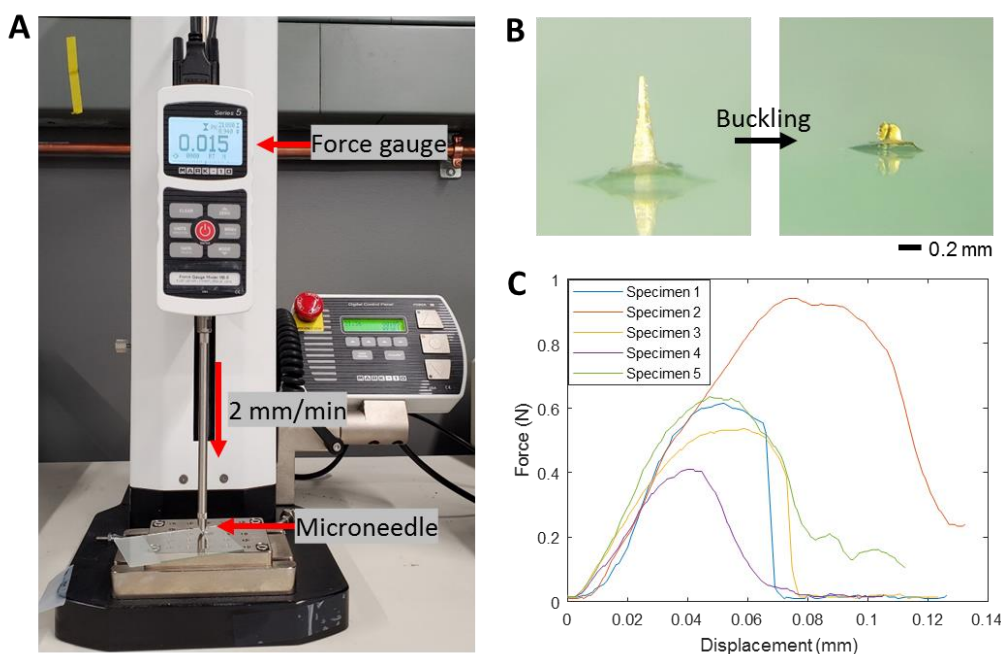


Figure 13. Buckling force evaluation of a single microneedle electrode. (A) Buckling force testing setup in which the motorized force gauge applies an axial force upon a single microneedle electrode and measures the axial force until its fracture. (B) Photos of a single microneedle before (left) and after (right) the buckling test. (C) The buckling test data of five different single microneedle test specimens where buckling fracture begins at the peak force value.

An additional experimental study was conducted to validate the safety of skin-penetrating electrodes, FMNE, via a cytotoxicity test (details in Figure 14). An additional

48-hour test on human skin is performed to demonstrate minimal skin immune reaction, with skin redness fading after 1 hour (details in Figure 15). Human keratinocytes were seeded on the electrodes and cultured for over five days. For the immunofluorescent labeling, cells were fixed and incubated with Alexa Fluor 555 Phalloidin and Hoechst for two hours, and the cytotoxicity was quantified with a PrestoBlue Cell Viability reagent. The summarized results show that the difference in cell densities and morphologies between the control and a gold coated FMNE is negligible. Also, the measured cytotoxicity between the two samples shows no significant difference, capturing the electrodes' safety for human study.

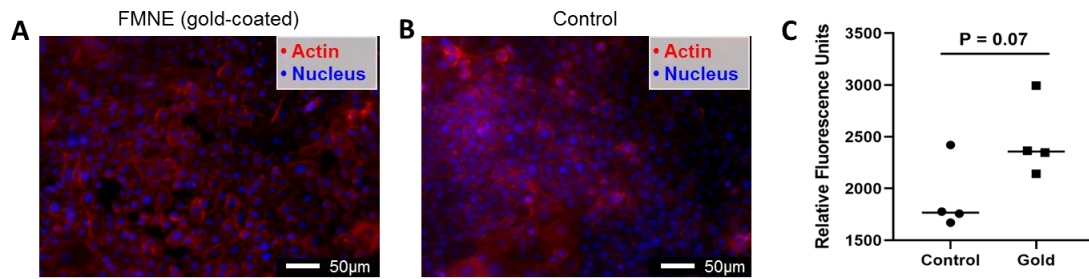


Figure 14. Cytotoxicity results. (A) Immunofluorescent Hoescht labeling of human keratinocyte cells after 5-day culture experiment in contact with Gold-coated FMNE electrode. (B) Control experiment data of immunofluorescent Hoescht labeling of human keratinocyte cells after 5-day culture. (C) Fluorescence measurements that quantify cytotoxicity with cell viability reagent for FMNE electrodes vs. control.

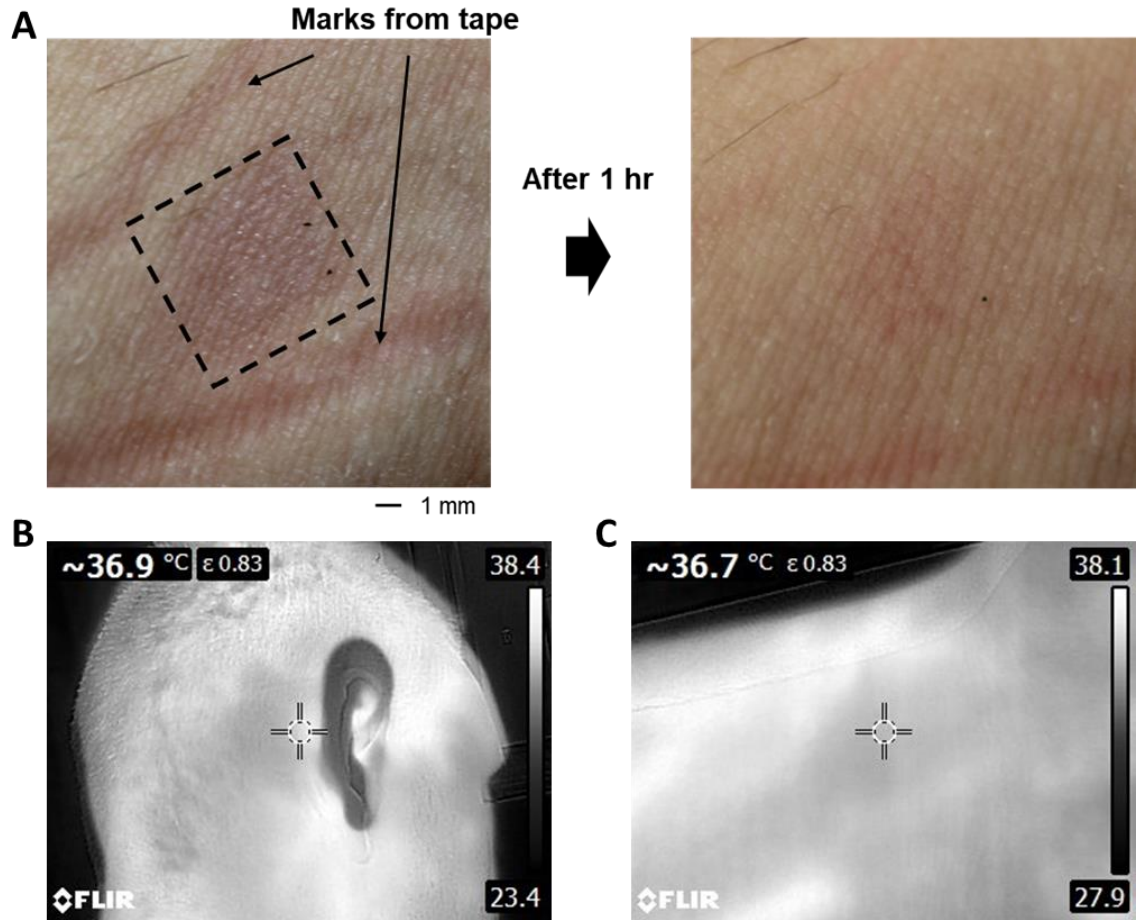


Figure 15. Microneedle electrode wearing results. (A) Photo of redness on skin after 48-hours continuous wear of gold flexible microneedle electrode (left) and fading redness after 1-hour post release (right). (B) Thermal image (FLIR) showing skin temperature after 1 hour of wearing microneedle electrode behind the ear. (C) Thermal image showing skin temperature after 48 hours of wearing microneedle electrode on the skin (wrist).

For a high-quality recording of brain signals, the impedance between the electrode and skin should be low, demonstrating an intimate contact. Two types of electrodes (FMNE and conventional Ag/AgCl) were utilized in this study by mounting both on human subjects' scalps. As summarized in Figure 16A and Figure 16B, the FMNE could maintain the skin-electrode contact impedance levels even after one hour of continuous use in EEG detection. The impedance density (ID , $k\Omega\text{-cm}^2$) was calculated by using the measured impedance (Z , $k\Omega$) and contact area (A , cm^2): $ID = Z * A$. To prove the

enhanced performance of the FMNE in EEG recording, two types of electrodes were used to measure signals on POz and Cz for two minutes simultaneously. The recorded alpha rhythms (Figure 16C) show an average signal-to-noise-ratio (SNR) of 13.7 ± 2.6 dB (top graph) and 9.9 ± 1.8 dB (bottom graph) for a dry FMNE case and a wet Ag/AgCl cup electrode with conductive paste, respectively. Overall, the skin-penetrating FMNE shows more reliable, higher performance signal recording than the conventional, gel-based metal electrode.

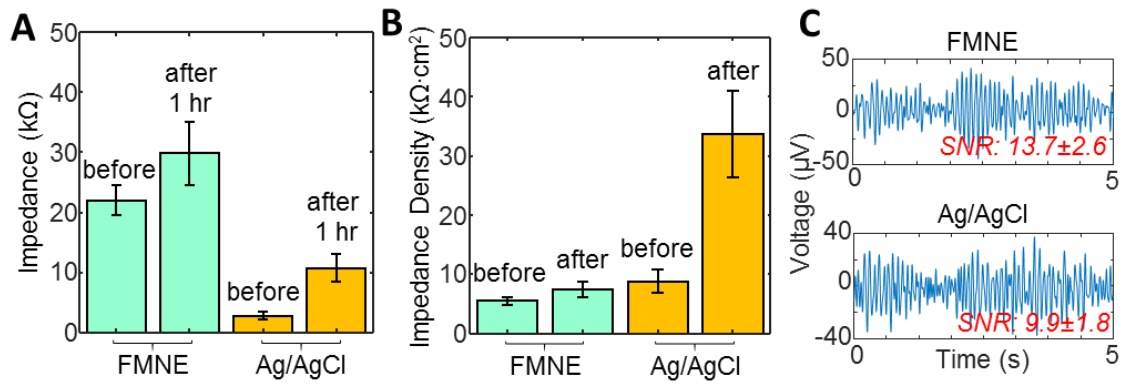


Figure 16. A) Skin–electrode contact impedance that compares the performance between FMNE and conventional Ag/AgCl cup electrodes (error: standard deviation with $n = 4$ subjects). B) Calculated impedance density from data (A), showing a dramatic increase of the impedance change from the conventional electrode. C) SNR comparison of EEG alpha rhythms measured by FMNE (top) and conventional Ag/AgCl electrodes (bottom).

3.3.3 Flexible and stretchable interconnects

As mentioned in the literature review and problem statement, a longstanding and unresolved problem of EEG design involve motion artefacts introduced in lead wires. These artefacts are introduced downstream of the signal source and are therefore difficult to manage. Apart from circuit-related solutions (i.e. use of active electrodes), and design-based solutions (size reduction, eliminating free-standing wires and high levels of

integration), there is additional opportunity to reduce noise through redesign of interconnects between the electrode and data acquisition circuit. Here, we introduce a novel flexible and stretchable interconnector designed to reduce motion noise and allow for significant mechanical compliance, reducing sources of noise from mechanical stressors.

The fabrication of a stretchable interconnector uses a micro-machining process with a femtosecond laser cutter (WS-Flex USP, OPTEC), which offers higher throughput and lower cost than the conventional microfabrication in a cleanroom. A substrate for the interconnector is prepared by an electron-beam evaporating Cr/Au (5nm/200nm) on a 2-mil PI film (200HPP-ST, DuPont). The metal-coated PI film is then laminated on a PDMS-coated PET film to hold the material during the laser cutting process. Once an array of stretchable interconnectors is patterned on the metal-coated PI film, excess materials other than the patterned interconnectors are manually peeled off from the PDMS-coated PET film. With water-soluble tape, the interconnectors are transfer-printed on a soft elastomer substrate (Ecoflex 00-30, Smooth-On, Inc.), and areas other than their contact pads are encapsulated with an additional layer of elastomer. The interconnectors are electrically connected to the electrode and sensor with silver paint (Fast Drying Silver Paint, Ted Pella). An illustration of the fabrication process is shown in Figure 17.

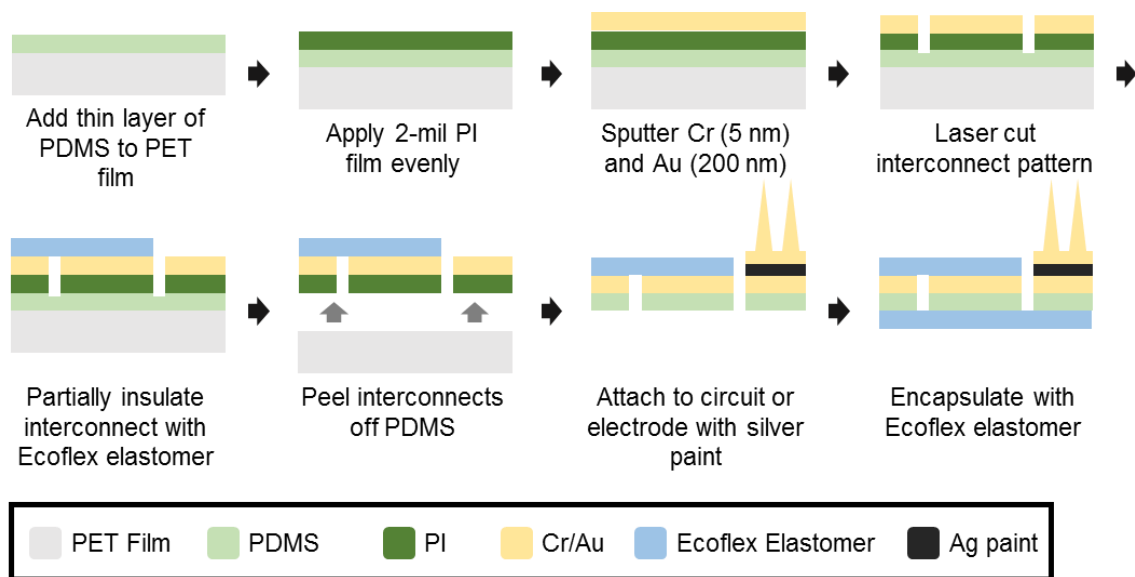


Figure 17. Overview of stretchable interconnector fabrication process.

Analysis of stretchable interconnector performance

Photos in Figure 18A capture the stretchability of up to 100% strain that the fabricated interconnector can manage without plastic deformation. With the help of an out-of-plane buckling, the thin-film connector, enclosed by a low-modulus elastomer, shows mechanical reliability upon cyclic stretching when measured by a digital force gauge (EMS303, Mark-10) and a multimeter (DMM7510, Tektronix). Details of the mechanical testing method appear in Materials and Methods. The result in Figure 18B shows the change of electrical resistance of the interconnector with an applied tensile strain of 60% and 100 cyclic loadings; each full cycle takes ~15 seconds (Figure 19). The level of resistance fluctuation during cycles was very consistent with less than 60 mΩ change, and the total resistance change after 100 cycles is about 70 mΩ. In addition, the interconnector's end-to-end resistance was monitored during a maximum strain test. As shown in Figure 18C, the stretchable connector shows a yielding after 200% strain, which

is eventually fractured at $\sim 275\%$ strain. Close-ups of the interconnect wire at the maximum strain in Figure 20 captures the failure point close to the contact pads. Overall, the presented data set demonstrates a reliable mechanical performance of the stretchable interconnector that integrates multiple sensors with a wireless circuit. The maximum stretchability is well beyond what would be realistically expected from the scalp-wearable application [4, 58].

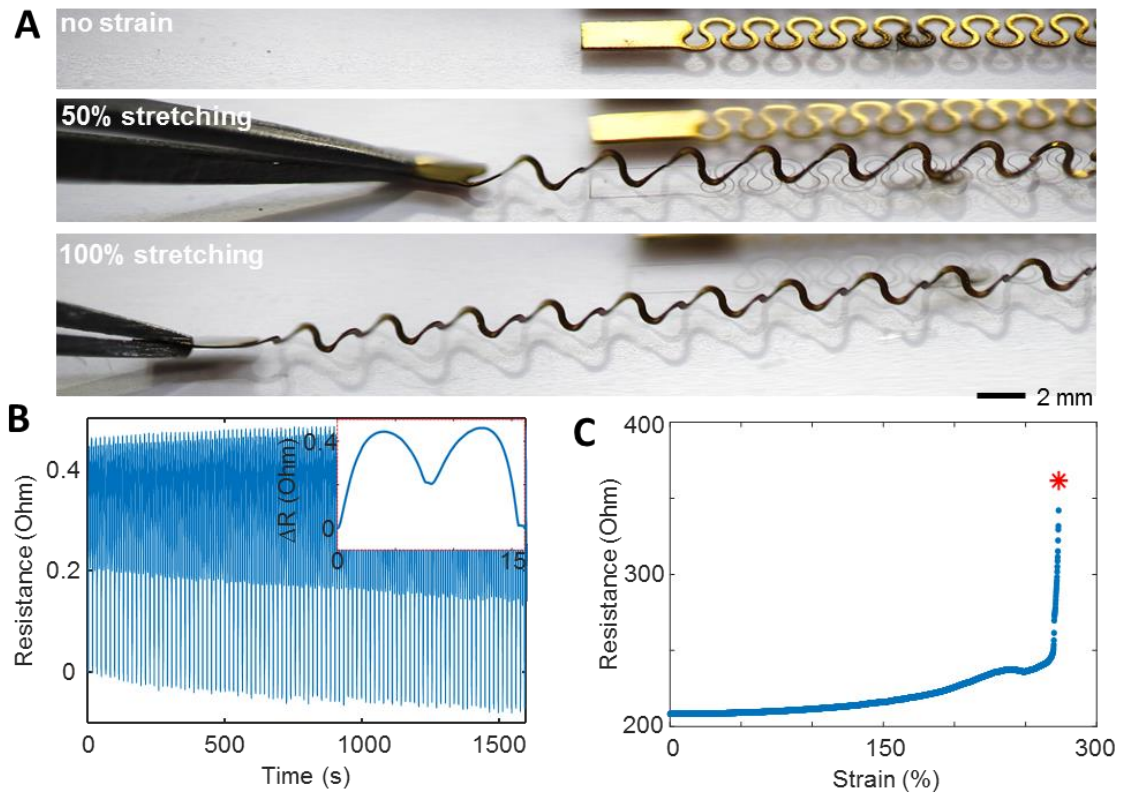


Figure 18. Characterization of stretchable EEG interconnectors. A) Photos of stretching of a stretchable EEG interconnector up to 100%. B) Electrical measurement of resistance change of the interconnector with 60% strain for 100 cycles, showing negligible changes in resistance. The inset shows the resistance change over a single stretch cycle. C) Measurement of electrical resistance change of the interconnector, showing mechanical fracture after 250% of tensile stretching.

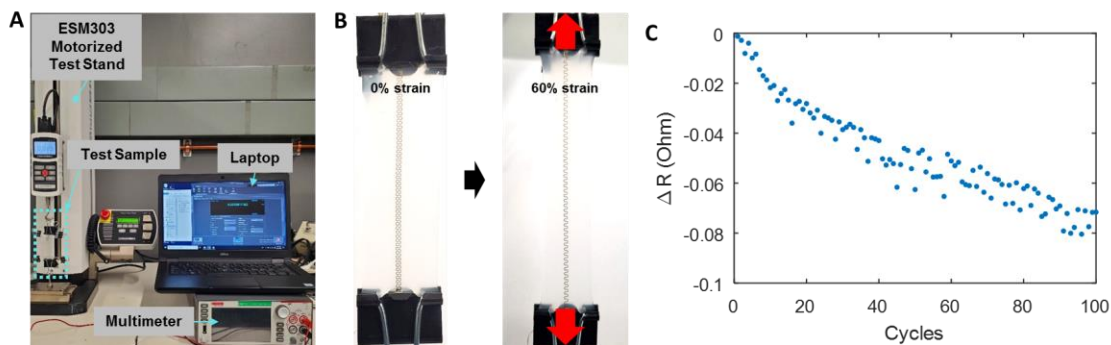


Figure 19. Experimental setup of a stretching test. (A) Motorized test stand (ESM303, Mark-10), multimeter, and laptop data acquisition setup for stretch testing of stretchable interconnects. (B) A two-inch segment of stretchable interconnects secured between two binder clips pre-strain (left), and at 60% strain (right). (C) Change in resistance over 100 stretching cycles with 60% strain.

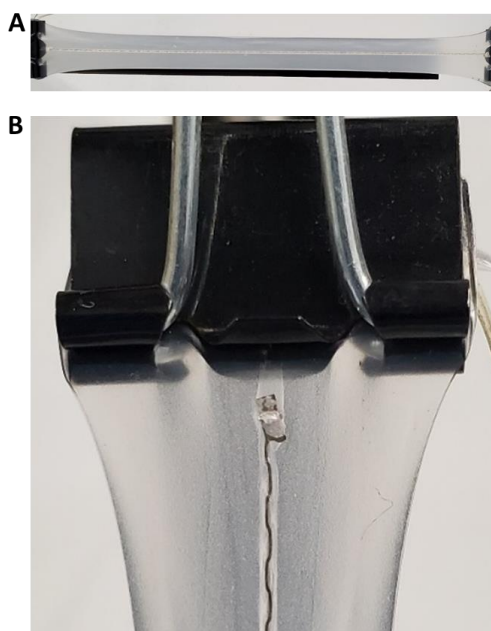


Figure 20. Close-up photos of a flexible interconnector with an excessive strain. (A) An entire view of an interconnector at 275% strain. (B) Close-up of the failure point near the contact pad.

The primary drawback of this design is the fact that it tangles easily and often, resulting in difficult handling. In order to prevent issues tangling during setup, they are coated in elastomer, resulting in excessive motion artefacts, which would be much

reduced without the elastomers. These issues are addressed in a later chapter with a tangle-free design.

3.3.4 Flexible Skintronics data acquisition device

The fabrication process for the data acquisition component of the *Skintronics* interface is detailed in Figure 21. The flexible wireless circuit maintains functionality even with an excessive bending up to 180 degrees with a radius of curvature of 1.5 mm, which is supported by both computational and experimental studies (Figure 22A–C). More importantly, this device shows robust mechanical reliability from an experimental study with 100 bending cycles, quantitatively measured by the change of electrical resistance (Figure 22D–E).

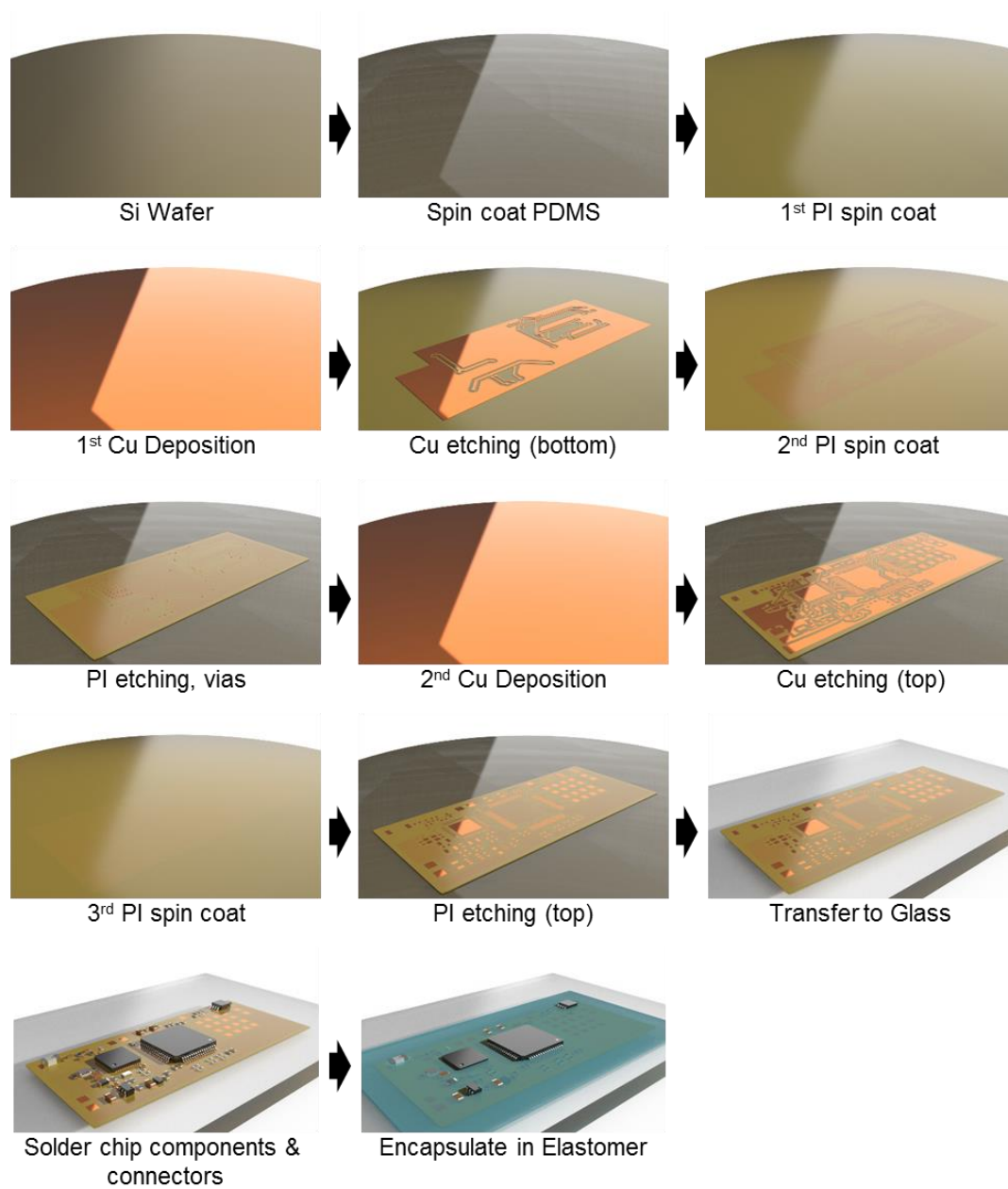


Figure 21. Fabrication process of a flexible wireless *Skintronics* circuit using conventional cleanroom fabrication techniques.

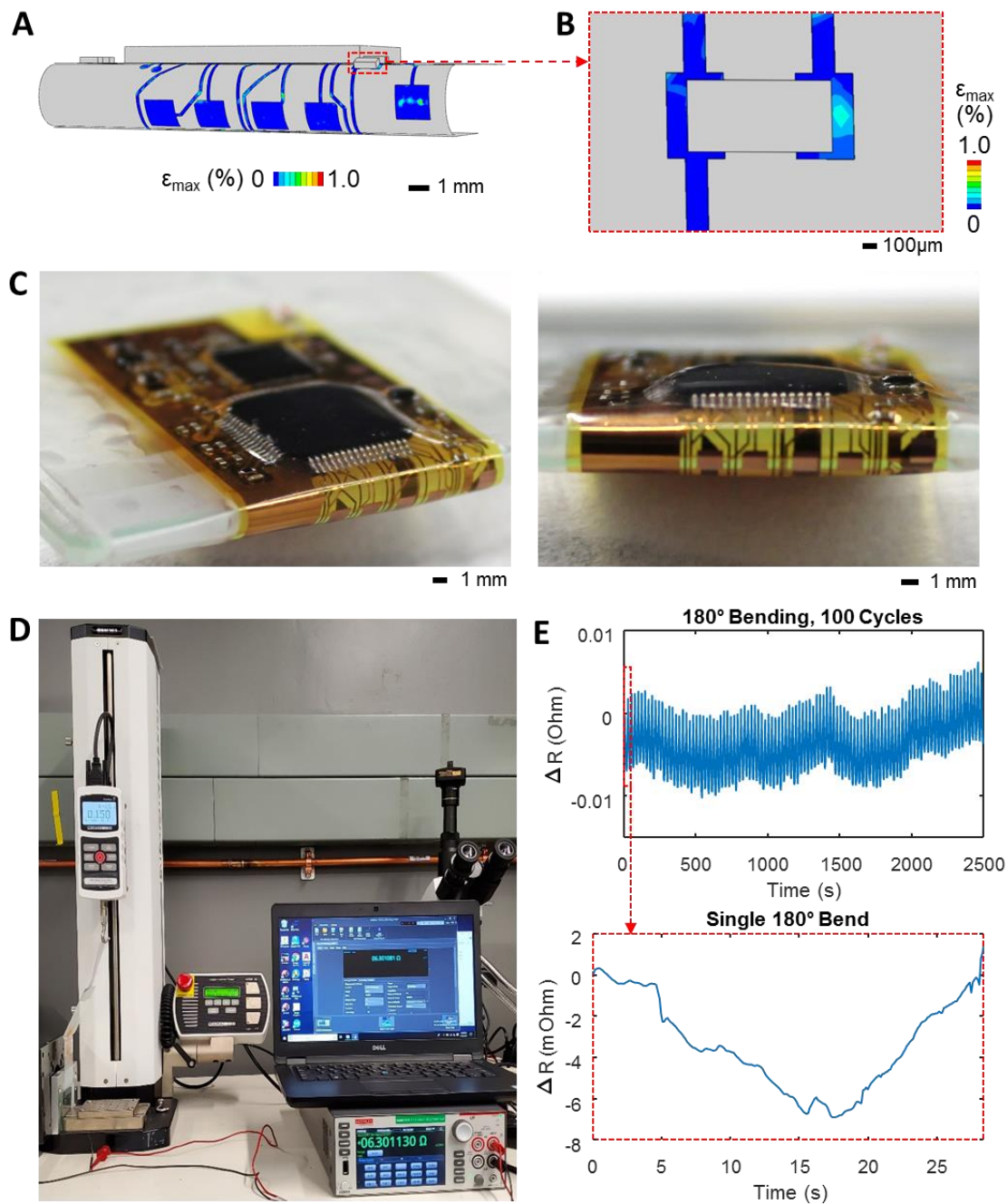


Figure 22. Mechanical characterization of a flexible circuit. (A) Computational mechanics modeling data of a circuit bent at the location with components and interconnects, demonstrating 180° bending with a radius of curvature of 1.5 mm. (B) Close-up area from (A). (C) Photos of a circuit undergoing bending by following the computational modeling. (D) Mechanical test stand setup for cyclic bending, with multimeter and laptop for measuring resistance. (E) Resistance data over 100 bending cycles (top), and a close-up of data over a single cycle (bottom), showing the minimal fluctuation of resistance.

3.3.5 *Experimental setup*

Three MI tasks were included in the experimental classes as well as alpha rhythms (the subject has eyes closed) for a total of four classes towards controlling our interface. Alpha rhythms were used as a null class in tasks where the subject wanted to pause control over some target. For the non-VR examination, subjects were asked to imagine the actions of opening and closing their hands, as well as depressing a pedal with both feet in the first person for the tasks. With the VR examination, the subjects were provided with clear visual guidance on what they should be imagining, using animated disembodied limbs within the normal field of view that a subject could view their own limbs. When recording with conventional Ag/AgCl electrodes, each subjects' skin was cleaned by gently rubbing with an alcohol wipe, and dead skin cells were removed using an abrasive gel (NuPrep, Weaver and Co.) in order to maintain a contact impedance below 10 k Ω on all electrodes. The abrasive gel was removed using an alcohol wipe and the surface dried using a clean paper towel. On the other hand, for the FMNEs, the only skin preparation conducted was a gentle rub of the electrode location with an alcohol wipe. The EEG data were recorded using a custom application running on an Android Tablet (Samsung Galaxy Tab S4), using Bluetooth Low Energy wireless communication. This study was conducted by following the approved IRB protocol (#H19553) at the Georgia Institute of Technology. For all experiments, data were sampled at 500 Hz, and down sampled to 250 Hz for analysis and classification. Training data involves continuous recording of a single task for one minute. The subject begins with their eyes closed to target alpha rhythms. After one minute, an auditory cue lets the subject know to open their eyes; then, they may watch for visual cues to follow the MI instructions. Two

seconds of training data were discarded between each class to allow the subject time to react to the new cues. For all four classes, this process takes four minutes per trial, and the process is the same with and without the use of a VR headset. To train the SVM and CNN models, training data were subdivided into window sizes of 1, 2, and 4 seconds to gauge accuracy over multiple window sizes, with 50% overlap between consecutive windows. There are approximately 112 4-second samples per trial for the training set for a total of 560 samples per subject. Therefore, there are 2240 samples for all four subjects.

3.4 Preprocessing and classification of MI brain activity with CNNs

Recent studies in multichannel, MI EEG classification suggest that using CNNs on preprocessed time-domain data provides the most accurate results [16, 59-61]. For validation of the machine-learning performance, we compared CNNs with conventional feature-extraction methods via power spectral density analysis (PSDA) and support vector machines (SVM). Two types of spatial CNN (Figure 23A) and conventional CNN (Figure 23B) methods were also compared since spatial convolutions to classify multiclass MI data was introduced by a recent study (17). We used data recorded from four subjects using FMNEs, preprocessed via a bandpass filter (3rd-order Butterworth, 4 – 33 Hz). The spatial CNN method achieved very high accuracy ($93.22 \pm 1.33\%$), whereas the standard CNN performed poorly in direct comparison ($68.51 \pm 3.89\%$), as shown in Figure 23C–D. This result suggests that the spatial-CNN method's modified architecture is better at extracting spatial information features from the multichannel MI data.

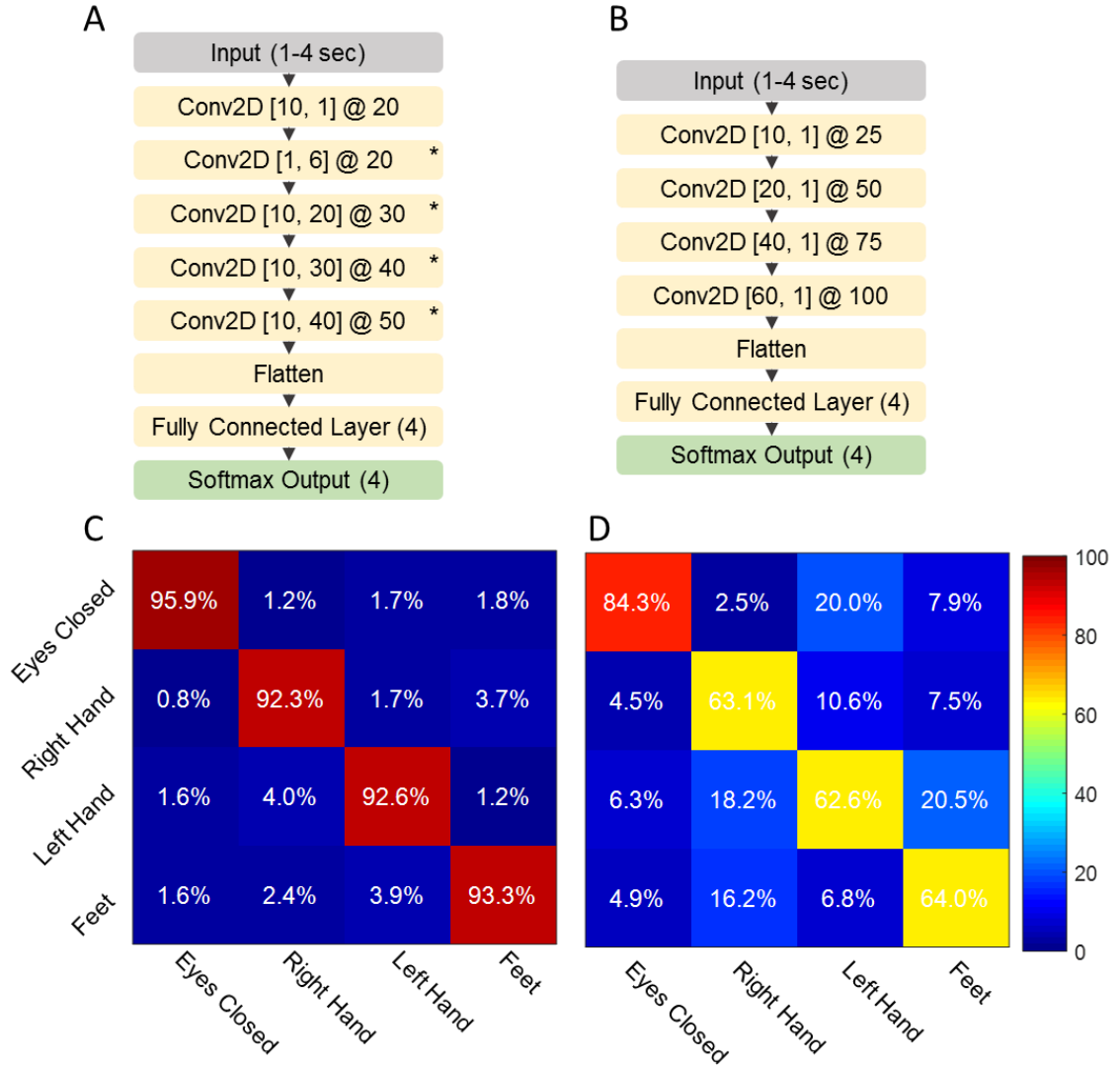


Figure 23. Comparison of CNN architectures and performance. (A) CNN architecture featuring multiple spatial convolution operations (Spatial-CNN), indicated with a ‘*’ symbol. (B) Standard CNN architecture with normal convolution operations along with the time-domain signals (Standard-CNN). (C) Confusion matrix demonstrating Spatial-CNN classifier performance on the FMNE dataset ($n = 2240$ samples from 4 subjects, 560 samples per subject, window length $w = 4$ s). (D) Confusion matrix demonstrating Standard-CNN classifier performance on the FMNE dataset ($n = 2240$ samples from 4 subjects, 560 samples per subject, window length $w = 4$ s).

Regarding feature extraction, PSDA demonstrates event-related desynchronization (ERD) and event-related synchronization (ERS) across MI classes when assessing six-channel data (Figure 24). However, not all ERS/ERD events are

apparent in this data, suggesting more subtle features obscured within the time-domain data. Additional results in Table 2 show that PSDA performs very poorly when compared with filtered time-domain data classified via CNN.

Table 2. PSDA and Cubic SVM Classification Results, Ag/AgCl with Conductive Paste Electrodes, 4-second time windows.

Subject	Fold 1	Fold 2	Fold 3	Fold 4	Fold 5	Average	Standard Error
1	66.67%	73.72%	61.54%	70.51%	68.59%	68.21%	1.82%
2	83.97%	81.41%	85.90%	83.33%	73.08%	81.54%	2.00%
3	81.41%	83.20%	89.74%	80.13%	82.69%	83.43%	1.49%
4	80.40%	79.60%	72.44%	75.00%	64.74%	74.44%	2.53%
Mean						76.90%	1.96%

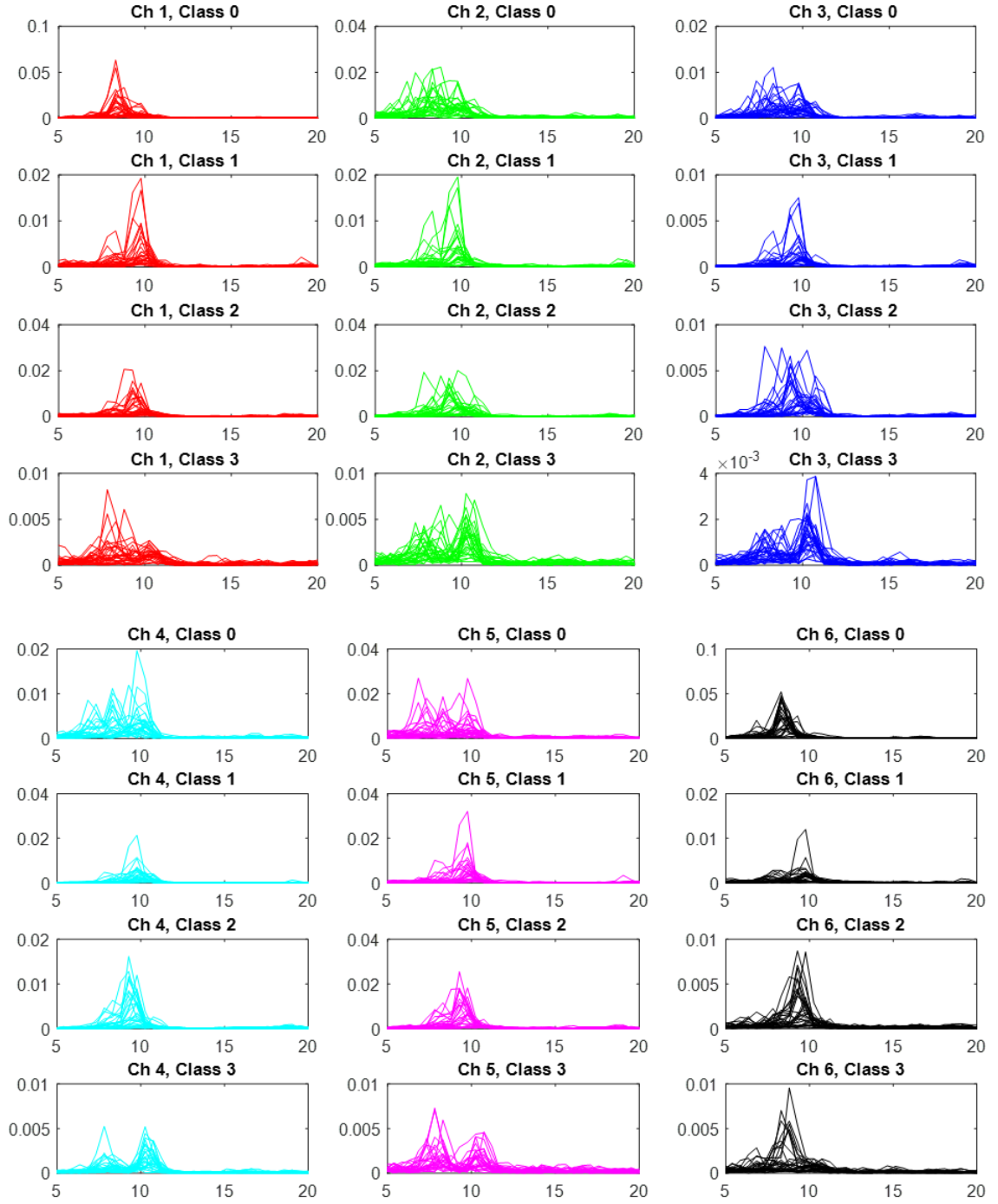


Figure 24. PSDA feature comparison of four EEG classes, demonstrating the presence of ERS/ERD in the form of power spectrum shifts for many of the samples shown (n=112 samples).

3.4.1 Feature extraction and classification

Data analysis involved power spectral density estimation using the Welch method [62], as described in prior work [58]. Here, the data is down sampled to 250 Hz, then preprocessed using a 3rd-order Butterworth bandpass filter from 4 Hz to 33 Hz and segmented into four-second windows with a 50% overlap between consecutive windows. Power spectral density estimation is then performed using 512-point overlapping Hann windows. This PSDA data is then trained using a SVM with a Cubic polynomial kernel function. For all CNN-based classifiers, the data is simply preprocessed using a 3rd-order Butterworth bandpass filter from 4 Hz to 33 Hz and segmented into four-second windows with a 50% overlap between consecutive windows.

3.4.2 Cross-validation of classification algorithms

A five-fold cross-validation scheme was used in all classification models, with four recordings being used for training and the fifth used for validation, across all five recordings. For the CNN, the batch size used was 64, and the training was run for 200 epochs or aborted early if the classification of the validation data did not improve for 20 epochs.

3.5 Results of MI-based BMI

Figure 26 shows a summarized set of preprocessing and classification of MI data with CNNs. An illustration in Figure 26A shows a spatial CNN model's detail with hidden layers of brain signals acquired from six EEG channels. This model demonstrates the capability of decomposing spatial features from multiple dipolar sources of the motor cortex. The comparison data in Figure 26B shows the different accuracies between three basic preprocessing methods and one with PSDA. Details on the PSDA preprocessing is

provided in *Materials and Methods*. In this comparison, the spatial-CNN with filtering shows better accuracy than PSDA. The results in Figure 25 compare the classification results with PSDA and SVM with a cubic kernel function on conventional Ag/AgCl electrodes and FMNEs, showing a better accuracy from the FMNE dataset (4-second windows).

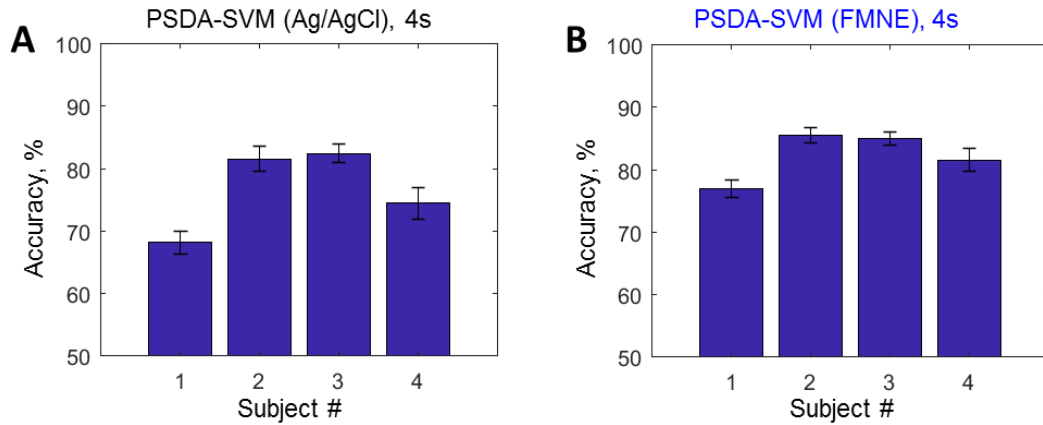


Figure 25. Comparison of classification results with PSDA and SVM with a cubic kernel function on conventional Ag/AgCl electrodes and FMNEs, showing a better accuracy from the FMNE dataset (4-second windows).

The graph in Figure 26C compares the spatial-CNN method's classification accuracy between the conventional Ag/AgCl electrodes and the newly developed FMNEs across multiple window lengths (1, 2, and 4 s). Error bars show a standard error from four subjects. All data sets that compare the performance between Ag/AgCl electrodes and FMNEs appear in Figure 27. Two confusion matrices in Figure 26D-E compare the performance of Ag/AgCl electrodes and FMNEs in classification accuracies with four classes. The real-time accuracy test of motor image brain data shows an overall accuracy of 89.65% and 93.22% for Ag/AgCl and FMNEs, respectively (2,240 samples, window length = 4 seconds, and 4 human subjects). Overall, the outstanding performance of EEG-

based MI classification with the soft scalp electronics (*Skintronics*) exceeds the results from prior works (Table 3).

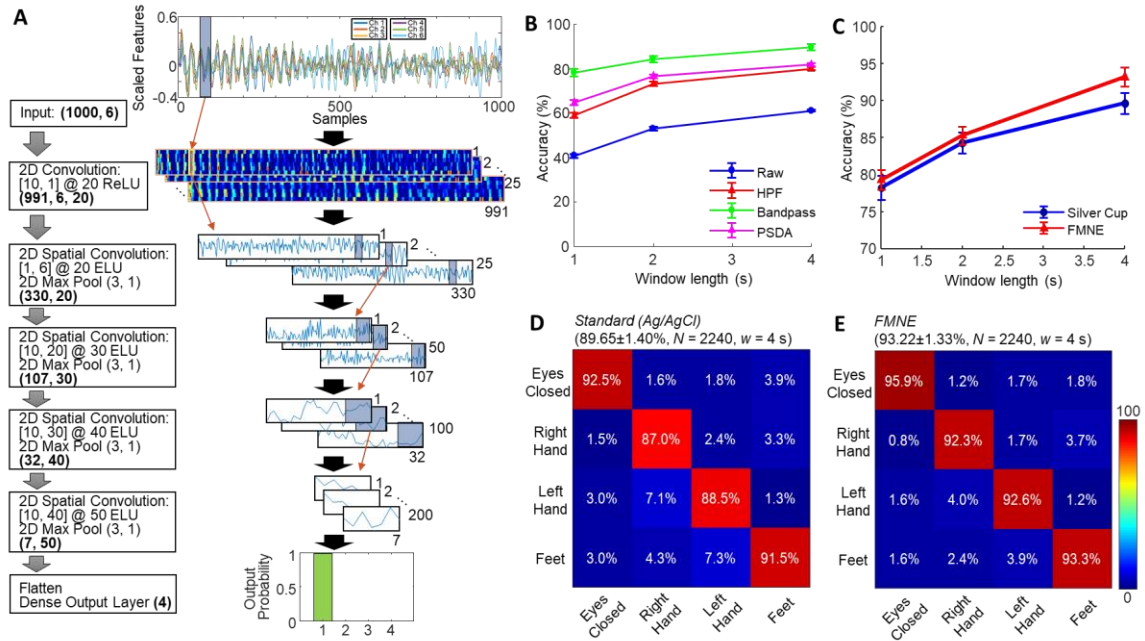


Figure 26. Preprocessing and classification of motor imagery brain signals with CNNs. A) Detailed illustration of a spatial CNN model with hidden layers of brain signals acquired from six EEG channels. This model demonstrates the capability of decomposing spatial features from multiple dipolar sources of the motor cortex. B) Comparison of spatial-CNN classification accuracy of four cases, including raw data, high-pass filtered data (HPF), band-pass filtered data (Bandpass), and power spectral density analysis (PSDA) across multiple window lengths (1, 2, and 4 s). Error bars show a standard error from four subjects. C) Comparison of spatial-CNN classification accuracy between the conventional Ag/AgCl gel electrodes and the newly developed FMNE across multiple window lengths (1, 2, and 4 s). Error bars show a standard error from four subjects. D) A confusion matrix representing results from the real-time accuracy test of motor image brain data, acquired by conventional Ag/AgCl electrodes, with an overall accuracy of 89.65% ($N = 2,240$ samples, window length = 4 seconds, and 4 human subjects). E) A confusion matrix representing results from the real-time accuracy test of motor image brain data, acquired by FMNE, with an overall accuracy of 93.22% ($N = 2,240$ samples, window length = 4 seconds, and 4 human subjects).

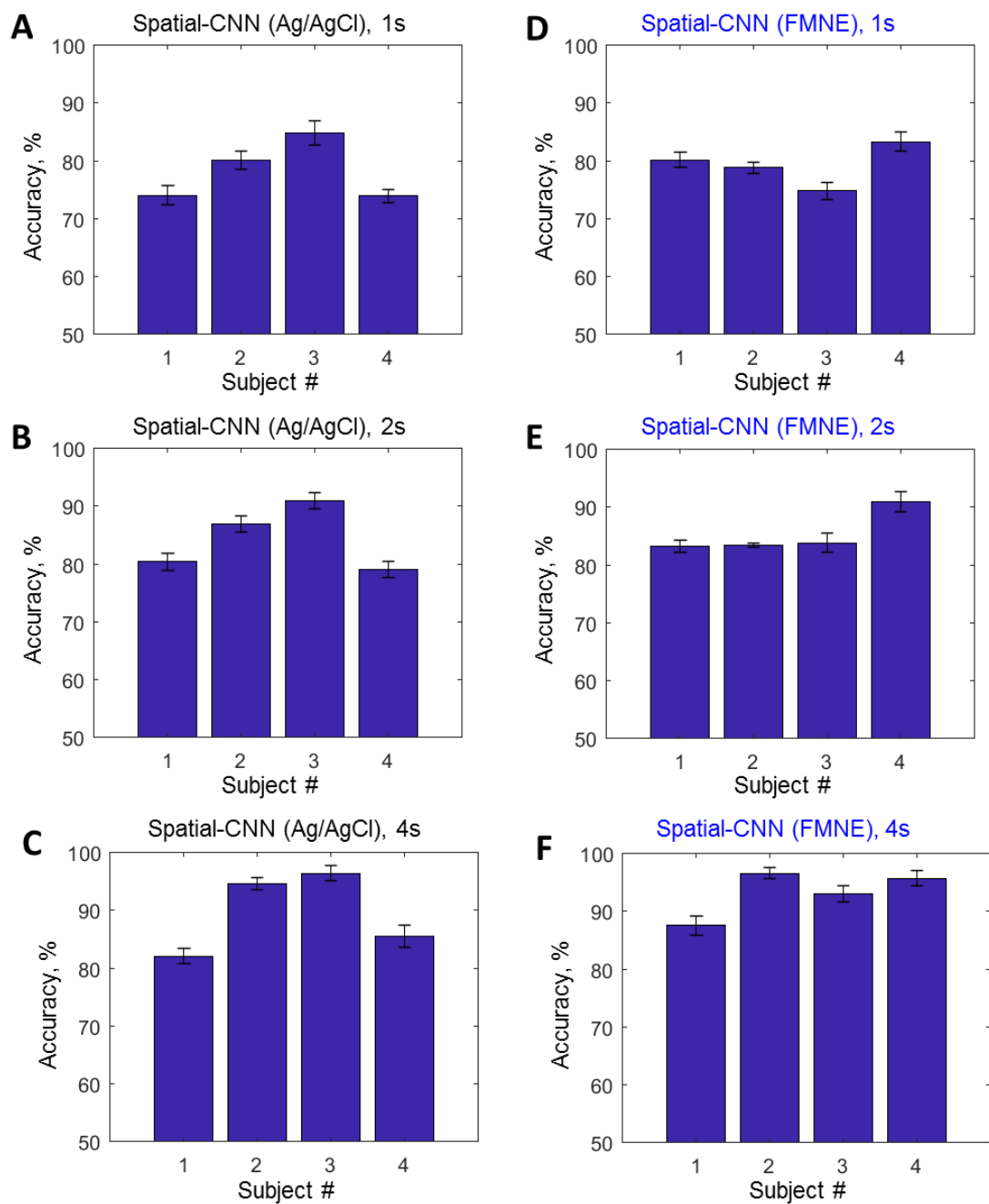


Figure 27. Comparison of the performance between Ag/AgCl electrodes and FMNEs across multiple window lengths (1, 2, and 4 seconds).

3.5.1 *Demonstration of real-time control of VR video game*

Cross-platform software development engine *Unity* (version 2018.4) was used to create the VR application for use with the Samsung Gear VR (Connected to a Samsung S7 mobile phone device). The 3D models of the hands and feet were created and animated with Maya version 2018. The VR application utilizes Bluetooth technology to exchange data with the controller application on the tablet pc. When the controller application detects an action such as "right-hand movement" or "eyes closed" from the user EEG signal, the application will send a byte array corresponding to that action through the connected Bluetooth channel to the VR application to inform them of the player action. In the VR game, cubes with 4 different colors (Blue, Green, Red, Yellow) will be generated, each corresponding to an action (feet movement, left-hand movement, right-hand movement, eyes closed) that is required from the users. The game lasts a total of 240 seconds. After the initial 1 second, the game will spawn a new cube every 4 seconds. The users need to provide the correct action through the EEG sensors in response to the color of the cube. For example, for a green cube, the user needs to move their left hand. When they perform a correct action, a green "correct" text will be displayed, and the cube will disappear, and the user will receive 1 point. For a wrong action, a red-colored "Wrong" text will be shown as feedback.

The combination of the high-performance electronics and the CNN-based machine learning allows for seamless integration of the system with a VR interface. The experimental study in Figure 29 shows the result of a VR implementation for MI training and real-time control of a video game. An overview of a study setup in Figure 29A captures a subject wearing the *Skintronics* system, real-time EEG data measured from six

electrodes (top inset), and an example of a VR interface (middle inset). A customized Android application provides real-time, continuous monitoring of 6-channel MI signals (screenshot shown in Figure 28). Examples of the training and testing processes of a VR game are shown in Figure 29B-D; a modified view of VR visuals is given to a subject with text and animation prompts. A video game interface, designed for MI response testing, shows clear color-coded visual cues as well as a text prompt. The summarized set of graphs in Figure 29E shows an accuracy comparison between non-VR setup and VR setup (two types of electrodes) classified with the spatial-CNN model.

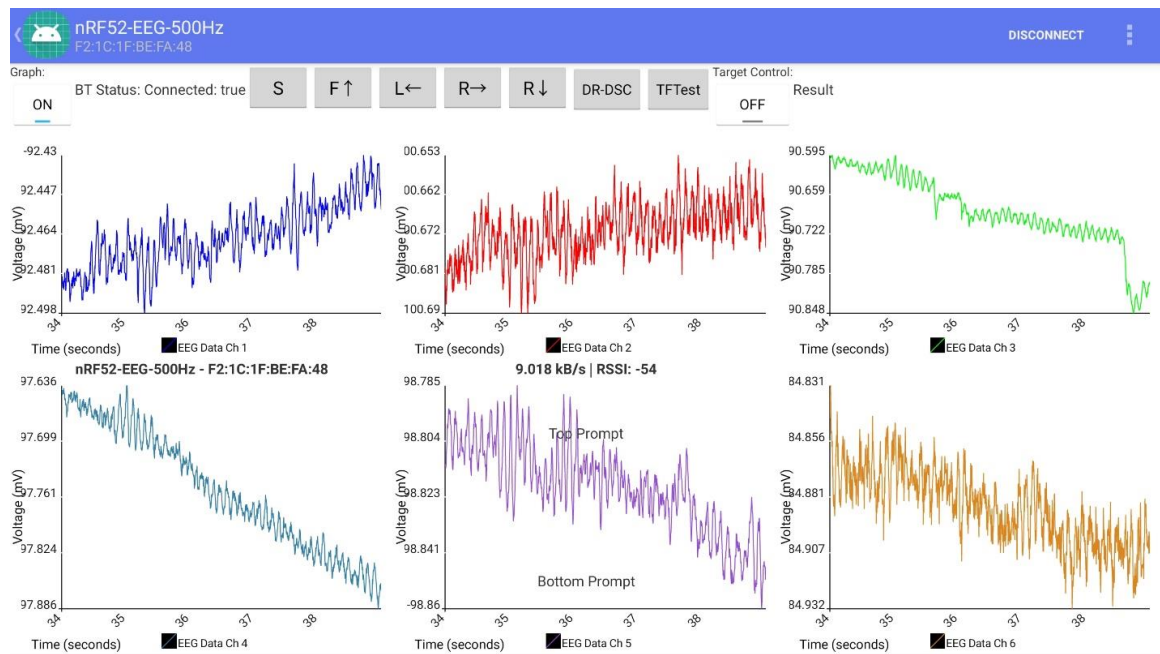


Figure 28. Android interface demonstrating real-time data plotting.

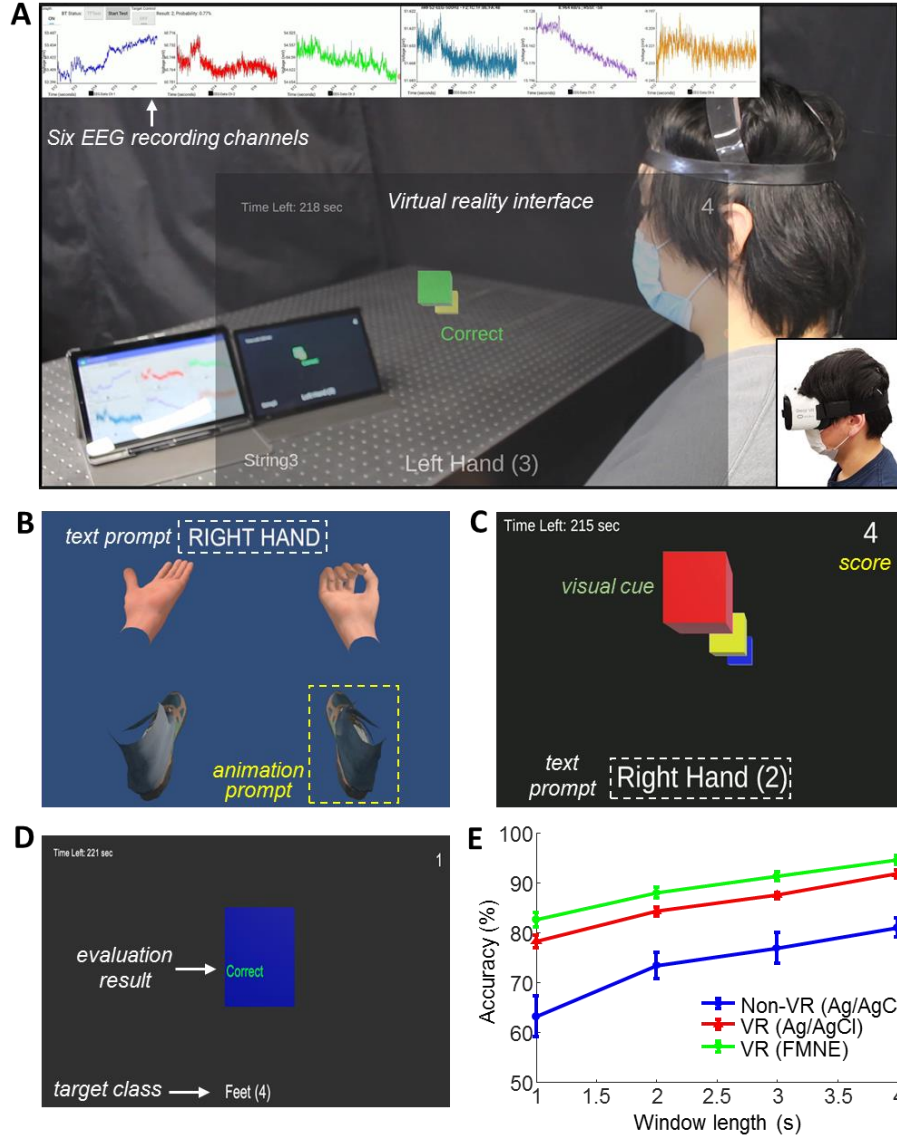


Figure 29. Virtual reality (VR) implementation for motor imagery training and real-time control of a video game demonstration. A) An overview of a study setup, including a subject wearing the *Skintronics*, real-time EEG data measured from six electrodes (top inset), an example of a VR interface (middle inset), and a photo of a subject wearing a VR headset (bottom-right inset). (B-D) Examples of the training and testing processes of a VR game. B) A modified view of VR visuals provided to test a subject with text and animation prompts. C) A video game interface designed for MI response testing with clear color-coded visual cues as well as a text prompt. D) An example of evaluation output according to the target class. E) An accuracy comparison between non-VR setup and VR setup (two types of electrodes) classified with Spatial-CNN model, demonstrating superior performance of VR as a training implement ($n = 2240$ samples from 4 subjects, 560 samples per subject, window length $w = 4$ s).

The result demonstrates superior performance of VR as a training implement (2240 samples from 4 subjects, 560 samples per subject, window length $w = 4$ s). At the same time, additional accuracy improvement is observed with the FMNE and VR setup. The enhanced accuracy would come from an immersive VR program with disembodied hands and feet shown within the subject's field of view in approximately the same position as their existing limbs. During the study, a subject could gently rotate or tilt their head to glance at the hands or feet as their focus requires.

3.6 Conclusion

The presented research in this chapter demonstrates a highly accurate classification of a four-class, MI-based BMI with as few as six channels. The *Skintronics* system provides a competitive accuracy and information transfer rate (ITR) with low response times ($93.22 \pm 1.33\%$ for 4 seconds of data; $ITR = 23.02 \pm 1.11$ bit/min). This study also shows a subject playing a rhythm-type video game where they must perform MI tasks in a specific prompted order within specific timing intervals to score points. Using 4-second windows, subjects could achieve high scores, only missing a few points per 5-minute game session. Subjects indicated that controlling the interface required a minimal effort on MI visualization.

The excellent signal reproduction with minimal artifacts may be attributed to the monolithic and compliant nature of the *Skintronics*. In conventional systems with rigid electronics and inflexible wiring, motion causes stress concentration at the skin-electrode interface. These stresses, when combined with conventional gel-based electrodes, cause significant skin-electrode impedance variations, resulting in motion artifacts. Where

dangling wires are involved, the influence of gravity compounds these issues. The newly developed FMNEs in the *Skintronics* provide an improved SNR by penetrating through the most superficial skin layers composed of dry and dead skin cells. By penetrating these layers and placing the conductive portion of the electrodes well within the dermis, we could significantly reduce the impedance density while allowing for smaller electrodes than the conventional setting and improving spatial resolution for MI detection. When compared head-to-head against the gold-standard Ag/AgCl gel electrodes, the FMNE achieved superior SNR. At the start of data acquisition, Ag/AgCl electrodes with abrasive gel to remove the superficial dead skin layer were favored. However, with the gel degrading over time, and as the impedance density and classification results show, the FMNE outperformed the conventional electrodes in every respect.

Additionally, an optimized training configuration in the form of an immersive VR environment resulted in a vast improvement in the system performance. The VR environment appears to have allowed subjects to visualize MI tasks better and easily focus on the training process. As a result, VR data is of higher quality, achieving superior classification performances as shown in Table 3. Without the visual cues from the VR headset, typically, MI signals could only be sustained for a few seconds at a time purely from imagination. With the VR headset, it allows the experimenters to record continuous, high-quality MI activity from one class for a minute at a time and could continue for an indefinite amount of time. Overall, the VR-based data yielded much higher quality data, resulting in optimal classification outcomes. Even after removing the headset, subjects could maintain excellent accuracy in test demonstrations, as shown in the video game demonstration.

Table 3. Performance comparison between the *Skintronics* and reported values for EEG-based MI classification.

Reference	Year	Accuracy (%)	# of electrodes	# of classes	Length (s)	# of subjects	ITR (bits/min)
<i>This work</i>	2020	93.22 ± 1.33	6	4	4	4	23.02 ± 1.11
[63]	2019	83.0	22	4	4	9	16.09*
[60]	2017	86.41 ± 0.77	28	2	3	2	$8.53 \pm 0.42^*$
[64]	2016	77.6 ± 2.1	3	2	2	9	$6.98 \pm 1.18^*$
[65]	2016	84.0	3	2	2	9	10.97*
[66]	2019	95.4	128	4	2	9	49.74*
[16]	2017	84.0	44	4	4	9	16.68*

As presented in this work, MI detection is advantageous in BMI paradigms since MI signals can be spontaneously produced by individuals, unlike with evoked potentials. Therefore, MI offers more significant potential as a general-purpose interface. However, a fundamental limitation is reconstructing poor-quality signals from the scalp to interpret motor cortex activity. In the next chapter, a more viable paradigm, steady-state visually evoked potentials (SSVEP) are studied towards increasing practicability and information throughput. Further drawbacks from this research include the arduous fabrication process of the PI-based microneedle electrodes, and the tangle-prone interconnect design. Both issues are considered and studied in the following chapter.

SSVEP-BASED BMI FOR WHEELCHAIR CONTROL

4.1 Background and overview

SSVEP signals require the use of steady-state flickering stimuli to elicit responses in the BMI user. These signals are then captured and classified to control the interface. However, inherent variation amongst human brains causes difficulty in implementation of electroencephalography (EEG) into a universal brain-machine interface (BMI). Existing SSVEP systems suffer from inconsistent signal quality, burdensome preparation time with many electrodes, and discomfort caused by rigid wires and metal electrodes in a hair cap. Additionally, leading classification methods require training on a per-subject or per-session basis. Although recent machine learning techniques offer a simpler EEG arrangement with fewer electrodes, these EEG devices still involve intrusive and heavy headgear, equipped with separate non-portable electrical hardware. The objective of this chapter is to demonstrate the potential for implementation of Skintronics as well as reduction to as few as 2 to 4 measurement electrodes while maintaining highly accurate classification. The first experiment will demonstrate a simple, 5-target setup for controlling an electric wheelchair to navigate an indoor environment. The second experiment increases the number of targets to 33 for controlling a text speller in a virtual reality environment.

Here, we introduce the first example of a fully portable, flexible, skin-like hybrid scalp electronics (referred to as ‘SKINTRONICS’) that includes a low-profile, flexible circuit, an ultrathin aerosol-jet printed skin electrode, and three flexible conductive polymer electrodes for mounting on the hairy scalp (occipital lobe). The primary novelty

is the miniaturized fully integrated packaging of all the required electronics within a low-profile skin-conformal wearable device. This low profile isolates it from most motion or cable related artifacts found with other EEG systems, allowing for superior SNR over long recordings. The number of electrodes was limited to reduce the profile of the electronics, and to allow for ease of setup. The SKINTRONICS is capable of competitive information transfer rates with as few as two data channels. We demonstrate a new capability to train deep convolutional neural networks (CNN) offline and integrate them into wireless mobile devices for a real-time, universal EEG classification. Additionally, optimization of the system setup and classification model enables a highly competitive information transfer rate[67] ($122.1 \pm 3.53 \text{ bits min}^{-1} \text{ channel}^{-1}$) using only two channels, far fewer than most other systems achieving similar values. With ever-improving mobile processing power, the combination of many-channel SKINTRONICS with integrated universal BMI, demonstrates possible implications for the use in portable EEG-based neuroprosthetics, real-time diagnosis of neurological disorders, or neuro-assisted learning (classroom support).

4.2 Development of 5-target SSVEP-based motor wheelchair interface

Figure 30 shows an overview of the wireless, portable scalp electronics for SSVEP-based BMI. The fully flexible, wearable system enables real-time long-range wireless data acquisition and accurate classification of SSVEP with a high information transfer rate from only two recording channels. The extreme mechanical compliance and small form factor of the wearable SKINTRONICS with a low-power circuit on scalp allows significant reduction of noise and electromagnetic interference, compared to the existing portable EEG systems with rigid electronic components[22, 68-70].

Additionally, the use of conformal electronic components allows for easy wearability on the back of the neck, or on other skin locations. This emphasis on ergonomics makes it preferable for long-term wear versus rigid PCBs or other devices with heavy plastic enclosures that have to be clipped-on or worn in other uncomfortable manner. The photo in Figure 30A captures the design concept of the scalp electronics that minimize the contact area (only 2 channels) on the scalp for a comfortable, dry EEG recording. The electrodes are connected to the SKINTRONICS through flexible thin film cables, which are routed under the headband and connected on the right side of the device. Shorter secured interconnects result in reduction of noise introduced through cable movement. We utilize a set of dry, flexible elastomeric electrodes (Cognionics) that make intimate contact to the hairy region, resulting in long-term EEG recording[71]. In addition, a skin-conformal, aerosol-jet printed electrode with improved skin adhesion reduces motion artifacts and enhances skin-electrode contact impedance. This electrode acts as a driven bias, therefore its ability to capture EEG is out of the scope of this paper and not tested. Overall, the integrated electronics on the scalp, in conjunction with a deep-learning algorithm, demonstrates the feasibility of this device for real-time, highly accurate *in vivo* BMI via SSVEP data from two channels.

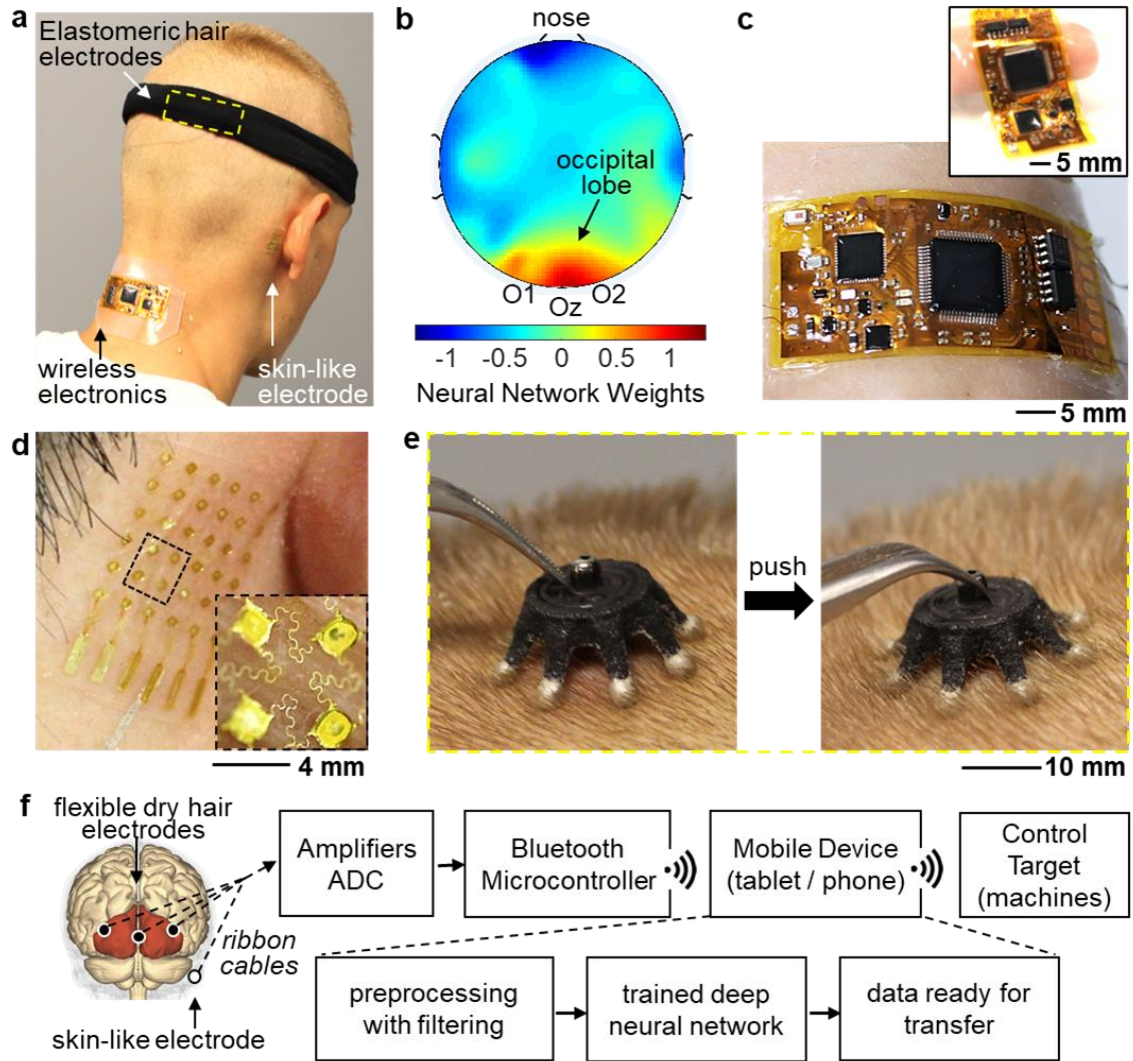


Figure 30. Overview of the system architecture featuring fully portable, wireless scalp electronics. (A) Photo of a subject who has flexible wireless electronics (SKINTRONICS) conformed to the back of the neck with dry hair electrodes under a fabric headband and a membrane electrode on the mastoid, connected via thin film cables. (B) Neural network-based topographical map that indicates EEG signal amplitudes. (C) Photo capturing the ultrathin, flexible wireless electronics on skin, with an inset demonstrating device flexibility while handling. (D) Aerosol-jet printed stretchable, skin-like electrode with an open-mesh structure (inset). (E) Images showing gentle splaying of the conductive flexible elastomer legs of a dry hair electrode when slight downward pressure is applied, allowing the legs to separate the hair and the Ag/AgCl tipped legs to achieve good contact with the scalp. (F) Illustration (left) showing electrode positions on a posterior view of the brain and highlighted occipital lobe and flow chart (right) describing the entire process of EEG-enabled brain-machine interfaces.

The optimal electrode locations may be determined by a deep CNN analysis of 32-channel EEG data from a conventional signal mapping (Figure 30B and details in Figure 30A-C). This process is not required for this SSVEP interface but is used to validate the selected scalp locations used for the two-channel setup. The electrode positions represented in Figure 30B (O1, Oz, O2) were determined empirically in preliminary tests to have consistently high SNR across all tested subjects. The system is designed to be universal for all subjects; and should not require retraining between subjects or sessions. The methods used here to isolate the best electrodes from a larger cluster of electrodes is a noteworthy, as it does not require prior knowledge of the signal type. This is most useful when trying to reduce the number of channels in a system, but the signal's features are not obvious or are difficult to decompose by conventional methods.

The representative sample of a topographical scalp captures the largest signal weights on the O1, O2, and Oz channels (data of other EEG mapping from six human subjects appear in Figure 31). These results are consistent with other topographical maps in a prior work[72]. For a deep neural network analysis, data was sampled at 256 Hz and the reference was set at Oz for the best results. The optimal electrode location was determined by a CNN trained to classify from all 32-channels (architecture listed in Table 4). The trained weights for each channel could then be extracted and plotted using a topographical mapping algorithm provided by open EEGLAB (open source software)[73]. Details of this method are explained in Appendix under

Topographic Scalp Mapping using Deep Learning. This multi-channel quantitative EEG study retrospectively verifies the optimal two electrode locations that were used in the two-channel EEG study.

Table 4. 2-CNN-Mapping: Convolutional Neural Network Model for Weight Extraction from 32-channel SSVEP Datasets. Using time domain data, we are able to optimize classification of real-time EEG data. Although the average accuracy was low across six subjects, we can generate mappings consistent with published literature regarding SSVEP.

Layer Name	Layer Description
Input	Time Domain Input: [32 x length(w)]
Conv1	[1 x 8] conv, 32 ReLU Units, Stride [1 x 1]
Pool1	[1 x 2] Max Pooling, Stride [1 x 2]
Conv2	[1 x 4] conv, 64 ReLU Units, Stride [1 x 1]
Pool2	[1 x 2] Max Pooling, Stride [1 x 2]
FC	Fully Connected Layer, 1024 ReLU Units, 50% Dropout
Softmax	5-way softmax output

The miniaturized, multi-channel flexible electronic system (Figure 30C), encapsulated in a soft elastomeric membrane, was fabricated by using the combination of microfabrication techniques[74], material transfer printing[74], and hard-soft component integration[75]. This manufacturing process makes a skin-conformal, unobtrusive, and comfortable device to the wearer. Prior to the fabrication, the circuit design was validated on a printed board to confirm the optimized layout with matching antenna circuitry (Figure 32A), along with the optimized components for a protocol of 2.45 GHz Bluetooth low energy. The reflection coefficient (S_{11}), plotted in Figure 32B, has a local minimum at 2.449 GHz of -29.68 dB, which allows for excellent telemetry at reasonably large ranges.

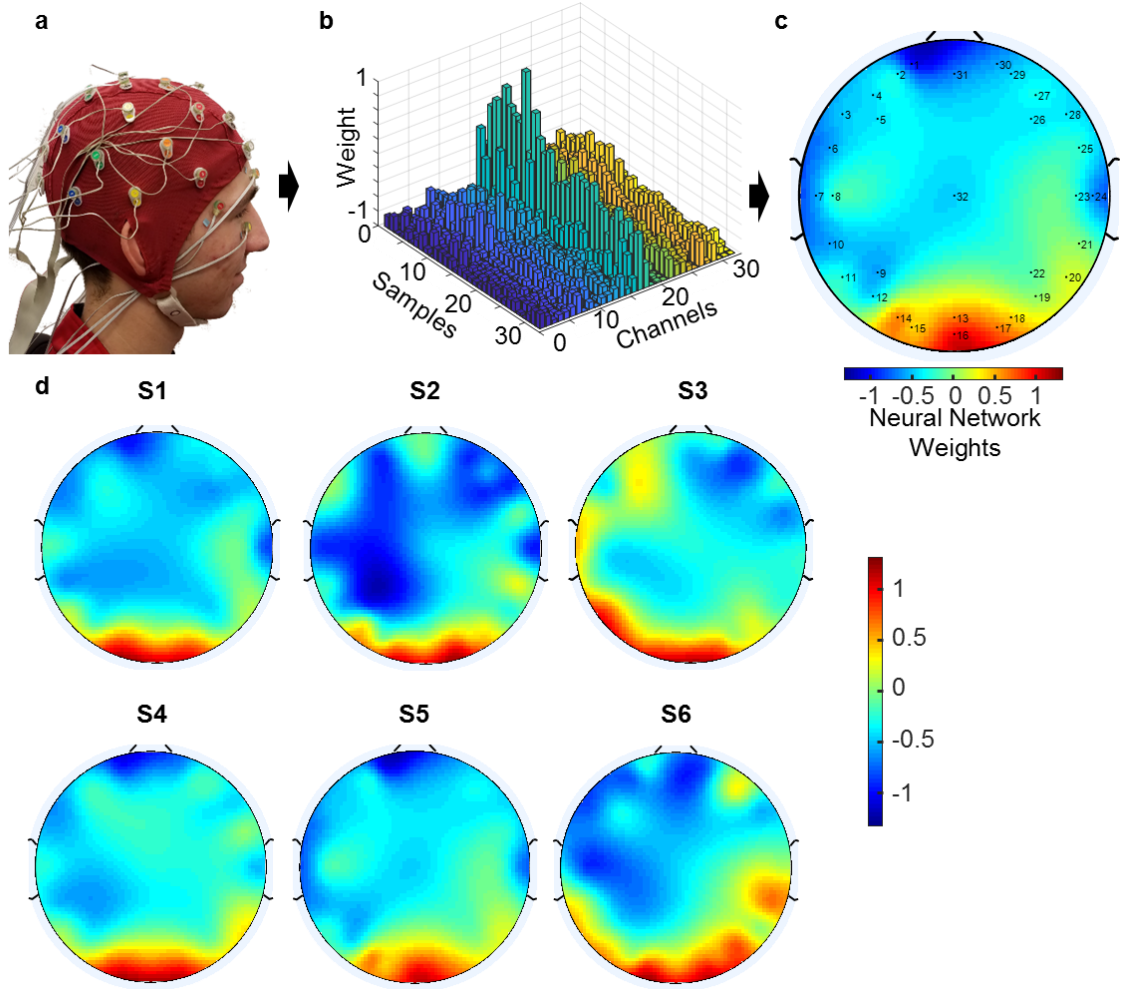


Figure 31. Topographical mapping of EEG signals using convolutional neural networks. (a) 32-channel cap EEG setup on test subject. (b) Weights extracted from the 2-CNN-Mapping convolutional neural network. From 32 convolutional filters used across all channels, the average weights for each point are summed, resulting in the weight mappings for each of the six subjects as illustrated in (c). The color scale represents the rescaled average neural network weights based on $n=200$ samples (40 samples per class). (d) shows the mappings generated for all 6 subjects, labeled correspondingly.

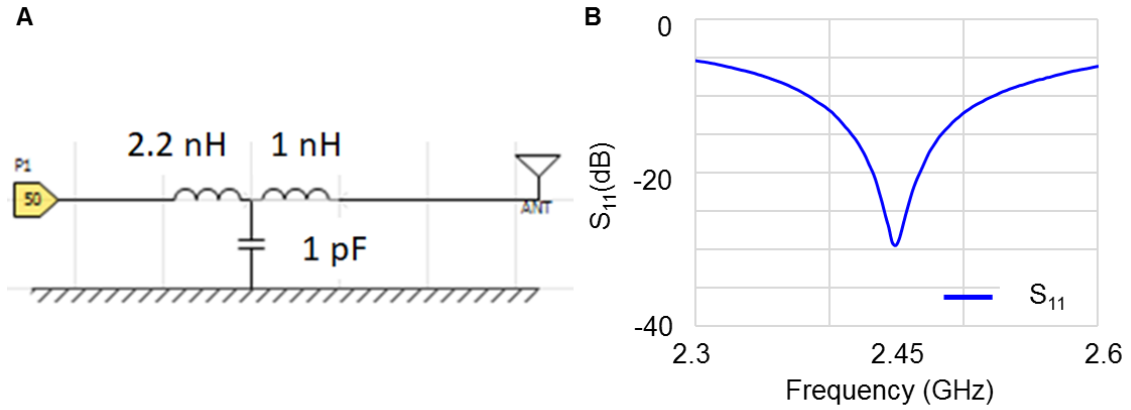


Figure 32. Antenna Matching Circuitry for SKINTRONICS wireless EEG. (A) shows the components in the antenna matching configuration optimized for use with the thin multilayer flexible SKINTRONICS format. (B) Shows reflection coefficient (S_{11}) measurement with a network analyzer in air, with the device placed flat on a glass slide.

The details of the device fabrication and encapsulation processes appear in the Appendix under

Device Fabrication Process (identical to the one presented in Chapter 3) and step-by-step illustration is shown in Figure 33. The EEG recording setup for two channels (O1 – Oz and O2 – Oz; Figure 30B) incorporates an aerosol jet-printed skin-like electrode and elastomeric hair electrodes. The highly conformal membrane electrode (Figure 30D) is placed at the right mastoid to serve as driven ground (details of the electrode fabrication in the Appendix under

Fabrication of Skin Electrodes via Aerosol Jet Printing).

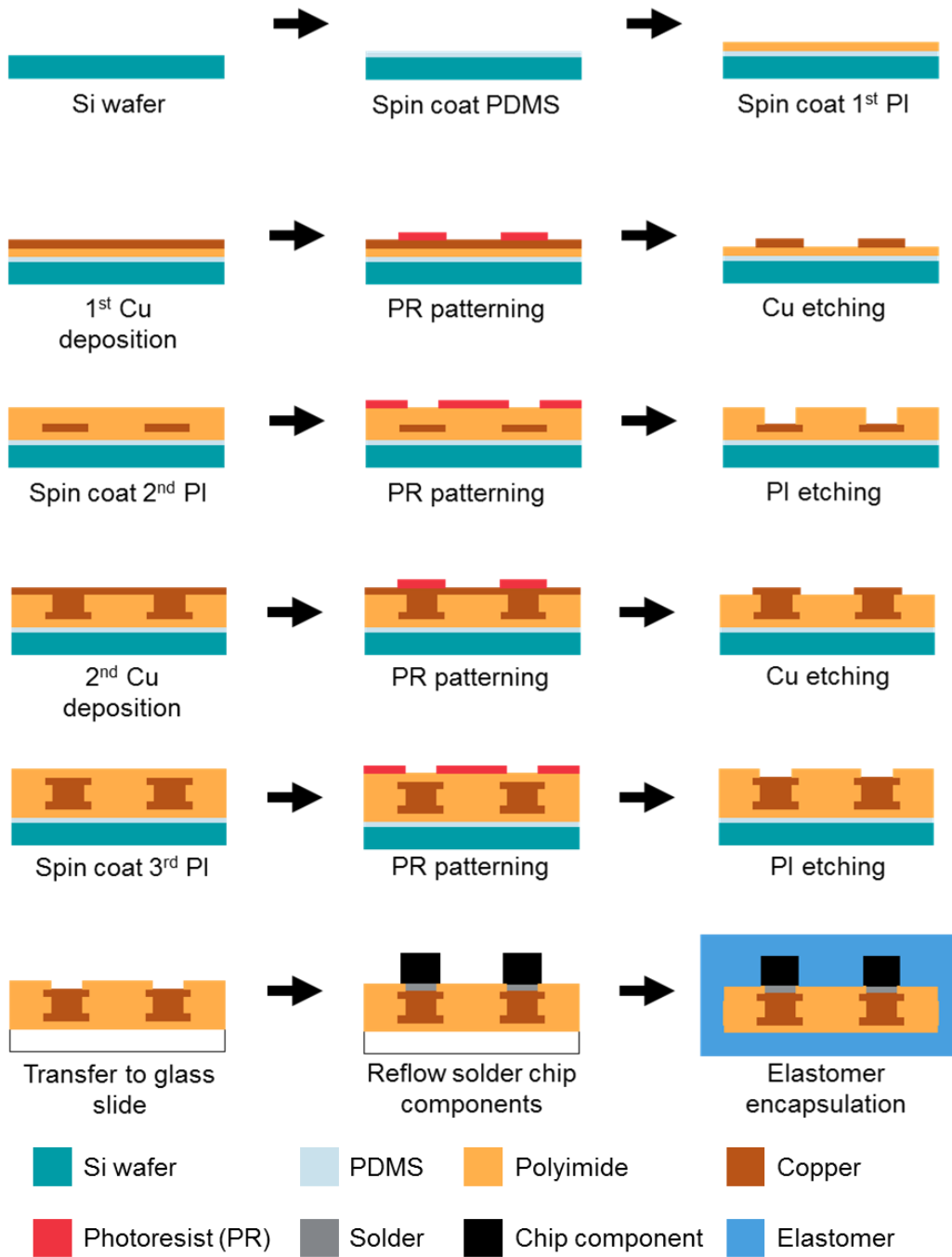


Figure 33. A schematic representation of the microfabrication and the assembly processes. Conventional microfabrication processes are used to construct the flexible circuit board. The PDMS-coated wafer surface allows the completed circuit boards to be peeled off and transferred onto a glass slide, where the reflow soldering of the chip

components is carried out. The soldered board is detached from the glass slide and fully encapsulated with elastomer.

With adequate skin preparation, conformal contact provided by these electrodes allow for superior skin impedance (less than 20 k Ω), and therefore lower noise in signal recording and transmission. In addition, there are only three scalp electrodes, effectively secured by using a single headband, which allows the electrode to splay its legs, separating and moving hair, to make effective contact with the scalp as demonstrated in Figure 30E. A flow chart in Figure 30F summarizes a high-level overview of data collection, processing, wireless transfer, and machine control. The wireless telemetry unit uses a Bluetooth low-energy microcontroller (nRF52832, Nordic Semiconductor) due to its high throughput, low latency, low power draw and wireless range[75]. The Bluetooth low-energy protocol supports wireless synchronization of multiple devices to support greater numbers of channels[76], with each SKINTRONICS device capable of supporting up to eight channels. This flexibility in the number of channels and devices that can be synchronized makes it optimal for biopotential paradigms where multiple signals need to be recorded simultaneously at different locations. For EEG recording, a front-end integrated circuit (ADS1299, Texas Instruments) was used, which is a low-noise 24-bit analog-to-digital converter with a built-in bias drive, which supports up to eight differential-input channels. The design also incorporates second-generation low-noise instrumentation amplifiers as the first gain stage (INA828, Texas Instruments).

4.2.1 Quantitative study of device mechanics and reliability

To build a portable, wearable scalp electronics, intimate skin integration is critical while allowing the wearer to conduct everyday activity. It must also maintain its ability to

acquire high fidelity EEG along with wireless transmission of data while under bending. In this work, we subject the electronics to 180° bending up to 1.3 mm in radius of curvature, well beyond the bending experienced during skin deformation on the back of the neck. Similar mechanical tests are performed on the hair electrode and skin-like electrode to ensure long-term mechanical stability on the skin application. Computational finite element analysis (FEA) was used to design the electronic circuit and wearable electrode, which provided an optimal design to endure continuous mechanical deformation. Afterwards, a set of experiments demonstrated the mechanical reliability of the SKINTRONICS (Figure 34), including microscope investigation, resistance measurement, and received signal strength indication (RSSI). The flexible electronic circuit shows a great mechanical stability upon cyclic bending along the vertical axis for the first location (Figure 34A-D) and second location (Figure 34E-H). Details of the bending points appear in Figure 34A. With a complete folding of the device at the bending radius of 1.3 mm (Figure 34A), the device shows no adverse effects, as supported by the FEA result (Figure 34B) with negligible change in the maximum principal strain ($<0.1\%$). The change of electrical resistance of the interconnects in Figure 34A is measured during the cyclic loading and unloading process (Figure 34C), which also shows consistent resistance with the maximum change of $0.06\ \Omega$.

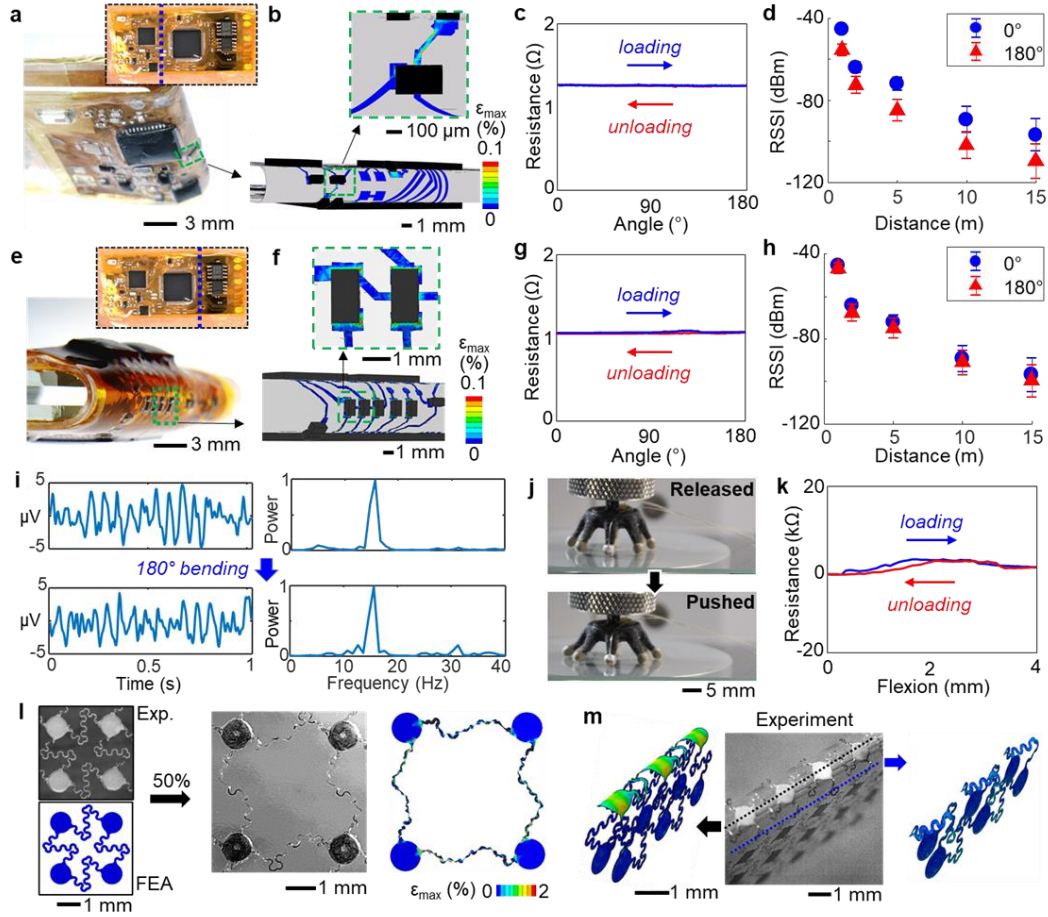


Figure 34. Mechanical flexibility and stretchability of the scalp electronics. (A) Photo of the electronics bent at first location along the vertical axis, as shown in the inset photo, between microcontroller and ADC integrated circuits, demonstrating 180° bending (radius of curvature: 1.3 mm). (B) FEA of fine mesh structure simulating 180° bending in (A) with same radius resulting in minimal strain at the interconnects (scale bar: maximum principal strain). (C) Measurement of electrical resistance for the device in (A) under cyclic bending between 0 and 180°, showing negligible changes in resistance. (D) RSSI response at 0° and 180° with different distances up to 15 meters ($n = 3$ samples). (E) Device bent at the second location along the vertical axis, as shown in the inset photo, between ADC and amplifiers (radius of curvature: 1.3 mm). (F) FEA of the flexible structure simulating 180° bending with minimal strain (scale bar: maximum principal strain). (G) Measurement of cyclic bending effect on the device in (E) by recording the change of electrical resistance. (H) RSSI response up to 15 meters at 0° and 180° bending. (I) 15.2 Hz SSVEP data recorded without (top) and with 180° bending (bottom). (J) Hair-based elastomer electrode under compression. (K) Corresponding load and unload curves showing a negligible peak change in resistance over a 6-second cycle. (L) Subunit of a skin-mounted electrode under 100% stretching in experiment and FEA, showing no mechanical failure. (M) 180° bending test of the electrode, showing less than 2% strain in FEA and no mechanical defects in experimental observation.

Additionally, the RSSI measurement monitors the wireless signal quality under 180° bending up to 15 meters (Figure 34D), showing that the device maintains connectivity at distances over 10 meters. Details of the mechanical bending configuration are shown in Figure 35. Another location of the electronics shows 180° bending with the radius of 1.6 mm (Figure 34E). The corresponding FEA in Figure 34F shows similar results to the first location, and the interconnects are intact after bending. Figure 34G shows the resistance measurements at this location where the maximum change in resistance is 0.09 Ω , indicating the stability of the interconnects during cyclic bending. The RSSI investigation (Figure 34H) validates the device's functionality with distances up to 15 meters. The resistance measurements at each location after 100 bending cycles are shown in Figure 35C, showing a slight increase in resistance, from 1.19 to 1.51 Ω at location 1, and from 1.08 to 1.38 Ω at location 2. Furthermore, recorded SSVEP data (stimulus at 15.2 Hz) compares the effect of cyclic bending of the electronics (Figure 34I), which shows negligible change in the signal quality. The elastomeric hair-based electrodes underwent cyclic compression testing while monitoring resistance from the connector to a single leg of the electrode.

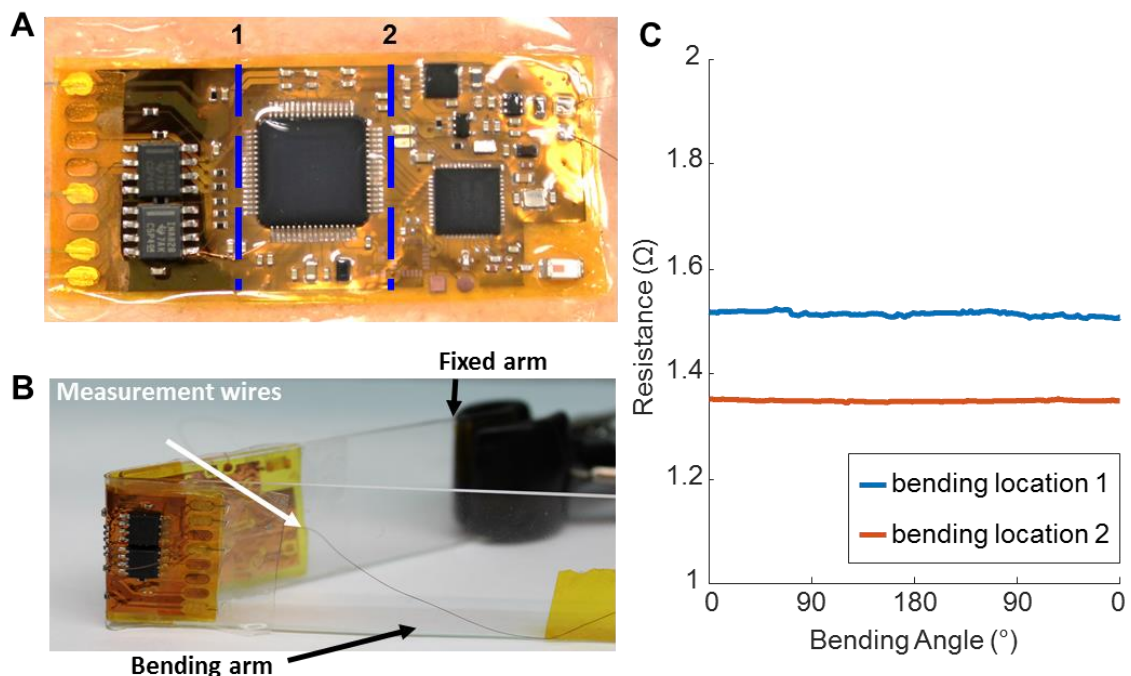


Figure 35. Mechanical Testing Setup and Additional Results. (A) Picture of device conformed to skin, with lines indicating the two locations of bending. (B) 180° bending test setup, with the device attached to glass slides, and attached wires for resistance measurements. (C) Resistance measurements on cyclic bending after 100 cycles completed at two bending locations, indicated by the legend.

The setup is shown in Figure 36, with the process described as follows: For cyclic compression of the hair electrode a motorized tension/compression test stand (ESM303, Mark-10, USA) was used to push the electrode with a controlled displacement of 2 mm. Two conductive film wires (HST-9805210, Elform, USA) were attached with silver paint (PELCO Conductive Silver Paint, Ted Pella, USA) to monitor the resistance across one of the flexible legs using a digital multimeter (DMM7510, Keithley Instruments, USA). Placed between two metal compression plates, the hair electrode underwent a repeated compression of 1000 cycles, with each cycle lasting approximately 6 seconds. Figure 36 shows the testing setup used for this experiment with multimeter and laptop for recording

results (Figure 36A), and the positioning of the electrode between the compression plates. (Figure 36B).



Figure 36. Compression Test Setup for Elastomeric Hair-based Electrodes. (A) Motorized tension/compression test stand setup with benchtop digital multimeter and laptop to measure resistance. (B) Placement of elastomeric hair-based electrodes between compression plates of test device.

The results from this test are shown in Figure 37, with the entire captured resistance data shown in Figure 37A, showing a general decrease in resistance over the test period. A single cycle in this process is expanded in Figure 37B, showing how the resistance increases under compression for the first three seconds, and returns to normal on decompression. A moving average is computed using a window of 90 samples (approximately 6 seconds) to show the reduction in resistance over 1000 cycles, showing a drop of $-4.46\text{k}\Omega$.

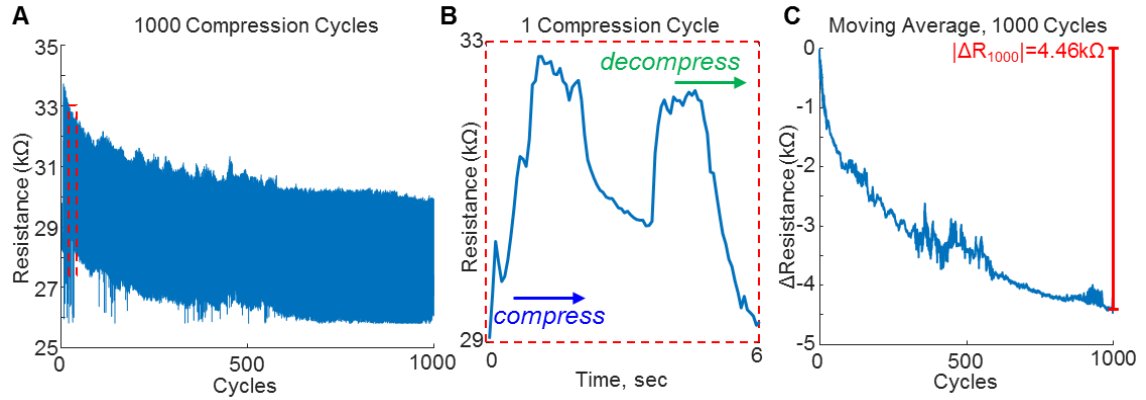


Figure 37. Data from Compression Test of Elastomeric Hair-based Electrodes. (a) Resistance data measured across single leg of the elastomeric hair-based electrodes, with (b) showing a representative resistance curve for a single compression cycle. (c) is a smoothed curve computed from a moving average of (a), using a 6-second (90 sample) moving average, showing the drift in resistance over extensive mechanical usage.

A maximum compression of 2 mm, followed by release over a 6-second period (Figure 34J), was repeated for 1000 cycles, simulating the maximum compression exhibited during EEG recording. During a single cycle of compression, the peak change in resistance was only 4.1 k Ω (Figure 34K). Even with 1,000 cycles, the uncompressed resistance changed a total of 4.46 k Ω (less than 10% of the initial resistance; Figure 37). The conductive elastomeric electrodes showed excellent resilience to mechanical stress and were still capable of measuring EEG after the test was completed. These results are supported by prior studies evaluating the robustness of these electrodes in high-density multichannel systems[77].

For EEG recording, a skin-like silver electrode undergoes multi-modal bending and stretching on the skin (mastoid), considering the ultrathin epidermis on that area with time-dynamics movements with the ear. For bending tests, a setup similar to the one used in Figure 35 for testing SKINTRONICS was used. For biaxial stretching, the device is placed in a custom-built biaxial stretcher (Figure 38), where opposite ends of a completed

electrode are silver pasted to copper wires that are connected to a digital multi-meter for resistance measurements.

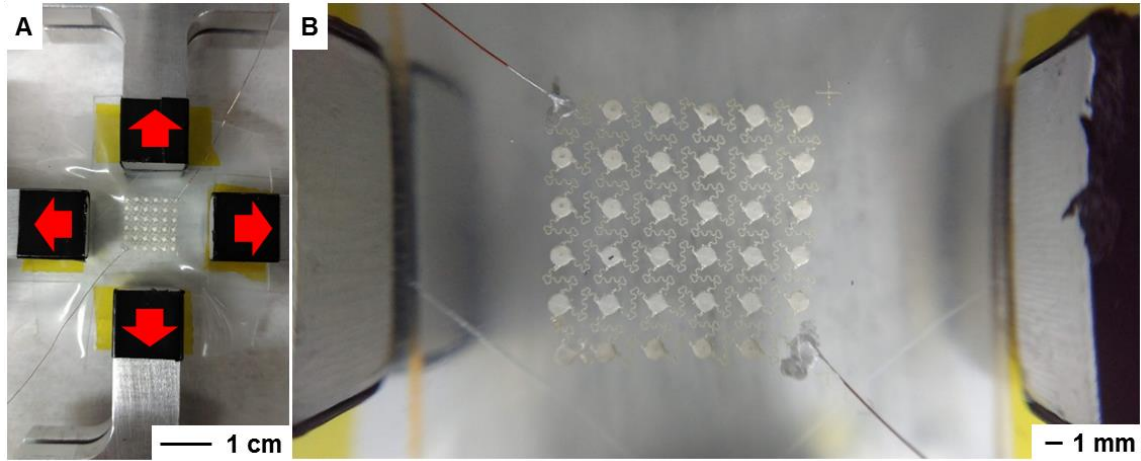


Figure 38. Biaxial Stretching Test Setup for Skin Electrodes. (a) Custom device for biaxial stretching with a flexible skin-based electrode on an elastomer placed between the 4 clamps. (b) shows a close-up of the device with attached copper wire (using silver paste) for resistance measurement.

Biaxial stretching caused the resistance to increase as expected as the interconnects thinned, followed by a fracture at over 60% strain (Figure 39). Resistance change during bending was also measured, showing stability under complete folding at a small radius. The summary of the experimental and computational study in Figure 34L-M validates the structural safety of the printed electrode, with over 50% biaxial strain and up to 180° bending at the radius of 250 μm . FEA results show the maximum strain under 1% in any region of the electrode, while microscopic observation captures no fracture lines. Overall, the computational and experimental study demonstrates the mechanical stability of the SKINTRONICS, including both electrodes and wireless circuit, suggesting that the device is resilient enough for normal use with human subjects.

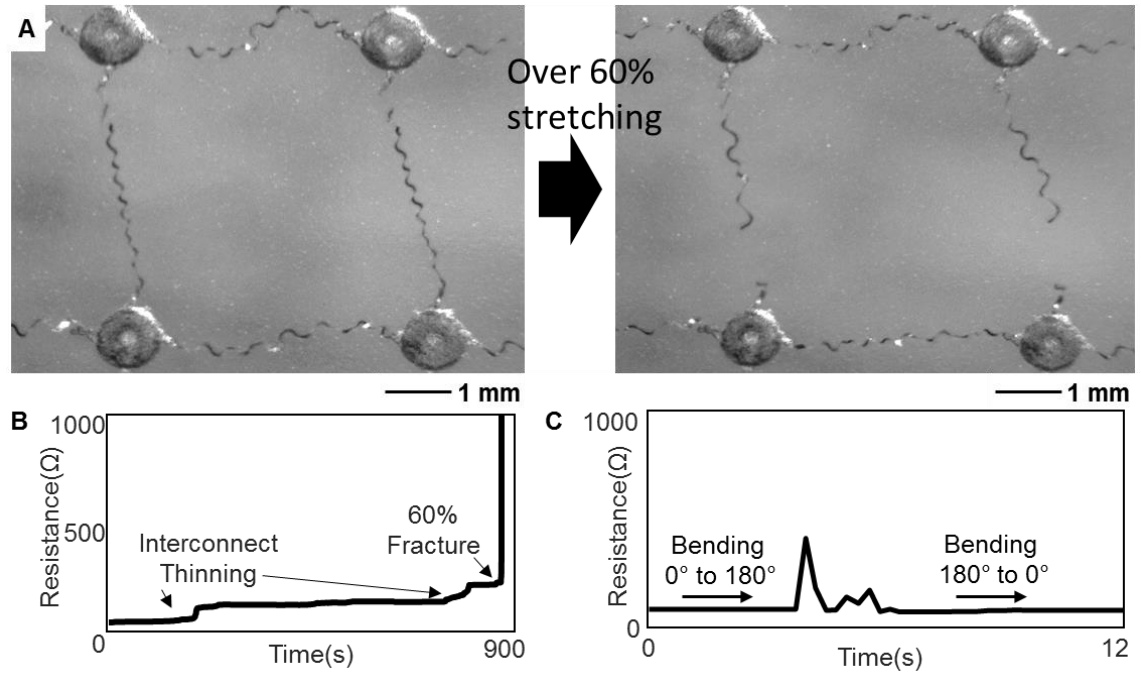


Figure 39. Data from Biaxial Stretching and Bending of Skin Electrodes. (a) electrode near 60% biaxial stretching before fracturing, as shown in (b). (c) experimental stretching shows deformation of the silver causing an increase in resistance. (d) Bending 180° increases the resistance due to the deformation of the skin-electrode but releasing that stress brings the resistance back down.

4.2.2 Analysis of device performance

We measure SSVEP at four frequencies (11.1, 12.5, 15.2, and 16.7 Hz), and alpha rhythms to test the robustness of a system to specifically decode SSVEP. We use alpha rhythms as the null class (no target interface action), intended for the user to relax their eyes in case of fatigue. Due to the overlapping frequency ranges between alpha rhythms (8 – 12 Hz) and intended SSVEP classes[78], the decoding process becomes more complex and error-prone to conventional machine learning techniques. Therefore, SSVEP frequencies below 11.1 Hz were not used due to frequency overlap with alpha rhythms. Here, the average accuracy is 86.44%, giving an ITR of 120.3 bits per minute. However, these frequencies were not included in the final system as they were considered

extraneous, and some subjects had trouble focusing on these higher frequency stimuli. It was studied that the risk of short bursts of alpha rhythms could cause false positive results in these ranges[79]. The converse case is also a concern, where intentional alpha rhythms (subject has eyes closed) are incorrectly interpreted as SSVEP within the alpha frequency band. Despite many prior works showing SSVEP-based systems within the alpha rhythm range, there has been limited study regarding confusion between SSVEP and alpha rhythm classification.

The new electronic system, SKINTRONICS, is benchmarked against two state-of-the-art EEG monitoring devices. The first is a 32-channel EEG system (ActiveTwo System, Biosemi B.V.), using water-based conductive gels (SignaGel, Parker Laboratories) and the second is a wireless, portable system (BioRadio, Great Lakes NeuroTechnologies) that allows for 8 channels in a referential montage. We demonstrate the functionality and performance of the SKINTRONICS via the direct comparison with those commercial systems. The ActiveTwo 32-channel system uses Ag/AgCl active electrodes to represent the gold standard, benchtop EEG system, while the BioRadio uses dry, flexible elastomeric electrodes (Cognionics) as a control to compare the performance of the SKINTRONICS. Figure 40 summarizes the comparison of SSVEP captured using a single occipital lobe channel (O1-Oz), by three different systems.

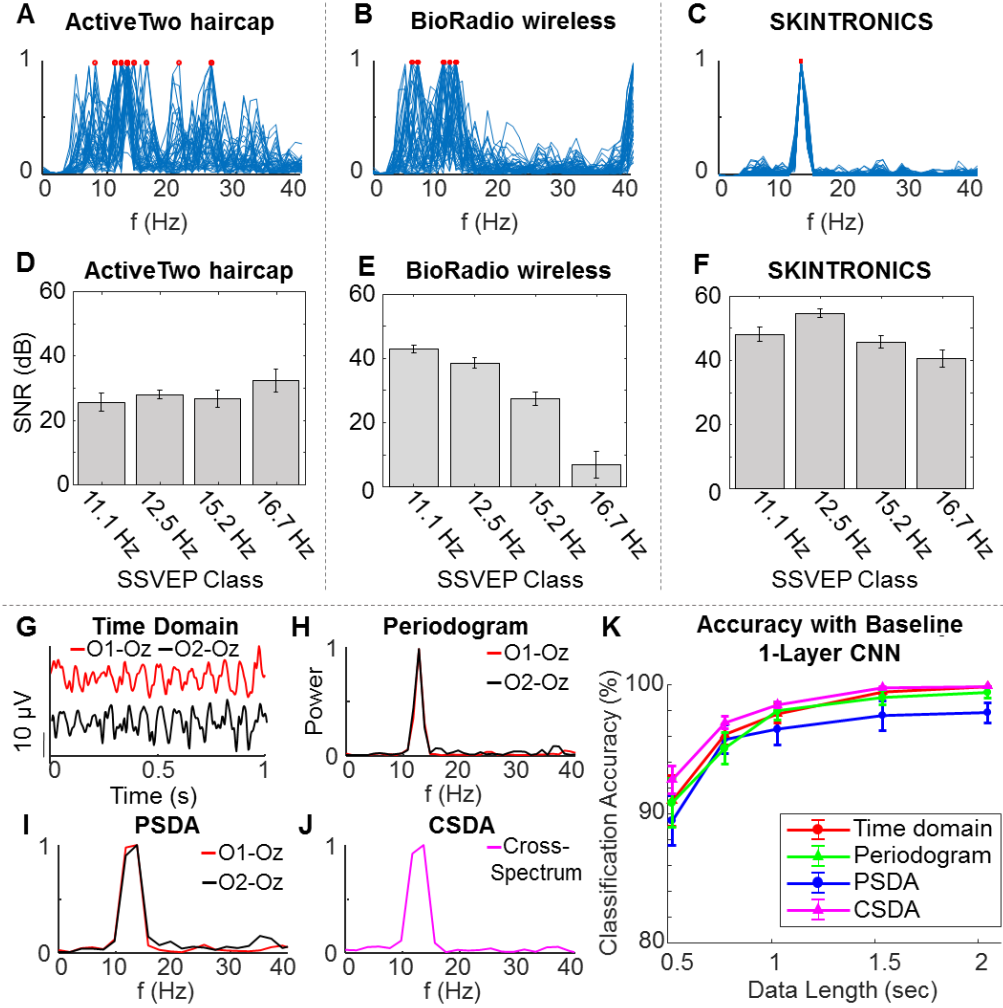


Figure 40. Analysis of the device performance in signal quality, feature extraction and classification accuracy. Three data sets for a conventional hair cap system (ActiveTwo; *1st* column), bulky clip-on wireless system (BioRadio; *2nd* column), and our 2-channel SKINTRONICS (*3rd* column). (A-C) Periodograms of 50 samples from 12.5 Hz SSVEP signals overlaid over each other, with peaks highlighted with red circles; this comparison illustrates our device's ability to target and capture SSVEP signals without excessive noise precisely and consistently. (D-F). Average signal-to-noise ratio (SNR) with four SSVEP classes, across all six tested subjects. Error bars represent standard error of the mean ($n=60$ recordings; 6 subjects, 10 recordings each). (G) Two-channel SSVEP data at 12.5 Hz in time domain by using 4 Hz Butterworth high-pass filter and removed baseline drift. (H) Further preprocessing in the form of frequency-analysis including a single-window periodogram. (I) Welch power-spectral density analysis (PSDA) overlapping periodogram. (J) Cross-spectral density analysis (CSDA) of both channels. Note that the cross-spectral input includes the normal Welch power spectrum, resulting in three feature sets to the 1-layer CNN. (K) Comparison of classification accuracy between four preprocessing methods, shown in (G-J). The points on the graph are the mean accuracies

from 36 trials from all 6 test subjects. Error bars represent standard error of the mean ($n = 36$ trials).

The side-to-side comparison of data captures the superior performance of the SKINTRONICS (Figure 40A-C) with the consistent and overlapping peaks at 12.5 Hz from the first channel (O1-Oz). In these panels, periodograms from 50 consecutive 1-second sample windows with 128 ms overlap from a single subject are overlaid on a single graph to demonstrate the signal variance from each of the three devices. Signal-to-noise ratio (SNR) analysis (Figure 40D-F) for all 6 subjects was performed offline in a numerical program (MATLAB, MathWorks). SNR was calculated from a continuously recorded 10-second sample, using the computed periodogram with 2048-point (8.192 sec) overlapping windows for each of the four stimuli. Data for each subject were recorded consecutively on the same day, starting with the ActiveTwo, followed by the BioRadio, and finally the SKINTRONICS. Care was taken to record all the trials within the shortest timespan, to reduce the possibility of bias in recording, as the EEG response is known to vary over the course of a day. The recordings from all three devices were performed within two hours. The setup time for the ActiveTwo was about half an hour for each subject. The BioRadio and SKINTRONICS systems were easier to set up due to the use of fewer electrodes, and both took about 15 minutes to set up for each subject. The time required to record all the training and test data was about 13.5 minutes, for each system, with each individual trial being 75 seconds, with a minute break in between each of the six trials. Set up time includes skin preparation time and checking the electrode impedance before starting trials.

Among the three systems, the SKINTRONICS shows the highest average SNR (46.6 ± 2.16 dB) from four SSVEP classes, measured with 6 human subjects (Figure

40D-F). This shows that SKINTRONICS SNR is a significant improvement over the conventional gel-based system (ActiveTwo; 16.94 ± 4.60 dB) and the portable wireless system with dry electrodes (BioRadio; 28.89 ± 2.28 dB). The dramatic difference in SNR is due to the novelty of the form-factor and conformal mounting of the SKINTRONICS, such that it is isolated from external electromagnetic interference, movement artifacts, and drift of gel electrodes. Here, the use of much shorter wires connecting the electrodes to the ADC in the SKINTRONICS provides the main difference in signal quality. The BioRadio and ActiveTwo devices both have long wires that are affected by minute movements of the head. As the short wires on the SKINTRONICS are secured to the head using the headband, and the device is also secured to the head, these movement artifacts are far less pronounced. A summary comparing the cable lengths of the different systems are given in Table 5. As the short wires on the SKINTRONICS are secured to the head using the headband, and the device is also secured to the head, these movement artifacts are far less pronounced. Due to its relatively low power requirements, the low-profile SKINTRONICS runs off a single Li-Po battery (capacity: 40 mAh) with minimal power supply interference. This ensemble effect causes the device to specifically target EEG signals with minimized noise.

Table 5. List of EEGs and Cable Length for Each System.

System Name	Cable Length	Active Electrodes
ActiveTwo	140 cm	Yes
BioRadio	100 cm	No
SKINTRONICS	18 cm	No

The conformal lamination of the SKINTRONICS on the back of a subject's neck is another factor to isolate excessive motion artifacts, compared to bulky portable device (belt clip-on device; BioRadio). This arrangement also places the device close to the

signal source on the scalp, minimizing introduction of noise before the first gain stage. Devices using dry electrodes typically require active shielding on high-impedance input amplifiers and electrodes to protect from interference and noise [80, 81]. However, the use of elastomer as passive shield, combined with the use of a low-impedance ground effectively provides the same results with dry and non-contact electrodes [81]. Using tiny, thin film cables allow the device to significantly reduce potential noise input by simply reducing the overall size of the device. A reduction in size and complexity serves to reduce noise levels in electrophysiological measurement systems, as the device and cables act as antennae that pick up electromagnetic interference[82]. Additionally, longer cables that are not properly secured may cause dragging and drift artifacts due to movement [83]. Overall, the results comparing the SKINTRONICS with two commercial systems, suggest that a low-profile, portable device garners superior SNR to larger systems that require longer leads and higher capacity power source.

To further quantify the SKINTRONICS performance, we conducted a canonical correlation analysis (CCA; details in the Appendix under

Frequency component analysis with CCA). Our system achieves an average accuracy of $89.6 \pm 2.1\%$ at the shortest data length of 0.512 seconds for four SSVEP classes over 6 human subjects (details of original datasets appear in Figure 41). The primary metric used to establish the efficacy of the EEG system is information transfer rate (ITR), calculated in bits per unit time (details may be found in the Appendix under *Calculation of Information Transfer Rate*). For each instruction relayed through the interface, the incoming EEG data was evaluated three times, every 64 ms. As actions are taken if three consecutive windows are consistent, it provides an additional layer of protection for the user of the interface to reduce likelihood of incorrect commands transmitted to targets. Using this method, the 4-class classification results using CCA results in an ITR of 77.63 ± 5.32 bits per minute, with window length, $w=0.94$ s, adjusted for gaze-shifting (+300 ms) and confusion protection (+128 ms).

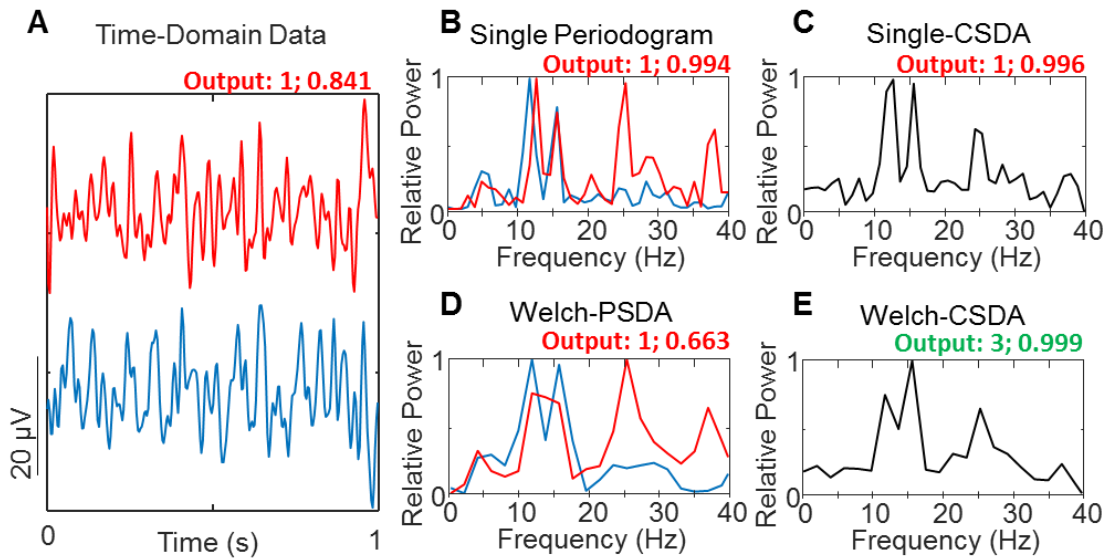


Figure 41. Feature representations using power and cross-spectral analyses. (A) A filtered EEG sample encoded with a noisy 15.2 Hz SSVEP signal in channels O1 and O2. (B) A simple periodogram using a window of equivalent length (single window periodogram). (C) The cross-spectral estimate of the single-windowed periodograms. This result may be

improved by using windows of 0.5-second length with 50% overlap (Welch's method), as seen in (D). Now, the 15.2 Hz peak is better represented, but still contains a peak around 11Hz. Taking the cross spectral estimate with Welch's method gives us (E), which most closely represents the intended frequency content. In this example, the baseline CNN trained for classifying cross-spectral density data predicts the correct class. The labels show the predicted class and softmax output probabilities, where red represents a false classification output, and green represents the correct output.

To improve upon the classification accuracy achieved using CCA, we utilized support vector machines (SVMs) and CNN[20]. Analysis includes comparison of time-domain and frequency-domain data using identical windows from the initial source in the form of single-window periodogram analysis and Welch power spectral density analysis (PSDA). A final coherence-based method, cross-spectral density analysis (CSDA) was also implemented due to its ability to analyze the coherence of multiple channels, allowing for more precise frequency decomposition versus single-channel PSDA. Time domain signals were preprocessed using 3rd order Butterworth high-pass filter with a cutoff frequency of 4 Hz to remove DC offset and baseline drift. Due to the high quality of the source signals, no other digital filtration was found to significantly improve classification. These feature extraction methods are used to compare the learned feature-extraction capability of CNN versus manual feature extraction with SVMs using various kernel functions (linear, quadratic, cubic, Gaussian).

The procedure for gathering training data involved a continuous EEG recording with 15 seconds for each class, separated by auditory cues. The classes were recorded in order of alpha rhythms, for the first 15 seconds, followed by 15 seconds of gazing at four different LED stimuli. Here, each recording where all five classes are performed constitutes a single trial. This trial was performed 6 times for each subject. Note that the experimental method for gathering training data is not the same as the experimental

testing method. To train the convolutional neural networks, the training data were subdivided into window sizes of 128, 192, 256, 384, 512 data points (corresponding to 0.512, 0.768, 1.024, 1.536, 2.048 sec data windows) were selected to gauge changes in accuracy over different window sizes. Empirical data from the SKINTRONICS suggested that training from a continuous stimulus was significantly more effective use of training data than a faster (< 1 second) cue-guided task. This may be because the relevant SSVEP features required for training are most optimal during these longer sessions of looking at the stimulus. The recording procedure for training and test data allowed for an additional 0.3 seconds for gaze-shifting between stimuli. From the training set, there were 2700 samples from each subject used, 450 samples from each of the 6 recordings. Therefore, for 5 subjects, a single training epoch consisted of training on 13,500 samples. For testing classification performance, a total of 30 individual stimuli were presented, for a total of 0.704 seconds, which allowed for classification of three consecutive 0.512ms samples. This was used as a safety mechanism for the control interface, where action would only be taken with a majority decision (2 or more classes match). Combined with gaze shift time, that brings the length of the window used up to 0.94 seconds ($0.512+0.3+0.128$ s). This same process was repeated for all the different window lengths. As a result, for each subject there were 450 samples of test data per trial for each window length, 90 for each class.

The aim of this research is to show the universal capability to classify SSVEP from two channels on any subject. Therefore, 6-fold cross-validation is performed on a subject-to-subject basis with five subjects' training data used to train the model, and the remaining subject's test data used for evaluation. This validation method was performed

with both the CNN and the SVM models. For the CNN, the training involved feeding a training batch of 256 and a test batch of 100 samples in each iteration. Following 3000 training iterations (approximately 57 epochs), or, if no validation improvement occurs after 150 training steps, the training terminates. The test sets are subsequently evaluated for accuracy. Figure 40G-K demonstrates each of these preprocessing and analysis methods by using a 1.024-sec segment at 12.5 Hz SSVEP. Two-channel (O1-Oz and O2-Oz) time-domain data (Figure 40G) is converted to a single-window periodogram (Figure 40H), PSDA (Figure 40I), and CSDA (Figure 40J). The summary of resulting accuracies from 4 datasets appears in Figure 40K. These preliminary results suggest that the basic network most effectively extracts features from CSDA and time-domain data. In this example, details of the feature extraction of four types of methods are summarized in Figure 42. A noisy sample at 15.2 Hz is incorrectly classified when evaluated in time-domain, single periodogram, CSDA, and PSDA. However, the correct output is achieved with the combination of CSDA and using overlapping window (Figure 42E). The details of PSDA and CSDA methods are shown in Section S6 and Section S7, respectively.

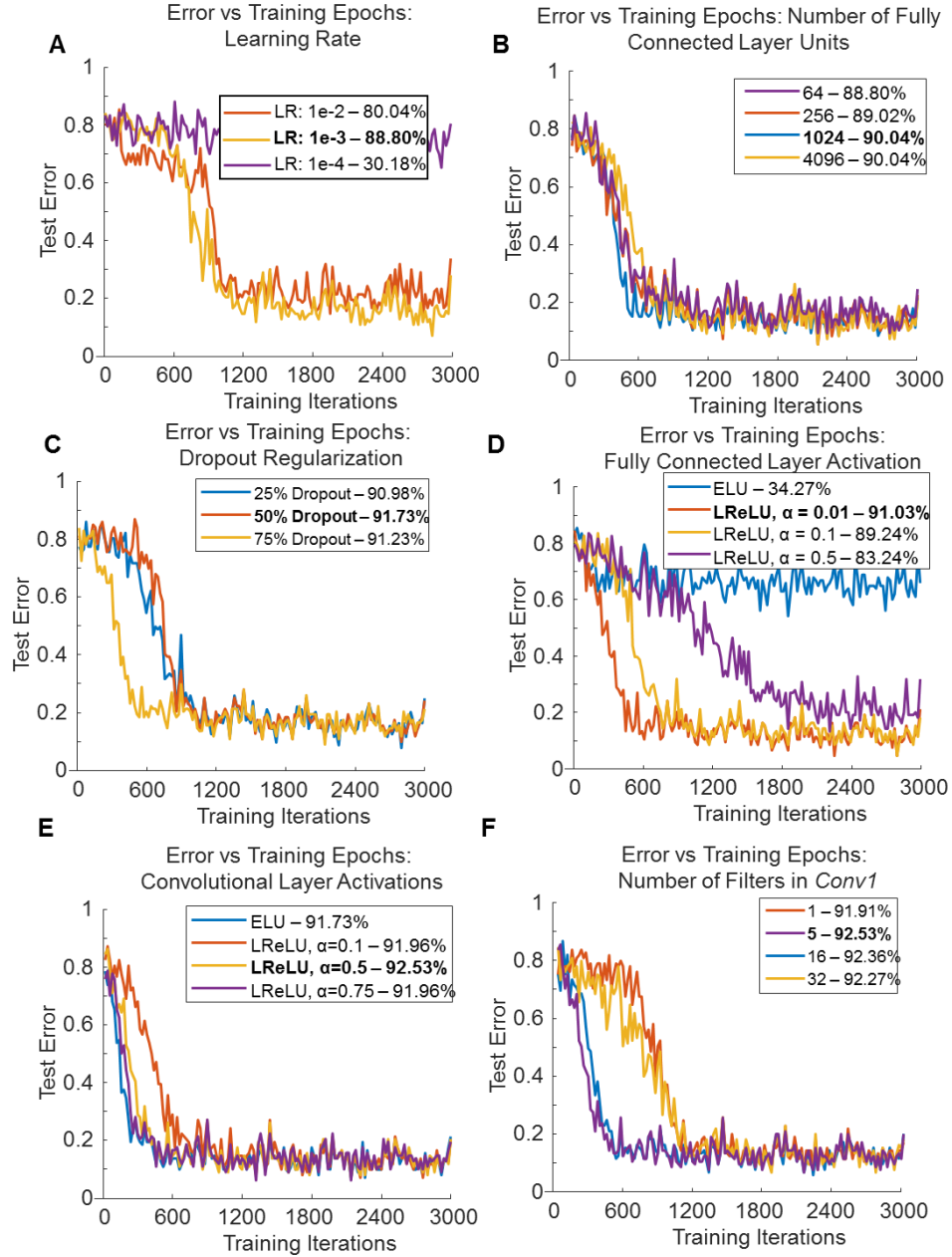


Figure 42. Hyperparameter Optimization of 1 Layer Convolutional Neural Network. (A) Different learning rates between $1e-2$ and $1e-4$ were tested in, followed by number of units in the fully connected layer in (B). (C) Dropout regularization in between 25% and 75% is then added and analyzed. (D) Different activations in the fully connected layer are added. It appears that ReLU activation performs more optimally in the fully connected layer. (E) The activations following the convolution operation were varied, with LeakyReLU performing most optimally. (F) The number of filters was varied from 1 to 32, with 5 filters providing the most optimal performance with $92.53 \pm 1.01\%$.

4.2.3 *Grid-search optimization of CNN*

With shared weights, CNN can detect features on either channel at any location, while keeping the size of the network relatively small[84]. In all models, these filters and other trained variables were optimized through the use of an optimization algorithm with a constant learning rate (Adam, learning rate=0.001, $\beta_1=0.9$, $\beta_2=0.999$)[85], and error was calculated using the cross-entropy loss function. The input to the network is a 2D array of $(n, 2)$, where n is the number of data points for a window sampled at 250 Hz (e.g. $n=128$, for a window length of 0.512s), and the 2 represents each of the two channels. As summarized in Figure 43, multiple convolutional layers allow for detection of low-level features that cannot be detected with a single filter. It also allows for down-sampling and collection of relevant activations from previous layers, to be classified by a fully-connected layer. This work optimizes the baseline CNN through two stages of improvements, adjusting components and hyperparameters on a single layer. A grid search approach was used because training for such a small dataset could be completed in a few minutes on consumer hardware, and it was reasonably efficient to find an optimal solution. First the optimum parameters are determined for a CNN with 1 convolutional layer and 1 fully connected layer before the output layer. This model is then expanded to multiple layers, as needed, to further improve accuracy. In Figure 43A, we represent ‘active’ features using a gray-scale representation of the time-series data. Here, 50 2D-convolutions are performed across each channel, resulting in 100 outputs total. An additional 100 2D convolutions are performed on the second convolutional layer, resulting in the outputs shown in Figure 43B. A fully connected layer of 1,024 units is produced, followed by a fully connected output layer with 5-class SoftMax activation

(Figure 43C). Mean accuracy results from SVM and CNN models for time-domain and CSDA data are shown in Figure 43D and Figure 43E, respectively. Of the four SVM kernel types tested, the highest accuracy results were chosen (cubic kernel) to be displayed for all results.

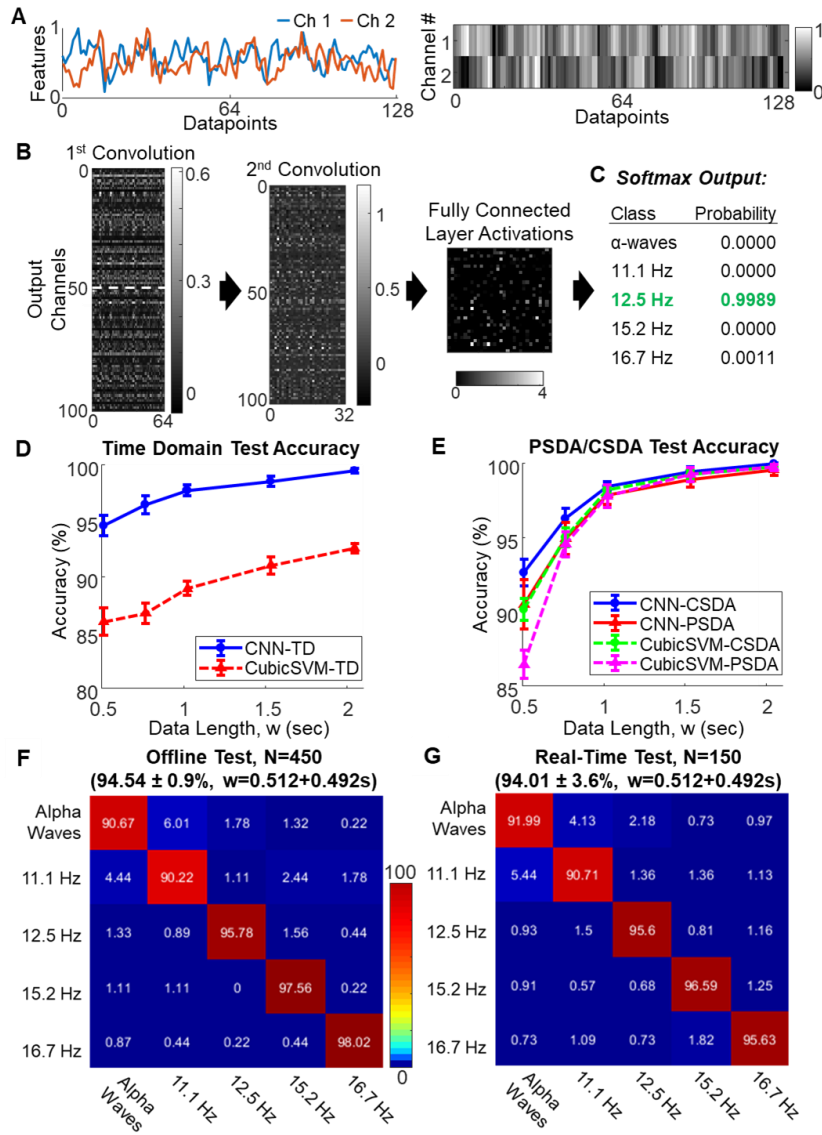


Figure 43. EEG classification with CNN. (A) High-pass filtered raw EEG data in time domain with features linearly rescaled between 0 and 1, labeled as SSVEP class ‘12.5 Hz’, along with a representative greyscale image. (B) Greyscale representation of output weights in the two layers of CNN as well as in the fully connected layer using the 2-CNN model for time domain data. (C) Table of softmax class outputs, indicating a correct choice with 99.89% probability. (D) CNN and SVM classification test accuracy using time domain data and cross-validating across all subjects. (E) CNN and SVM test accuracy on frequency-domain data, cross-validating across all subjects, with window lengths from 0.512 to 2.048 seconds. The displayed results are from the strongest SVM of the four tested (cubic kernel). (F) Confusion matrix representing results from offline accuracy test of time-domain data of data window length $w=0.512$ s, with an overall accuracy of 94.54% ($n=2700$ samples; 6 subjects, 450 samples each). (G) Confusion matrix representing results from real-time accuracy test of time-domain data of length

$w=0.512s$, with an overall accuracy of 94.01% ($n=2700$ samples; 6 subjects, 450 samples each).

This serves to establish universal applicability for the acquisition of SSVEP using only two-channel SKINTRONICS. Multiple support vector machines were used to train the same datasets as were used to train the CNN. The same subject-to-subject cross-validation scheme was used for all training models. The results show the SVM models able to achieve high accuracies with frequency-domain features for all kernel types. However, the linear SVM failed to classify time domain signals beyond trivial accuracies. Overall, the optimized 2-layer CNN was superior in all situations, due to its inherent ability to extract low-level features through shared weights and its ability to detect many features that standalone SVMs cannot. Based on this evidence, this system and classification model can be trained on a small group of individuals and used in universal SSVEP-based BMI applications. To further emphasize these offline results, a confusion matrix, representing the results from the shortest data window input ($w = 0.512$ seconds) is summarized in Figure 43F where the wireless scalp system achieves a high accuracy ($94.54 \pm 0.90\%$) for a corresponding information transfer rate of 122.1 ± 3.53 bits per minute. In comparison, real-time cue-guided SSVEP test data across all six subjects shows the accuracy of $94.01 \pm 3.6\%$ (Figure 43G). These results show a consistent level of accuracy even with real-time classification, which allows for precise control over different interface targets, including an electronic wheelchair, wireless mini-vehicle (Figure 44).

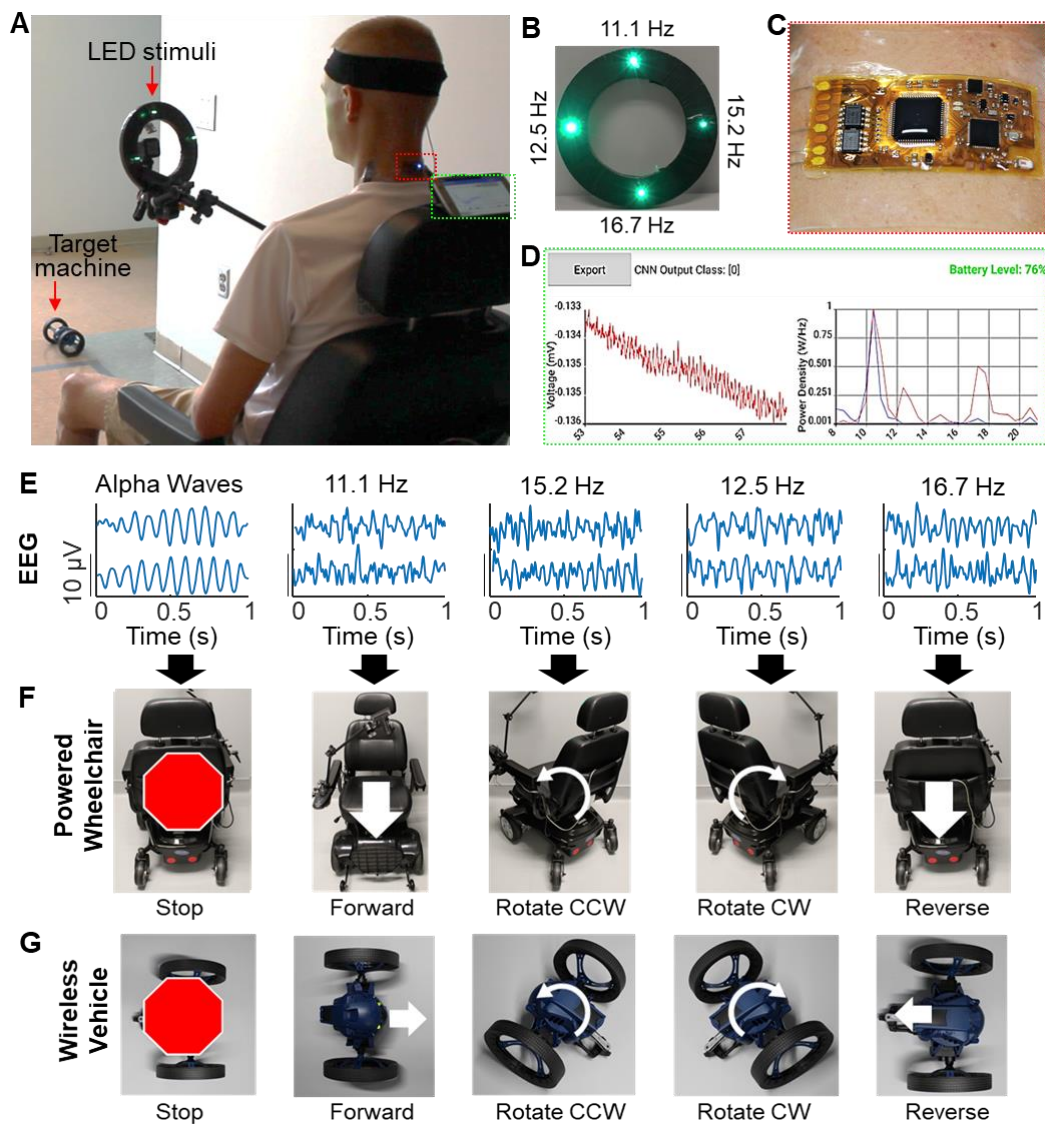


Figure 44. *In vivo* demonstration of wireless, portable BMI with human subjects. (A) Subject seated in a powered wheelchair with the LED stimulus array (B) and SKINTRONICS secured and conforming to the back of the neck (C). (D) Android user interface during training and evaluation, showing time-domain data, corresponding power spectrum, and output class. (E) EEG data recorded at each state, labeled as alpha rhythms, 11.1 Hz, 15.2 Hz, 12.5 Hz, 16.7 Hz SSVEP respectively. (F-H) Three target machines to control via SSVEP signals, including a wireless electronic wheelchair (F) with 5 classes (no action, forward, rotate counterclockwise, rotate clockwise, and reverse), and wireless vehicle (G) with the same commands as the wheelchair, and PowerPoint presentation (H) with 5-class actions (no action, begin presentation, next slide, previous slide, and end presentation, respectively). To compare SKINTRONICS to commercial systems, the same optimized CNN procedure was performed on data from the BioRadio and ActiveTwo systems.

A plot comparing the data from all three systems is shown in Figure 45, showing a clear gulf between the accuracies of the SKINTRONICS and the other two systems. This data is supported by the difference in SNR, as discussed previously.

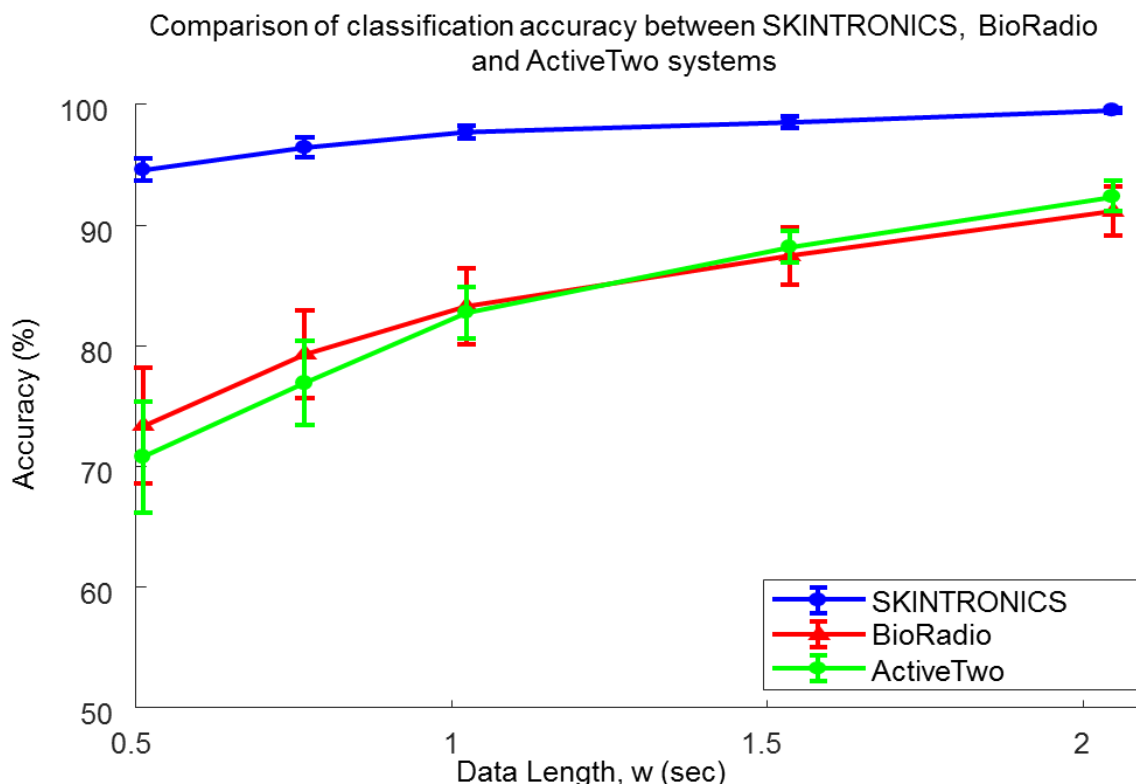


Figure 45. Comparison of classification accuracies of time domain data from SKINTRONICS, BioRadio and ActiveTwo systems using optimized CNN model.

4.3 Results of 5-target SSVEP-based navigation interface

In this work, we demonstrate the feasibility of the SKINTRONICS for a portable, wireless BMI via SSVEP from 6 human subjects (Figure 44). For the experiments, subjects were seated in front of the LED stimulus setup, about 0.8 m away from their head at eye level where all four stimuli are presented simultaneously (Figure 44A). A subject conducts five tasks; gazing at each LED stimuli, and a null task (eyes closed, for

alpha rhythms) and gazing four LED locations (Figure 44B), while the SKINTRONICS securely conforms to the back of the subject's neck (Figure 44C). The EEG data is recorded, displayed and saved in real-time, along with the corresponding classification outputs on an Android-based mobile device (Figure 44D). Impedances between the hair mount electrodes to ground were maintained below 20 k Ω . Due to the use of flexible contacts of the scalp-mounted dry electrode and skin-like electrode on the mastoid, we maintained relatively low skin-electrode contact impedance. For all experiments, we used 250 Hz sampling rate. An Android-based operating system was selected to demonstrate functionality and feasibility of a fully portable, wireless BMI. The SSVEP data transmitted from the SKINTRONICS was received by a Bluetooth enabled smartphone (Samsung Galaxy S7). The data was preprocessed and fed into the trained CNN for classification on the smartphone. The output of the classification was directly used to control the interface target. A set of representative EEG data from 5 classes appears in Figure 44E, including alpha waves and 5 SSVEP data of 11.1, 15.2, 12.5, and 16.7 Hz. A subject uses these data to control three target machines, including a wireless electronic wheelchair (Pronto, Invacare; Figure 44F), a wireless mini vehicle (Minidrone, Parrot; Figure 44G). For the electronic wheelchair and wireless vehicle, the methods of control are the same as they are both two-wheel drive vehicles. When the subject has their eyes closed, the vehicle does not move, and only begin to move once SSVEP is classified by the central processing device. The top LED (11.1 Hz) is used to program the forward motion of the wheelchair and vehicle. The right-facing 15.2 Hz LED results in a counter-clockwise rotation, while the left-facing 12.5 Hz results in a clockwise rotation. The final 16.7 Hz LED operates the reverse functionality. For the presentation control interface, the

top LED initiates the start of the presentation, the right LED proceeds forward through the slides, and the left LED reverts to the previous slide. Lastly, the bottom LED terminates the presentation. This simple functional interface illustrates the potential of the SKINTRONICS to be easily implemented in many rehabilitation applications, as the controls can be easily reassigned to any target with equivalent or fewer targets. Additionally, this method can be scaled up to include a greater number of classes, which was previously not possible due to a lack of signal quality. Overall, subjects were able to achieve highly accurate and precise real-time control of three target machines with $94.01 \pm 3.6\%$ accuracy at 0.512-second intervals and $96.24 \pm 3.4\%$ at 1.024-second intervals. Subjects with various hair types and conditions were selected to ensure the electrodes could perform in various scenarios. A table detailing the hair types of each of the subjects is shown in Table 6.

Table 6. Subject Information: Ethnicity and Hair Conditions. This table demonstrates the variety of hair conditions among the subjects and shows the consistent SNR achieved using the SKINTRONICS system.

Subject Number	Ethnicity	Hair thickness	Hair Length	Mean SNR (dB)
S1	Caucasian	Sparse	Long	40.1 ± 4.9
S2	Asian	Dense	Short	54.9 ± 2.4
S3	Caucasian	Dense	Short	37.2 ± 9.1
S4	Caucasian	Sparse	Very Short	60.4 ± 2.2
S5	Caucasian	Dense	Short	64.2 ± 1.5
S6	Asian	Dense	Short	60.3 ± 3.9

4.4 Discussion and Analysis

The collection of materials presented here reports that a fully portable, wireless, ergonomic SKINTRONICS offers highly accurate, real-time monitoring of SSVEP on the scalp for a BMI. The flexible hybrid electronic system integrates a highly conformal

wireless circuit on the back of the neck, a skin-like membrane electrode on the mastoid, and three flexible conductive electrodes on the occipital lobe. The extremely small form factor and associated portability of the low-power SKINTRONICS makes it less prone to interference and movement artifacts. The adherence to the skin and mechanically compliant electrodes allows for reasonable flexion and movements without any significant artifacts added to the EEG signals. Provided these advantages, locations of highest signal density may be targeted with fewer electrodes, producing high resolution signals from the areas of highest signal density. The electrode configuration is designed to target a consistently high SSVEP SNR across all subjects. A custom optimized algorithm using deep-learning CNN provides real-time, highly accurate classification of SSVEP and a highly efficient information transfer rate with only two channels (122.1 ± 3.53 bits per minute; Table 7), enabling precise control of a wireless wheelchair, motorized mini-car, and a presentation software. To mitigate risk of collisions or accidents when piloted by motor-limited subjects, the wheelchair can use collision prevention systems incorporating infrared or other proximity sensors[86]. Additionally, the wheelchair can be bound to a specific set of paths to prevent accidents arising from misclassification.

This result is significant due to the decreased number of channels used when compared to other systems and is also fully integrated for comfort and a low profile. Due to the decreased number of channels, correlation-based analyses such as canonical correlation analysis (CCA) and task-related component analysis (TRCA) could not be used with 2 channels. This control demonstrated by healthy subjects may easily be learned by subjects with weak or nonexistent motor control (locked-in syndrome),

requiring only movement of the eyes and closure of the eyelids. Using high-quality signals over a targeted two channels, combined with an optimum classification method, we can achieve a high accuracy with limited information, generalized enough to be used with any subject, demonstrating the possibility of a universal BMI.

Table 7. Comparison of information transfer rate (ITR) between the SKINTRONICS and reported values.

	Year	Accuracy (%)	Length (sec)	# of classes	# channels	of ITR (bits/min)	
<i>This work (SKINTRONICS)</i>	2019	94.54	0.94	5	2	122.1 ± 3.53	
Nakanishi et al.[87]	2018	89.83	0.8	40	9	325.33 ± 38.17	
Chen et al.[88]	2015	91.09	1	40	9	270.0 ± 61.8	
Bevilacqua et al.[89]	2014	95.61	2	3	4	38.44*	
Kwak et al.[20]	2017	99.19	2	5	8	67.13*	
Volosyak et al. [90]	2011	96.79	2	5	8	61.70 ± 32.68	
Lin et al. [91]	2007	73.00	1.5	9	8	60.74*	
Bin et al. [92]	2009	95.30	2	5	8	58.6 ± 9.6	

4.5 Conclusion

Overall, this research reports fundamental strategies to design an ergonomic, portable EEG system for a broad range of rehabilitation and therapeutic applications. Future studies would focus on investigation of including a greater number of classes and reducing eye strain by using a virtual reality headset to immerse the subject into the training environment.

SSVEP-BASED VR TEXT SPELLER FOR COMMUNICATION

5.1 Virtual Reality Environment

As shown in the previous two sections, we can see the potential in using flexible electronics for EEG data acquisition. Additionally, we showed that SSVEP, despite its limitations of requiring a stimulus in front of the subject, can still be utilized for navigation purposes. However, there were many issues with these systems, as will be detailed. First, the PI-based needles have many issues including poor yield, low mold lifespan and a generally tedious and wasteful process, which is tackled and discussed in a later section. The serpentine interconnects are only insulated on one side, and therefore require some additional coating after processing in order to function correctly. Uncoated interconnects were prone to tangling and were very difficult to untangle. Elastomer coatings often caused more artefacts through electrostatic effects[26], and defeated the purpose of using thin, insulated interconnectors. Finally, SSVEP interfaces work well for applications such as navigation, where a few targets are needed to move in a few directions but are not useful where more commands are needed. In this section we are going to demonstrate how we attempted to solve each of these shortfalls and created an optimal, fully mobile SSVEP-based text speller VR interface with a multitude of potential real-world applications.

A virtual reality environment provides many advantages that a simple computer screen does not. Firstly, it allows for an immersive environment allowing a BMI user to focus on the task at hand, which has been shown to vastly improve classification accuracy and BMI literacy[13, 43]. Secondly it has an interesting property where each

eye does not see the same screen; each eye sees a separate display, which is demonstrated in order to effectively double throughput.

5.1.1 Stage 1: 11-target stimulus environment

To test the feasibility of using VR as a stimulus for a high-throughput SSVEP-based interface, a VR training environment was developed using a cross-platform software development engine (Unreal Engine 4.26, Epic Games Inc.). The paradigm used is shown in Figure 46. Here the mobile tablet features as a data collector and central processor. Data is transferred from the EEG devices to the tablet where it is processed and classified in real-time and the results are transmitted to the target headset.

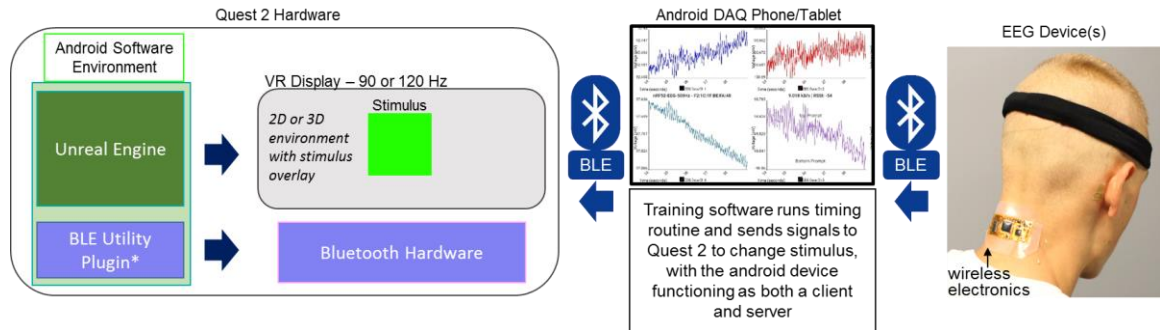


Figure 46. Flowchart demonstrating information flow for training environment

In this first stage, the aim is to establish feasibility using a 10-target SSVEP stimulus setup, using standard stimuli (both eyes experience same visuals), listed in Table 8. In this experiment, each stimulus is presented one at a time for four seconds each, separated by 2 seconds to allow the subject to relax. These trials were recorded 20 times for a total of 22 minutes of data per subject. The stimulus data is then segmented into windows of various length and classified using a CNN with spatial filters (see *Feature*

extraction and classification in Chapter 3). The results from a 5-fold cross-validation scheme based on the Stage 1 data recorded is presented in Table 9.

Table 8. List of Targets and Stimuli for Stage 1 VR Training Setup

Class #:	Desc	Lfreq	Lphase	Rfreq	Rphase
0	Eyes Closed			N/A	
1	Stage1_1	10.0	0.00	same	same
2	Stage 1_2	10.8	1.75	same	same
3	Stage 1_3	11.6	1.50	same	same
4	Stage 1_4	12.4	1.25	same	same
5	Stage 1_5	13.2	1.00	same	same
6	Stage 1_6	14.0	0.75	same	same
7	Stage 1_7	14.8	0.50	same	same
8	Stage 1_8	15.6	0.25	same	same
9	Stage 1_9	16.4	1.85	same	same
10	Stage 1_10	17.2	1.60	same	same

Table 9. Demonstration of cross-fold validation of 11-class Stage 1 dataset using Spatial CNN with 1-second windows.

Subject	1	2	3	4	5	Mean	Std. Error	ITR (bits/min)
S1	99.3%	91.5%	99.0%	99.0%	99.9%	98.3%	0.7%	197.0
S2	94.6%	96.1%	91.3%	96.1%	95.6%	93.7%	1.8%	174.5
S3	97.5%	99.1%	98.6%	98.7%	99.0%	98.2%	0.4%	196.2
S4	88.6%	90.2%	88.5%	94.3%	93.5%	90.8%	1.0%	162.5
S5	93.0%	89.3%	96.6%	97.2%	97.9%	94.9%	0.8%	179.9
S6	98.2%	93.7%	98.2%	97.4%	95.7%	97.2%	0.5%	191.1
S7	96.0%	81.4%	98.9%	99.4%	99.7%	96.4%	1.6%	186.9
S8	97.2%	76.9%	95.0%	81.5%	94.6%	90.8%	2.1%	162.7
Average						95.04%	1.11%	180.6

5.1.2 Stage 2: 9-target dual-stimulus concept

For the second stage of testing, we introduced the per-eye stimulus system, where, for each stimulus, each eye would be presented with a different frequency, and each class would have a unique combination of frequencies for the left and right eye. In theory, if the information is retained to the same degree when compared to that of a single-

frequency stimulus, this allows us to effectively double the information we can pass through this BMI-based system. The details of which frequencies are used in which eye are shown in Table 10, and the cross-validation results are presented in Table 11.

Table 10. List of Targets and Stimuli for Stage 2 (per-eye) VR Training Setup

Class #:	Desc	Lfreq	Lphase	Rfreq	Rphase
0	Eyes Closed	N/A			
1	Stage 2_1	10.0	0.00	16.9	1.00
2	Stage 2_2	11.1	1.75	15.8	0.75
3	Stage 2_3	12.2	1.50	14.7	0.50
4	Stage 2_4	13.3	1.25	13.6	0.25
5	Stage 2_5	14.4	1.00	12.5	0.00
6	Stage 2_6	15.5	0.75	11.4	1.75
7	Stage 2_7	16.6	0.50	10.3	1.50
8	Stage 2_8	17.7	0.25	9.2	1.25

Table 11. Demonstration of cross-fold validation of 9-class Stage 2 dataset using Spatial CNN with 1-second windows.

<i>Subject</i>	<i>1</i>	<i>2</i>	<i>3</i>	<i>4</i>	<i>5</i>	<i>Mean</i>	<i>Std. Error</i>	<i>ITR (bits/min)</i>
S1	92.6%	92.6%	91.8%	94.6%	95.5%	94.3%	0.6%	177.4
S2	96.9%	92.4%	94.7%	96.8%	95.6%	95.7%	0.5%	183.5
S3	94.0%	83.0%	91.7%	90.0%	93.4%	91.9%	1.1%	167.2
S4	93.3%	94.2%	92.1%	96.7%	89.7%	93.2%	0.7%	172.4
S5	92.0%	83.7%	97.6%	93.9%	94.9%	91.4%	1.3%	165.2
S6	66.8%	71.9%	74.4%	79.6%	70.9%	70.4%	1.9%	96.0
S7	95.0%	88.4%	95.1%	98.7%	98.4%	96.0%	0.9%	185.2
S8	64.8%	63.7%	62.4%	70.2%	59.9%	65.3%	1.1%	82.6
Average						87.29%	1.01%	149.2

5.1.3 Stage 3: Final 33-target Text Speller

The final text speller setup uses a combination of matched frequencies in both eyes and per-eye stimuli, as shown in Figure 47, where the rows in red show standard SSVEP stimuli, and the rows in blue show the per-eye stimuli; where the number given first is the frequency of the stimulus presented to the left eye, and the number after the ‘/’ is the frequency of the stimulus presented to the right eye.

A	7.8	8.4	9	9.6	10.2	10.8	11.4	12
	7.5/11.8	8.1/12.4	8.7/13	9.3/13.6	9.9/14.2	10.5/14.8	11.1/15.4	11.7/16.0
	12.6	13.2	13.8	14.4	15	15.6	16.2	16.8
	12.3/8.0	12.9/8.6	13.5/9.2	14.1/9.8	14.7/10.4	15.3/11	15.9/11.6	16.5/12.2
B	A	B	C	D	E	F	G	H
	I	J	K	L	M	N	O	P
	Q	R	S	T	U	V	W	X
	↑/↓	,	NEWLINE	SPACE	SUBMIT/ RESET	.	Y	Z

Figure 47. Default text speller interface layout. (A) Frequency of each stimulus tile in Hz and (B) corresponding command on default English keyboard.

5.2 Tangle-resistant high-throughput interconnects

As mentioned previously, the main issues with the interconnects included an issue where the serpentine interconnects are only insulated in one side, and therefore require some additional coating after processing to function correctly. Uncoated interconnects were prone to tangling and were very difficult to untangle. Elastomer coatings often caused

more artefacts through electrostatic effects[26], and defeated the purpose of using thin, insulated interconnectors. Therefore, the connectors were redesigned to prevent tangling, insulation of both sides of the conductor, and improve overall robustness at the cost of reducing maximum strain before yield. These connectors were then evaluated in a similar manner as the connectors in Chapter 3, as shown in Figure 48.

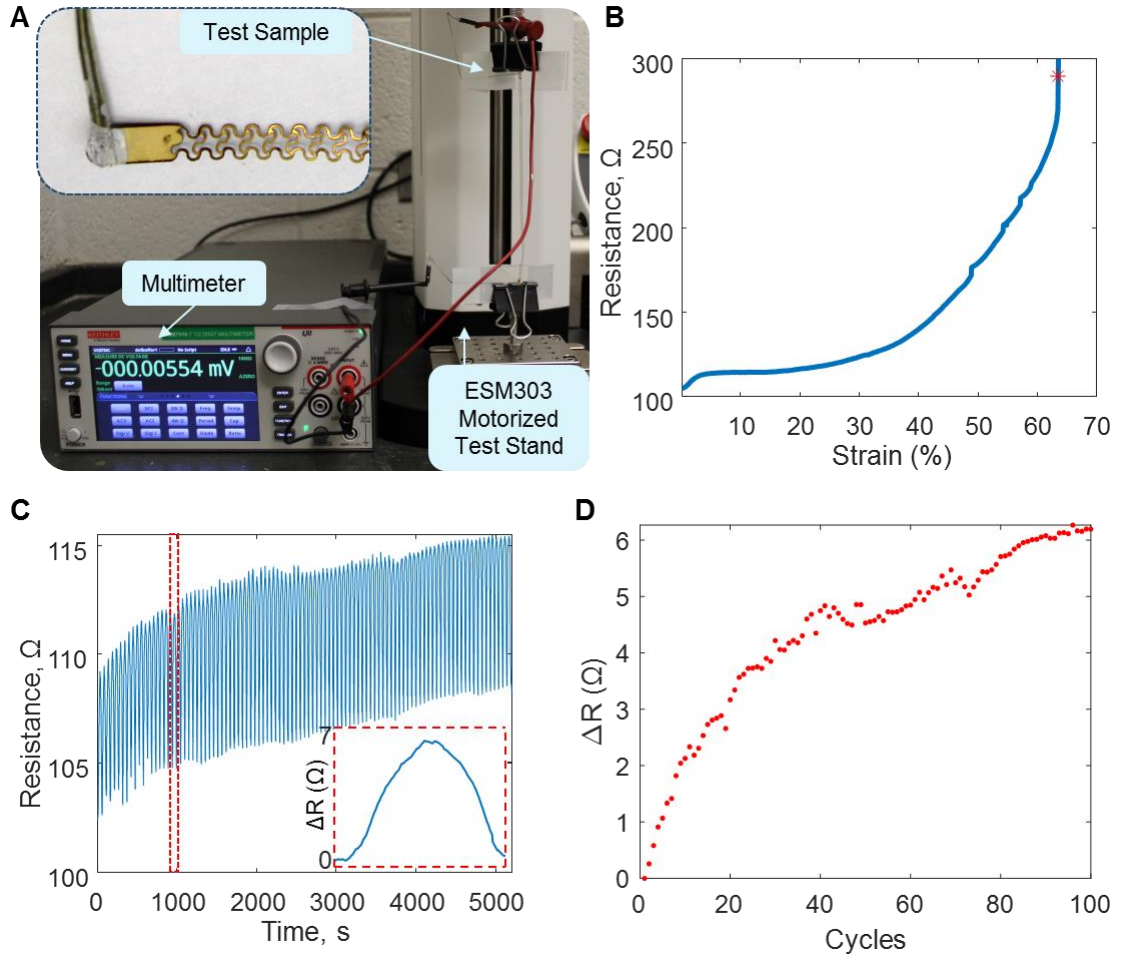


Figure 48. Characterization of stretchable EEG interconnectors. A) Photos showing test setup with benchtop DMM connected to sample. The sample is connected using ACF cables using silver paint. B) Measurement of electrical resistance change showing mechanical fracture after ~65% of tensile stretching. C) Cyclic tensile stretching of up to 20% strain for 100 cycles, with minimal resistance changes. D) Peak resistance change per cycle over 100 cycles.

5.2.1 Performance analysis

5.3 Biocompatible, flexible epoxy microneedle

In Chapter 3, replica molding of PI microneedle arrays was demonstrated. Despite the excellent impedance and signal quality outcomes, this process had many serious drawbacks, making it impractical for large scale manufacturing. PI 2610 is a polymer based in a highly volatile solvent, NMP. As a result, the PI must be settled, and the NMP slowly evaporated in vacuum-then-bake cycles in order to mold high quality needles. Unfortunately, this process is extremely sensitive to ambient temperature and other variables out of the control of a basic laboratory environment. Many air bubbles remained in a significant number of samples resulting in low yield. Even from the high-quality needles, the thickness of the PI backing varied between 100 μ m to 1mm, due to manual deposition of PI in layers. There is potential for such a process to be automated, optimizing for exact depositions in highly controlled air pressure and temperature enclosures, but that process would be highly costly and impractical. Another major problem is that baking PI in the PDMS molds destroys the molds, with the molds only usable for three cycles; needle quality diminishing each cycle. Additionally, the process is difficult to parallelize due to requirement of specialized processes like plasma treatment. Needle quality is highly variable with a yield of less than 50%.

To resolve this problem, a new needle material was acquired with similar mechanical properties to PI but optimized for replica molding. An epoxy (EP4CL-80MED, Master Bond Inc.) was selected due to its excellent mechanical properties, and its ISO 10993-5 compliance, designed for biomedical applications. Additionally, this epoxy was compared with another epoxy on hand (EpoxAcast 670 HT) for a low-cost alternative. The use of an epoxy greatly simplified the fabrication process, as the molds only must be filled once and cured at 90°C for 2 hours. Additionally, due to its low temperature curing process the lifespan of the PDMS molds may be extended. With the improved process, small 7x7mm squares of 0.5 mil thick PI sheets were cut, and an excess quantity of EP4CL epoxy was placed in the PDMS molds. A square PI sheet and plunger weight was added on top and compressed in order to fill the PDMS mold cavity and push out excess epoxy, leaving only the thin PI backing.

5.3.1 Performance analysis

The EP4CL is a unique 1-part epoxy system that demonstrates strong mechanical properties including tensile strength of 6500 psi, and a tensile modulus of over 450,000 psi. Additionally, it features a Shore hardness rating of around 95, making it an excellent alternative to PI. Additionally, it has a relatively low viscosity (50-150 cPs) at room temperature, making it easier to handle and work with, when compared with conventional 2-part epoxies like EpoxAcast. Finally, the most significant improvement over PI is the short fabrication time, with the needles capable of finalization after a low temperature cure of 60 minutes at 80-85°C. Lastly, it features a linear shrinkage of less than 0.5%, whereas PI contracts significantly during the hard baking process.

As a result of the improved design, the microneedle portion retained low impedance density of $9.5 \pm 1.6 \text{ k}\Omega\text{-cm}^2$ averaged across all subjects, similar in performance to the PI-based needles $9.7 \pm 3.3 \text{ k}\Omega\text{-cm}^2$. The primary advantage to the epoxy is the high yield and lower cost due to longer mold lifespan. However, EP4CL-80MED is significantly more brittle than PI-based needles, and therefore is only capable of a bending radius of 8.0 before fracturing. A summary comparing different microneedle electrodes to conventional cup and paste electrode are shown in Table 12.

Table 12. Comparison of electrode characteristics used in testing.

Needle type	Yield	Biocompatibility	Flexibility (radius of curvature)	Impedance Density ($\text{k}\Omega\text{-cm}^2$)
Conventional cup/paste	N/A	Good	None	37.6 ± 10.7 , changes over time
PI-2610	42%	Excellent[93]	5.0 mm	9.7 ± 3.3 , consistent
Epoxacast 670 HT	80%	Poor	Not flexible	26.0 ± 7.6 , consistent
EP4CL- 80MED	96%	Excellent	8.0 mm	9.5 ± 1.6 , consistent

5.4 Results

Accuracy performance from the system demonstrates high SNR and significantly improved classification accuracy over the conventional EEG electrodes. We demonstrate the feasibility of using customizable stimuli for a virtual reality-based interface by recording 33-class SSVEP from 6 human subjects. Subjects were asked to sit comfortably and wear the VR headset and await instruction. Then the stimuli were presented to the subject at regular intervals where the subject would glance at each of them in turn. An overview of the setup is shown in Figure 49A, with the top row of flexible microneedle electrodes residing under a thin headband, and the lower row residing below the strap of

the VR headset. A screenshot of the SSVEP-based keyboard in the VR environment is shown in Figure 49B. A closeup of the epoxy-based microneedle electrode is presented in Figure 49C. Closeups of the behavior of the stretchable tangle-resistant interconnect is shown in Figure 49D. Finally, the same *Skintronics* EEG devices used in Chapter 3 is used again in this project due to its small footprint, versatility and high SNR.

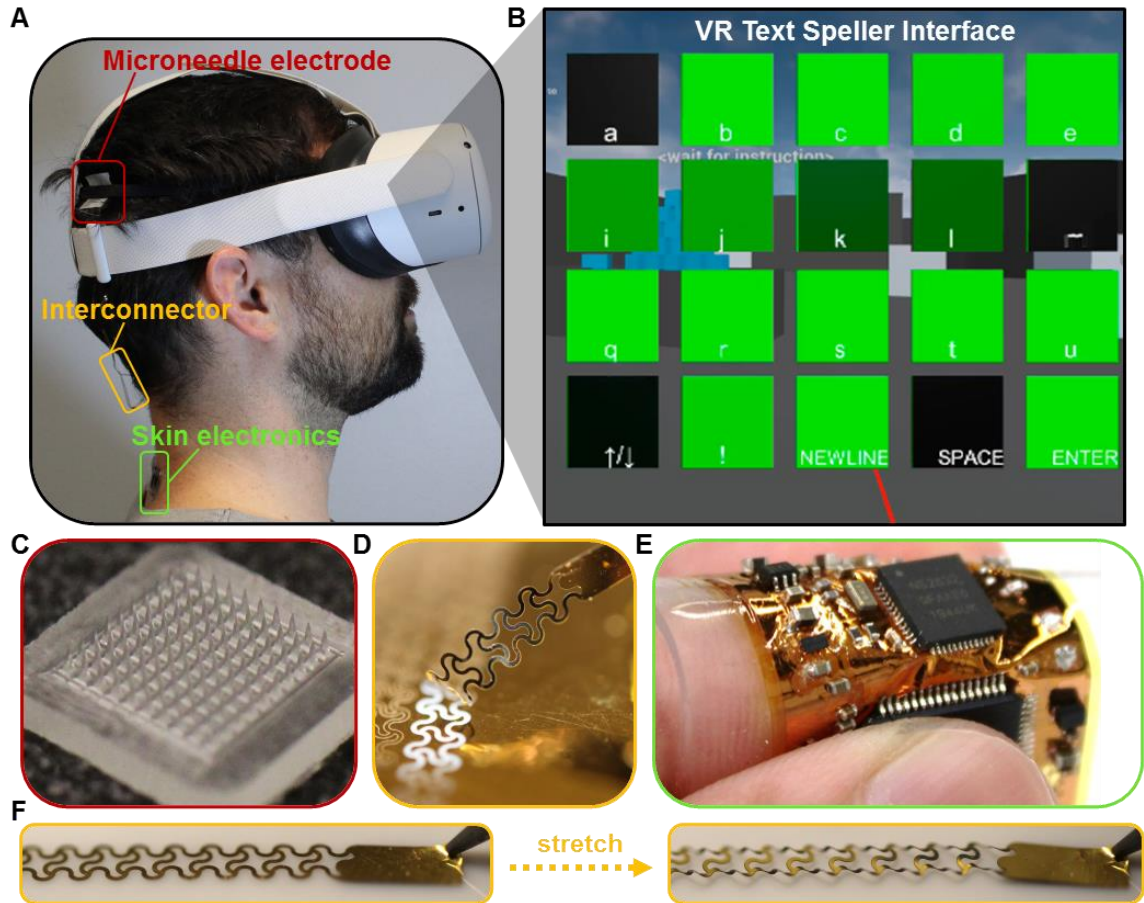


Figure 49. Overview of refined *Skintronics* system. (A) Subject wearing *Skintronics* EEG interface and VR headset. (B) Cropped screenshot of VR text speller interface (C) closeup of new epoxy microneedle electrode (uncoated). (D) closeup of tangle-resistant interconnector peeling from substrate. (E) closeup photo showing *Skintronics* EEG flexibility. (F) demonstration stretching from relaxed state (left) to 40% strain on interconnector (right).

The completed experimental setup involves the *Skintronics* device placed at the back of the neck, as seen in Figure 49. The stretchable interconnects are routed from the EEG under and around the VR headset to the electrodes on the scalp. The placement of the electrodes is meant to target each hemisphere of the brain in order to measure signals biased to one side (due to the per-eye stimulus system). Electrode placement with relative positions based on the 10-10 system are shown in Figure 50. These positions were selected based on the anatomy and the fact that for some of the stimuli each eye would be

viewing a different stimulus, therefore it was important for the setup to have a bilateral setup, where certain channels can measure data from the center outwards, which are more center-biased, and some channels that measure exclusively to one hemisphere, and hence left- or right-biased.

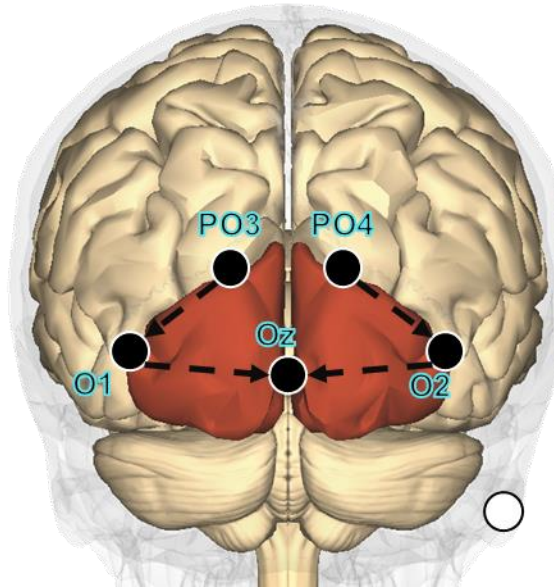


Figure 50. Relative electrode positions of 4-channel bilateral SSVEP setup.

For classification, the same Spatial-CNN architecture was used from the motor imagery project (See Chapter 3), adjusted for 4-channel input and shorter input lengths. An illustration of this architecture and its hidden layers are presented in Figure 51.

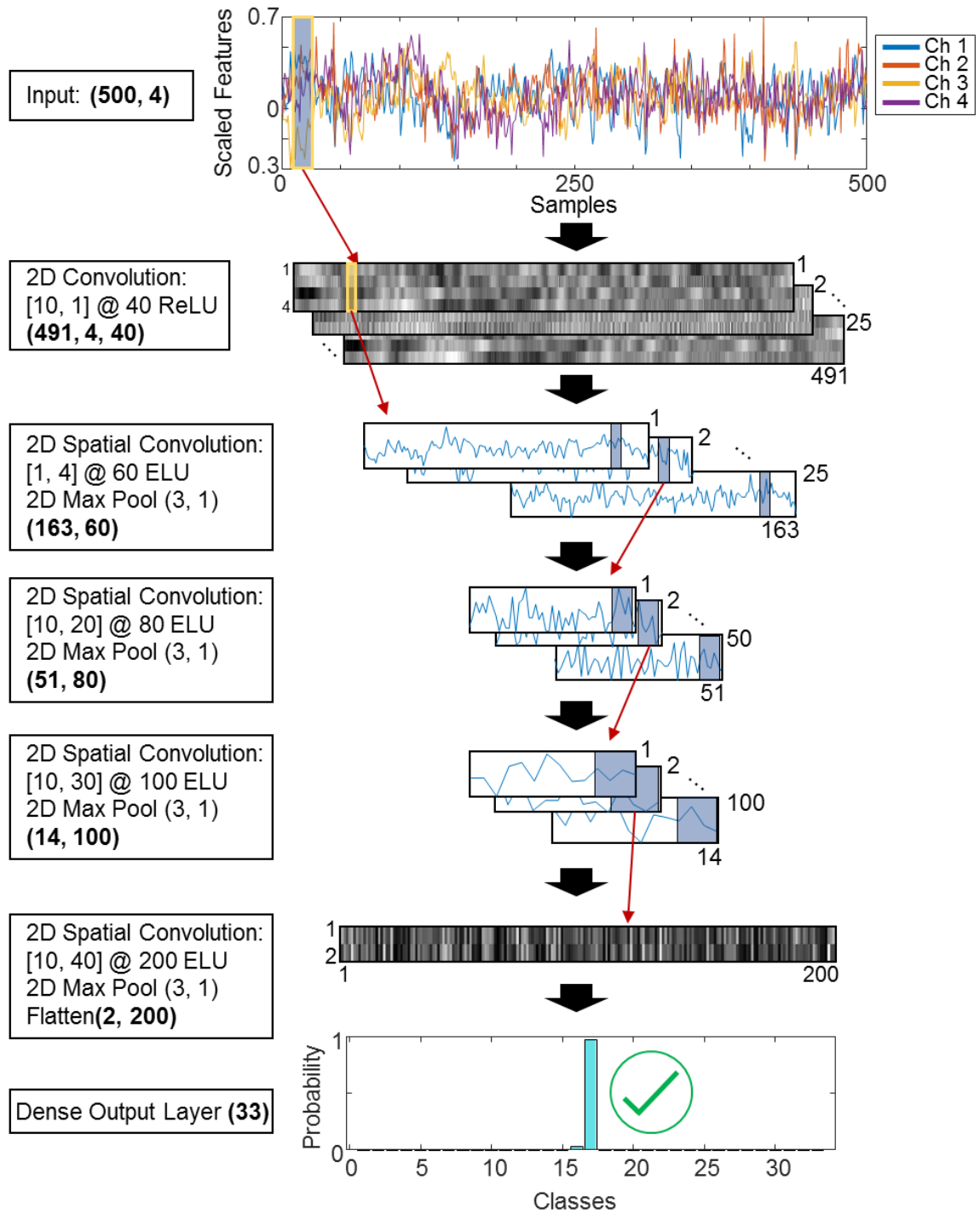


Figure 51. Spatial-CNN architecture and revealed hidden layers, as well as output demonstrating accurate classification from a 33-class dataset.

Data recorded with this setup from 6 subjects demonstrates an average accuracy of $91.07 \pm 0.63\%$ with 1-second windows, resulting in an information transfer rate of

249.7 \pm 4.4 bits/min. This ranks among the highest throughputs in the current published literature as shown in Table 13. The overall results are shown in

Table 14.

Table 13. Comparison of information transfer rate (ITR) between the new VR-based SKINTRONICS and reported values.

	Year	Accuracy (%)	Length (sec)	# of classes	# of channels	ITR (bits/min)
<i>This work (SKINTRONICS)</i>	2021	91.19	1.00	33	4	250.5 \pm 3.2
Mahmood et al. [58]	2019	94.54	0.94	5	2	122.1 \pm 3.53
Nakanishi et al. [87]	2018	89.83	0.8	40	9	325.33 \pm 38.17
Chen et al. [88]	2015	91.09	1	40	9	270.0 \pm 61.8
Bevilacqua et al. [89]	2014	95.61	2	3	4	38.44*
Kwak et al. [20]	2017	99.19	2	5	8	67.13*
Volosyak et al. [90]	2011	96.79	2	5	8	61.70 \pm 32.68
Lin et al. [91]	2007	73.00	1.5	9	8	60.74*
Bin et al. [92]	2009	95.30	2	5	8	58.6 \pm 9.6
Wang et al. [94]	2010	97.20	3.08	16	10	72.2

Table 14. Overall results from 33-class VR-text speller directed training task.

Subject	1	2	3	4	Mean	ITR (bits/min)
S1	97.36%	93.56%	92.46%	90.64%	93.50%	262.4
S2	90.53%	96.71%	87.11%	93.33%	91.92%	254.1
S3	88.88%	90.76%	93.31%	90.91%	90.97%	249.3
S4	94.41%	90.18%	86.76%	88.91%	90.07%	244.8
S5	92.27%	86.57%	88.75%	90.41%	89.50%	242.1
Average					91.19 \pm 1.42%	250.5 \pm 3.2

5.5 Conclusion

The goals of this project were to attempt to maximize throughput of an SSVEP-based BMI by optimization of various components from prior work. Several major limitations from the first two projects were identified. Materials and processes were developed in order to resolve these issues. Overall, the system achieved very high information throughput thanks to its use of innovative combination of flexible electronics and clever use of VR stimulus setup. As shown in Table 13, our system ranks among the best SSVEP-based BMIs. Examples demonstrating superior information transfer rates are based on conventional benchtop EEG systems with twice as many electrodes and highly synchronized, purpose-built stationary systems. Our *Skintronics* systems offers the portability and VR reality interface to accomplish virtually any task. There is great potential for VR environments to rehabilitate individuals with LIS and allow them to freely interact with others by their own will, and to browse the internet freely (see mock-up in Figure 52).

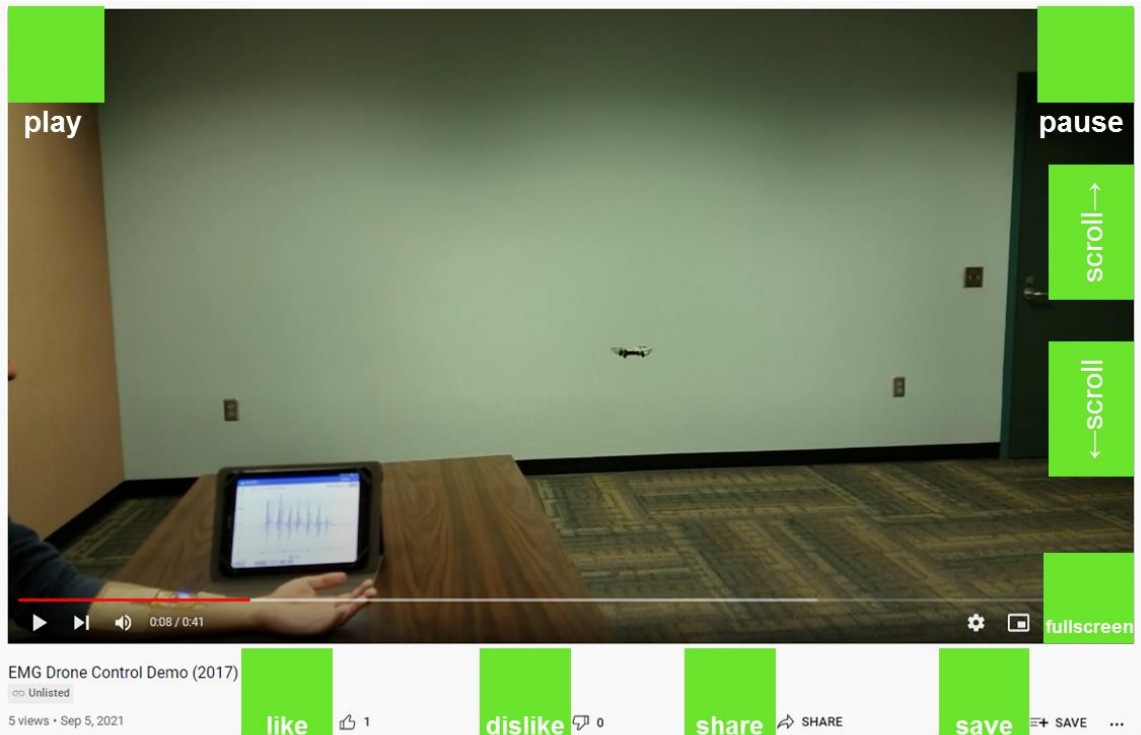


Figure 52. User interface demonstrating a potential use for an SSVEP-based BMI, allowing a user to browse the web through their VR headset; in this example, watching a video online.

The ability to freely interact with the internet and other people on their own command can provide much needed feelings of control, resulting in improved quality of life for individuals afflicted with LIS.

FUTURE WORK

6.1 Summary and original contribution

This thesis demonstrates a significant advancement in the state of non-invasive brain-machine interfaces. The combination of flexible, hybrid electronics (*Skintronics*) allows for comfortable capture of high-quality signals from the scalp. Multiple setups show high SNR when compared with conventional EEG and conventional electrode setups. In the first study, a combination of a VR immersive environment is used with animated visuals to allow for improved motor imagination, and therefore improved BMI literacy. In the next study, we introduced a novel wheelchair control interface using an entirely flexible EEG setup. In the final study, we expanded upon the prior work, and created a VR-based text speller interface with a total of 33 targets. The demonstration of this interface shows the advantages of a fully mobile system with many potential applications. Overall, many novelties were introduced by my research over these three projects, which are listed in the following sections.

6.1.1 *Novelties – Overall*

1. First fully flexible and skin-wearable EEG system, with all individual components being flexible, skin-friendly and compliant, including dry electrodes and stretchable interconnects while also demonstrating resistance to environment noise and motion artefacts.

2. First published data demonstrating performance advantage of fully flexible wearable *Skintronics* interface over conventional rigid EEG and gel- or paste-based electrodes.
3. Laser-cut interconnects for rapid fabrication of electronics with low layer-complexity, such as stretchable interconnects used in Chapters 3 and 5.

6.1.2 *Novelties – Chapter 3*

1. First development and demonstration of an immersive training environment to boost subject BMI performance, along with a video game test environment that provides audio-visual feedback of user performance and accuracy.
2. Highly accurate CNN classification system based on spatial convolutions for a small number (6) of channels using minimal signal preprocessing, resulting in highly competitive information throughputs among published MI-based BMIs.
3. Novel use of input perturbation for reducing channels with minimal classification performance penalty.

6.1.3 *Novelties – Chapter 4*

1. First published use of fully flexible and dry-electrode based BMI, where all components were skin-wearable, skin-compliant and dry (no gels or pastes).
2. Demonstration of highly accurate classification using simple CNN optimized using a grid-search process.
3. First demonstration of highly accurate real-time control of wheelchair interface with SSVEP-based fully flexible BMI.

4. Novel use of hidden-layer analysis towards generating topographical EEG mappings and selecting optimal channels.

6.1.4 *Novelties – Chapter 5*

1. Implementation of a cloud-based ML pipeline for wearable EEG-based BMI training and classification model deployment.
2. Introducing novel utility of VR headset as a stimulus, presenting different stimuli to each eye simultaneously; effectively doubling stimulus-based information throughput.
3. Development of immersive VR-based stimulus and video game environments for subject training and testing.
4. Method for rapid fabrication of fully insulated ultrathin stretchable interconnects based on tangle-resistant design.

6.1.5 *Future Direction*

The Future of Flexible Electronics Fabrication

The future of flexible electronics fabrication appears promising. In the last few years, we have seen a large increase in productivity in this field, and the trend appears to be increasing. New methods for rapid prototyping such as inkjet and aerosol-jet printing, screen printing, as well as femtosecond laser cutting are just a few new methods aimed at tackling the financial and time costs of cleanroom-based processes (see Figure 53).

As mentioned in this dissertation, aerosol-jet printing offers the ability to print a variety of materials using inks with a range of viscosities. This additive process saves

much time, and a single machine can be used to print fully functional multilayer circuits[95]. Laser etching also allows for high speed etching of materials, even with complex three-dimensional geometries. This thesis demonstrated one example of a potential use case in the printing of flexible and stretchable multilayer interconnectors. Inkjet printing offers methods for deposition of inks like AJP, but deposits droplets based on drop properties only. Nozzles and inks are typically designed together, and a range of materials can be printed including PI, silver nanoparticle or nanowires, Cu, graphene, CNTs and more. This process is typically faster than AJP and may be useful for high throughput production beyond the prototyping stage. Overall, with an increasing toolkit, the fabrication of flexible devices will become easier and faster over time.

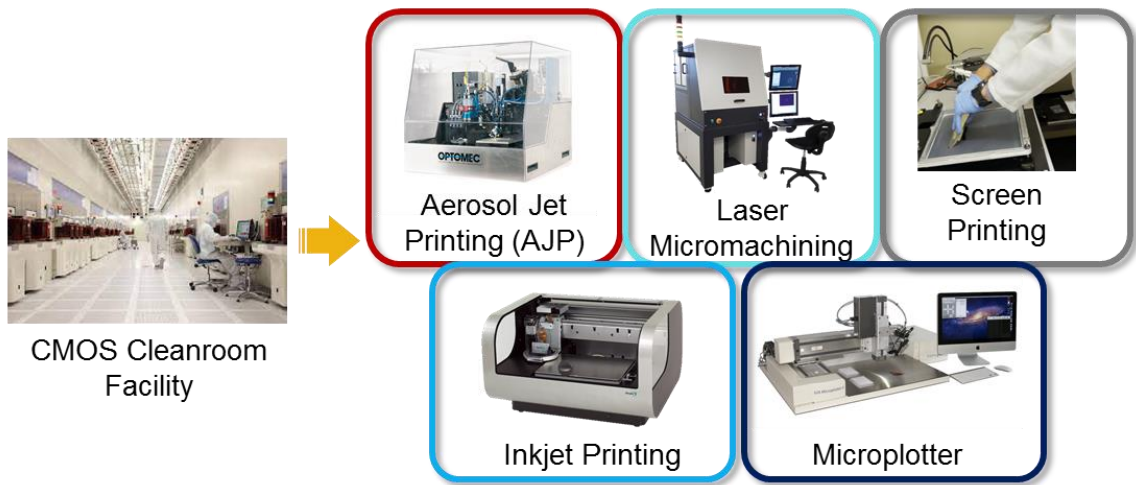


Figure 53. Proposed advanced manufacturing techniques for future *Skintronics*-type and flexible hybrid electronics.

The Future of BMI

As mentioned in the literature review chapter, non-invasive brain-machine interfaces suffer from intrinsic problems related to signal acquisition, primarily due to the inverse square law and poor spatial resolution and lack of depth resolution. These

problems can be approached using dense EEG arrays with smaller needle-based electrodes with very low impedance with better surface spatial resolution and advanced algorithms and statistical models to attempt to reconstruct greater information. However, for the purposes of minimalist, practical wearable EEG setups, this is becoming less and less likely. Additionally, no algorithm or statistical model can make up for the complete loss and mixing of low amplitude signals crucial to BMI functionality. Additionally, many brain signals and action potentials occur in frequency ranges outside of what can be reasonably sampled using a small, wearable multichannel system. It is worth noting that most companies currently developing BMIs are doing so using some type of implanted devices as seen in the Table 15 below. This is not a surprise, due to the limitations mentioned previously.

Table 15. Select Companies Developing BMIs and related technologies. Bold text indicates an implanted device. Adapted from Smalley[96].

Company Name	Device	Type	Status
CorTec	AirRay	ECoG implant	FDA Approved
Blackrock Microsystems	Utah Array	Intracortical implant	FDA Approved
Ad-Tech Medical	Epilepsy/LTM	ECoG implant	FDA Approved
Synchron	Stentrode	Intravascular implant	Early clinical feasibility study (ongoing)
NeuroNexus Technologies	Matrix Array	Intracortical implant	Preclinical
Iota Biosciences	Neural dust	Wireless microimplants	Preclinical
Neuroolutions	IpsiHand	EEG	Clinical

Additionally, implants are more logical for patients who have life-long illnesses like LIS, as it makes far more sense to develop an implanted system that can provide functionality over an extended time period. Cost-benefit analyses will vary depending on

severity of illness and how rapidly the technology improves. It is possible that non-invasive EEG may become obsolete with the rise of small minimally invasive implants such as the stent implant from *Synchron*.

APPENDIX

A.1 Calculation of Information Transfer Rate

BMIs are generally assessed based on their information transfer rate (ITR), measured in bits/min and their classification accuracy.[97] ITR is calculated as follows:

$$ITR = \left(\log_2 N + A \log_2 A + (1 - A) \log_2 \left(\frac{1 - A}{N - 1} \right) \right) \times \left(\frac{60}{w} \right) \frac{\text{bits}}{\text{min}}$$

where N is the number of targets, A is the accuracy, and w is the combined size of the classified windows in seconds, and the gaze shift time[98].

A.2 Topographic Scalp Mapping using Deep Learning

When using as few as two EEG data channels (3 measurement electrodes), it is important to verify that the electrode locations are optimal for that subject. Therefore, 4-class SSVEP examinations were undertaken with a 32-channel EEG (ActiveTwo System, Biosemi B.V., Amsterdam), with setup shown in Figure 30A. A convolutional neural network (CNN) is then trained to classify the data. From the trained network, relevant weights correlated to information presence may be extracted and associated to specific channels. Electrode placement is then decided based on the channel locations with the most significant weights. The architecture used is a 2-layer deep convolutional neural, 2-*CNN-Mapping*, with max pooling using only vector kernels. The input was split into epochs of 300 data points (1.172 seconds at 256 Hz). Each epoch was high pass filtered at 4 Hz and normalized from the range of 0 to 1. Therefore, the inputs were 32 channels x 300 data points, and convolutions were performed along the time domain signal to prevent data mixing across channels. The weights are extracted from the feature maps formed in the first convolution layer. The sum of weights of all feature maps was obtained as we have 32 feature maps in the first convolution layer. We used the first convolution layer as the feature maps are still in the same shape as the input before max-pooling. The weights for each feature map were calculated using the following formula. w_l stands for window length, which is 300 and p is the number of channels.

$$W_p = \sum_{q=0}^{q=w_l} w_{(p,q)}, \text{ where } 0 \leq p < 32 \text{ and } 0 \leq q < w_l$$

To get the total weight W for each channel p per participant, we then sum the weights of all feature maps r in the first convolution layer which has 32 feature maps as

expressed in equation: $W = \sum_{r=1}^{32} (W_p)_r$. A resulting scale shows the activation weights for each channel over the 32 feature maps. The topographic maps created from the weights extracted from the trained model shows the regions with highest weights are situated around the virtual cortex region of the human brain. This exercise is meant to be a proof-of-concept method for mapping biopotential signals from a range of sources with the intention of reducing the number of electrodes and amount of data to process.

A.3 Device Fabrication Process

Device fabrication procedure is illustrated in Figure 21 and Figure 33. This process is roughly the same for each *Skintronics* device discussed in Chapters 3-5. Detail procedures involved with device preparation is described here:

a) Microfabrication of the thin-film circuit boards

1. Spincoat PDMS on a cleaned silicon wafer at 3000 rpm for 30 sec.
2. Cure the PDMS-coated wafer on a 150 °C hot plate for 5 min.
3. Perform oxygen plasma treatment to render the PDMS hydrophilic.
4. Spincoat polyimide at 4000 rpm for 1 min and bake in a vacuum oven at 250 °C for 3 hr including ramping steps.
5. Sputter 500 nm copper for the 1st metal layer.
6. Spincoat photoresist (SC1827) at 3000 rpm for 30 sec and bake it on a 110 °C hot plate for 1 min.
7. Expose UV with the 1st metal pattern (ground) using a mask aligner (MA6).
8. Develop the exposed photoresist with developer (MF-319).
9. Etch exposed copper with copper etchant (APS-100, diluted 1:1 with DI water) and strip photoresist.
10. Spincoat polyimide at 850 rpm for 1 min bake in a vacuum oven at 250 °C for 3 hr including ramping steps.
11. Spincoat polyimide at 850 rpm for 1 min bake in a vacuum oven at 250 °C for 3 hr including ramping steps.
12. Spincoat photoresist (AZP4620) at 1000 rpm for 30 sec and bake it on a 95 °C hot plate for 4 min.
13. Expose UV with the 1st via pattern using a mask aligner (MA6).
14. Develop the exposed photoresist with developer (AZ400K, diluted with 4 parts of DI water).
15. Oxygen plasma etch exposed PI using reactive ion etching (Plasma-Therm) and strip photoresist.
16. Sputter 1.5 μm copper for the 2nd metal layer.
17. Spincoat photoresist (AZP462) at 3000 rpm for 30 sec and bake it on a 95 °C hot plate for 4 min.
18. Expose UV with the 2nd metal pattern using a mask aligner (MA6).
19. Develop the exposed photoresist with developer (AZ400K, diluted with 4 parts of DI water).
20. Etch exposed copper with copper etchant (APS-100, diluted 1:1 with DI water) and strip photoresist.
21. Spincoat polyimide at 4000 rpm for 1 min and bake in a vacuum oven at 250 °C for 3 hr including ramping steps.
22. Spincoat photoresist (AZP462) at 2000 rpm for 30 sec and bake it on a 95 °C hot plate for 4 min.
23. Expose UV with the solder pad exposure pattern using a mask aligner (MA6).
24. Develop the exposed photoresist with developer (AZ400K, diluted with 4 parts of DI water).

25. Oxygen plasma etch exposed PI using reactive ion etching (Plasma-Therm) and strip photoresist.
 26. Completed circuits are peeled-off from the PDMS wafer and transferred onto a glass slide for chip assembly.
- b) Flexible circuit board assembly using reflow soldering
1. Openings of the stainless-steel stencil is aligned to the exposed copper pads.
 2. Solder paste is dispensed onto the stencil is dragged across the stencil with a razor blade.
 3. Chip components are placed on the board.
 4. Using a programmable hot plate, the components are reflow soldered by ramping the hot plate from 100 °C to 170 °C at an increment of 10 °C with a 1 min dwell period at each temperature.
 5. Soldered board is rinsed with acetone and isopropyl alcohol and dried with a stream of nitrogen.
 6. The board is detached from the glass slide and is attached to a thin layer of elastomer (Ecoflex).
- c) Dry electrode integration and device encapsulation
1. Flexible film cables are obtained by cutting the cables into individual strips.
 2. PDMS is applied on the backside of the strips, where the conductive trace is exposed, and cured.
 3. Using silver paint, the flexible device and the dry electrode are bonded on the two ends of the cables.
 4. Small amount of epoxy is applied to the tip of the cable on the dry electrode side to enhance the attachment.
 5. Ecoflex is applied on top of the circuit for full device encapsulation.

A.4 Fabrication of Skin Electrodes via Aerosol Jet Printing

Silver skin electrodes were printed using an Aerosol Jet Printer (AJ200, Optomec, Albuquerque, NM). This additive manufacturing process involves depositing polyimide and silver nanoparticle ink in xylene onto a glass slide prepared with spin-coated Polymethyl methacrylate (PMMA A7). The PMMA is then dissolved for 15 minutes in an acetone bath at room temperature, and the finished electrodes are transferred to an elastomer (Ecoflex Gel, Smooth-On, USA) using water-soluble poly-vinyl alcohol (PVA) tape (3M, Maplewood, Minnesota).

Step-by step instructions:

1. Clean glass slide or silicon wafer with acetone and IPA.
2. Plasma clean at 18 W for 30 seconds.
3. Spin coat PMMA in Anisole at 4000 RPM.
4. Bake the 700 nm PMMA at 180 °C for 2.5 minutes.
5. Align sample onto platen stage of the AJ200 and leave platen stage at 70 °C.
6. Change deposition head to 300 µm nozzle.
7. Enable the pneumatic atomizer to print polyimide 2545 5:1 mixture with N-methyl-2-pyrrolidone.
8. Turn on sheath flow rate and 100 SCCM, atomizer flow rate at 1500 SCCM, and exhaust at 1470 SCCM.
9. Print two to five layers of the polyimide patterns at 10 mm/s on the PMMA substrate.
10. Ensure atomization is dense on the side of the pneumatic atomizer.
11. Cure the polyimide at 250°C in an ambient oven for 1 hour.
12. Change deposition head to 150 µm nozzle.
13. Align fiducial markers of the polyimide layer to deposit the silver layer.
14. Enable the ultrasonic bath on the AJ200 at 30°C.
15. Turn on sheath flow rate between 5 SCCM and 30 SCCM.
16. Turn on atomizer flow rate between 15 SCCM and 30 SCCM
17. Turn on atomizer current at .6 Amps.
18. Run the silver ink pattern at 10 mm/s on the polyimide patterns.
19. Sinter the silver ink at 200 °C for 1 hour
20. Place a Texwipe and a glass slide to sandwich the samples for the acetone bath.
21. Place the samples in an acetone bath for 1 hour at 60 °C.
22. Prepare a sheet of PVA by laminating onto a glass slide.

23. Heat treat at 100 °C for 1 minute to remove wrinkles and release stress.
24. Spin coat Ecoflex gel (1:1) at 2000 RPM for 1 min.
25. Let cure at room temperature for 2 hours.
26. Remove the samples from the acetone bath and apply water soluble tape onto the electrodes.
27. Transfer the electrodes onto the Ecoflex gel elastomer and dissolve the tape.
28. Attach anisotropic conductive film (ACF) wires to the electrode pads using silver paint.

A.5 Frequency component analysis with CCA

Canonical correlation analysis (CCA) is a well-established method for decoding SSVEP signals using frequency component analysis[72, 91, 92]. For two multidimensional

random variables, X and Y , and corresponding linear combinations $x = X^T W_x$ and $y = X^T W_y$ CCA generates pairs of linear combinations W_x and W_y , for sets X and Y such that the correlation between the two canonical variables is maximized. CCA may be used to classify where an unlabeled dataset may be classified using ‘template’ datasets for each class. In this case, the unlabeled SSVEP dataset is the recorded training data, and that is compared against template reference signals which is generated using the sine and cosine functions, including only the first and second harmonics.

$$Y_f = \begin{pmatrix} \sin(2\pi ft) \\ \cos(2\pi ft) \\ \sin(2 \cdot 2\pi ft) \\ \cos(2 \cdot 2\pi ft) \end{pmatrix}$$

Therefore, we find the maximum canonical correlation, ρ , with respect to W_x and W_y

$$\max_{W_x, W_y} \rho(x, y) = \frac{E[W_x^T X Y^T W_y]}{\sqrt{E[W_x^T X X^T W_x] E[W_y^T Y Y^T W_y]}}.$$

To determine the output class, we find the index of the maximum correlation from ρ :

$$y_{fit} = \underset{i}{\operatorname{argmax}} \rho_i, \quad i = 0, 1, 2, \dots, K$$

where classes i correspond to frequencies from reference signals f_0, f_1, \dots, f_K . [91, 92]

REFERENCES

1. Padfield, N., et al., *EEG-based brain-computer interfaces using motor-imagery: Techniques and challenges*. Sensors, 2019. **19**(6): p. 1423.
2. Pels, E.G., et al., *Estimated prevalence of the target population for brain-computer interface neurotechnology in the Netherlands*. Neurorehabilitation and neural repair, 2017. **31**(7): p. 677-685.
3. Lin, C.T., et al., *Review of wireless and wearable electroencephalogram systems and brain-computer interfaces--a mini-review*. Gerontology, 2010. **56**(1): p. 112-9.
4. Norton, J.J.S., et al., *Soft, curved electrode systems capable of integration on the auricle as a persistent brain-computer interface*. Proceedings of the National Academy of Sciences, 2015. **112**(13): p. 3920-3925.
5. Salvo, P., et al., *A 3D printed dry electrode for ECG/EEG recording*. Sensors and Actuators A: Physical, 2012. **174**: p. 96-102.
6. Stauffer, F., et al., *Skin Conformal Polymer Electrodes for Clinical ECG and EEG Recordings*. Adv Healthc Mater, 2018. **7**(7): p. e1700994.
7. Li, G., S. Wang, and Y.Y. Duan, *Towards gel-free electrodes: A systematic study of electrode-skin impedance*. Sensors and Actuators B: Chemical, 2017. **241**: p. 1244-1255.
8. Tallgren, P., et al., *Evaluation of commercially available electrodes and gels for recording of slow EEG potentials*. Clin Neurophysiol, 2005. **116**(4): p. 799-806.
9. Ahmmed, K., C. Grambow, and A.-M. Kietzig, *Fabrication of micro/nano structures on metals by femtosecond laser micromachining*. Micromachines, 2014. **5**(4): p. 1219-1253.
10. Mishra, S., et al., *Soft, wireless periocular wearable electronics for real-time detection of eye vergence in a virtual reality toward mobile eye therapies*. Science advances, 2020. **6**(11): p. eaay1729.
11. Wilkinson, N., et al., *A review of aerosol jet printing—a non-traditional hybrid process for micro-manufacturing*. The International Journal of Advanced Manufacturing Technology, 2019. **105**(11): p. 4599-4619.
12. Kim, P., et al., *Soft lithography for microfluidics: a review*. 2008.

13. Mahmood, M., et al., *Wireless Soft Scalp Electronics and Virtual Reality System for Motor Imagery-based Brain-Machine Interfaces*. Advanced Science, 2021.
14. Zhu, M., et al., *Haptic-feedback smart glove as a creative human-machine interface (HMI) for virtual/augmented reality applications*. Science Advances, 2020. **6**(19): p. eaaz8693.
15. Krizhevsky, A., I. Sutskever, and G.E. Hinton, *Imagenet classification with deep convolutional neural networks*. Advances in neural information processing systems, 2012. **25**: p. 1097-1105.
16. Schirrneister, R.T., et al., *Deep learning with convolutional neural networks for EEG decoding and visualization*. Human brain mapping, 2017. **38**(11): p. 5391-5420.
17. Smith, E. and M. Delargy, *Locked-in syndrome*. Bmj, 2005. **330**(7488): p. 406-409.
18. Graimann, B., et al., *Visualization of significant ERD/ERS patterns in multichannel EEG and ECoG data*. Clinical neurophysiology, 2002. **113**(1): p. 43-47.
19. Bager, F., et al., *Comparison of EEG and ECoG for detecting cerebrocortical activity during slaughter of calves*. Meat Science, 1990. **27**(3): p. 211-225.
20. Kwak, N.S., K.R. Muller, and S.W. Lee, *A convolutional neural network for steady state visual evoked potential classification under ambulatory environment*. PLoS One, 2017. **12**(2): p. e0172578.
21. y Alvarez, G.D., et al., *Wireless EEG System Achieving High Throughput and Reduced Energy Consumption Through Lossless and Near-Lossless Compression*. IEEE transactions on biomedical circuits and systems, 2018. **12**(1): p. 231-241.
22. Lin, C.-T., et al., *A Wireless Multifunctional SSVEP-Based Brain Computer Interface Assistive System*. IEEE Transactions on Cognitive and Developmental Systems, 2018.
23. Nakanishi, M., et al., *Enhancing detection of SSVEPs for a high-speed brain speller using task-related component analysis*. IEEE Transactions on Biomedical Engineering, 2017. **65**(1): p. 104-112.
24. Kim, Y.S., et al., *All-in-One, wireless, stretchable hybrid electronics for smart, connected, and ambulatory physiological monitoring*. Advanced Science, 2019. **6**(17): p. 1900939.
25. Yeo, W.H., et al., *Multifunctional epidermal electronics printed directly onto the skin*. Advanced materials, 2013. **25**(20): p. 2773-2778.

26. Rodeheaver, N., et al., *Strain-Isolating Materials and Interfacial Physics for Soft Wearable Bioelectronics and Wireless, Motion Artifact-Controlled Health Monitoring*. Advanced Functional Materials, 2021. **31**(36): p. 2104070.
27. Das, J.M., K. Anosike, and R.M.D. Asuncion, *Locked-in Syndrome*. StatPearls [Internet], 2021.
28. Kim, S., et al., *Thermal impact of an active 3-D microelectrode array implanted in the brain*. IEEE Transactions on Neural Systems and Rehabilitation Engineering, 2007. **15**(4): p. 493-501.
29. Starr, P.A., et al., *Implantation of deep brain stimulators into subthlamic nucleus: technical approach and magnetic imaging—verified electrode locations*. Journal of neurosurgery, 2002. **97**(2): p. 370-387.
30. Sellers, E.W., T.M. Vaughan, and J.R. Wolpaw, *A brain-computer interface for long-term independent home use*. Amyotrophic lateral sclerosis, 2010. **11**(5): p. 449-455.
31. Lebedev, M.A. and M.A. Nicolelis, *Brain-machine interfaces: past, present and future*. TRENDS in Neurosciences, 2006. **29**(9): p. 536-546.
32. Konrad, P. and T. Shanks, *Implantable brain computer interface: Challenges to neurotechnology translation*. Neurobiology of disease, 2010. **38**(3): p. 369-375.
33. Allison, B.Z., A. Kübler, and J. Jin, *30+ years of P300 brain-computer interfaces*. Psychophysiology, 2020. **57**(7): p. e13569.
34. Jin, J., et al., *A P300 brain-computer interface based on a modification of the mismatch negativity paradigm*. International journal of neural systems, 2015. **25**(03): p. 1550011.
35. Herrmann, C.S., *Human EEG responses to 1–100 Hz flicker: resonance phenomena in visual cortex and their potential correlation to cognitive phenomena*. Experimental brain research, 2001. **137**(3): p. 346-353.
36. Wolpaw, J.R., et al., *Brain-computer interfaces for communication and control*. Clinical neurophysiology, 2002. **113**(6): p. 767-791.
37. Pun, T., et al., *Brain-computer interaction research at the Computer Vision and Multimedia Laboratory, University of Geneva*. IEEE Transactions on Neural Systems and Rehabilitation Engineering, 2006. **14**(2): p. 210-213.
38. Sharma, N., V.M. Pomeroy, and J.-C. Baron, *Motor imagery: a backdoor to the motor system after stroke?* Stroke, 2006. **37**(7): p. 1941-1952.
39. Johnson, S.H., *Imagining the impossible: intact motor representations in hemiplegics*. Neuroreport, 2000. **11**(4): p. 729-732.

40. Daly, J.J. and J.R. Wolpaw, *Brain-computer interfaces in neurological rehabilitation*. The Lancet Neurology, 2008. **7**(11): p. 1032-1043.
41. Ramos-Murguialday, A., et al., *Proprioceptive feedback and brain computer interface (BCI) based neuroprostheses*. 2012.
42. Gomez-Rodriguez, M., et al., *Closing the sensorimotor loop: haptic feedback facilitates decoding of motor imagery*. Journal of neural engineering, 2011. **8**(3): p. 036005.
43. Allison, B.Z. and C. Neuper, *Could anyone use a BCI?*, in *Brain-computer interfaces*. 2010, Springer. p. 35-54.
44. Halder, S., et al., *Prediction of P300 BCI aptitude in severe motor impairment*. PloS one, 2013. **8**(10): p. e76148.
45. Chepesiuk, R., *Where the chips fall: environmental health in the semiconductor industry*. Environmental health perspectives, 1999. **107**(9): p. A452-A457.
46. Wang, Y., J. Bokor, and A. Lee, *Maskless lithography using drop-on-demand inkjet printing method*. 2004. p. 628-636.
47. Xu, B.L., et al., *Aerosol Jet Printing on Radio Frequency IDentification Tag Applications*. Key Engineering Materials, 2013. **562-565**: p. 1417-1421.
48. Rahman, M.T., et al., *3D printed high performance strain sensors for high temperature applications*. Journal of Applied Physics, 2018. **123**(2): p. 024501.
49. Yeo, L.Y. and J.R. Friend, *Ultrafast microfluidics using surface acoustic waves*. Biomicrofluidics, 2009. **3**(1): p. 012002.
50. McDonald, J.C., et al., *Fabrication of microfluidic systems in poly (dimethylsiloxane)*. ELECTROPHORESIS: An International Journal, 2000. **21**(1): p. 27-40.
51. Xia, Y., et al., *Replica molding using polymeric materials: A practical step toward nanomanufacturing*. Advanced Materials, 1997. **9**(2): p. 147-149.
52. Weibel, D.B., W.R. DiLuzio, and G.M. Whitesides, *Microfabrication meets microbiology*. Nature Reviews Microbiology, 2007. **5**(3): p. 209-218.
53. Xia, Y. and G.M. Whitesides, *Soft lithography*. Annual review of materials science, 1998. **28**(1): p. 153-184.
54. Jurcak, V., D. Tsuzuki, and I. Dan, *10/20, 10/10, and 10/5 systems revisited: their validity as relative head-surface-based positioning systems*. Neuroimage, 2007. **34**(4): p. 1600-1611.

55. Olatunji, O. and A. Denloye, *Production of hydrogel microneedles from fish scale biopolymer*. Journal of Polymers and the Environment, 2019. **27**(6): p. 1252-1258.
56. Römgens, A., et al., *Monitoring the penetration process of single microneedles with varying tip diameters*. journal of the mechanical behavior of biomedical materials, 2014. **40**: p. 397-405.
57. Russo, S., et al., *Soft and stretchable sensor using biocompatible electrodes and liquid for medical applications*. Soft robotics, 2015. **2**(4): p. 146-154.
58. Mahmood, M., et al., *Fully portable and wireless universal brain-machine interfaces enabled by flexible scalp electronics and deep learning algorithm*. Nature Machine Intelligence, 2019. **1**(9): p. 412-422.
59. Yang, H., et al. *On the use of convolutional neural networks and augmented CSP features for multi-class motor imagery of EEG signals classification*. in *2015 37th Annual International Conference of the IEEE Engineering in Medicine and Biology Society (EMBC)*. 2015. IEEE.
60. Tang, Z., C. Li, and S. Sun, *Single-trial EEG classification of motor imagery using deep convolutional neural networks*. Optik, 2017. **130**: p. 11-18.
61. Chaudhary, S., et al., *Convolutional neural network based approach towards motor imagery tasks EEG signals classification*. IEEE Sensors Journal, 2019. **19**(12): p. 4494-4500.
62. Welch, P., *The use of fast Fourier transform for the estimation of power spectra: a method based on time averaging over short, modified periodograms*. IEEE Transactions on audio and electroacoustics, 1967. **15**(2): p. 70-73.
63. Zhang, R., et al., *A novel hybrid deep learning scheme for four-class motor imagery classification*. Journal of neural engineering, 2019. **16**(6): p. 066004.
64. Tabar, Y.R. and U. Halici, *A novel deep learning approach for classification of EEG motor imagery signals*. Journal of neural engineering, 2016. **14**(1): p. 016003.
65. Lu, N., et al., *A deep learning scheme for motor imagery classification based on restricted boltzmann machines*. IEEE transactions on neural systems and rehabilitation engineering, 2016. **25**(6): p. 566-576.
66. Shi, Z., et al., *Silk-Enabled Conformal Multifunctional Bioelectronics for Investigation of Spatiotemporal Epileptiform Activities and Multimodal Neural Encoding/Decoding*. Advanced Science, 2019. **6**(9): p. 1801617.

67. Schlogl, A., et al. *Information transfer of an EEG-based brain computer interface.* in *Neural Engineering, 2003. Conference Proceedings. First International IEEE EMBS Conference on.* 2003. IEEE.
68. Xu, J. and B. Zhong, *Review on portable EEG technology in educational research.* Computers in Human Behavior, 2018. **81**: p. 340-349.
69. Shi, M., et al. *Towards portable SSVEP-based brain-computer interface using Emotiv EPOC and mobile phone.* in *Advanced Computational Intelligence (ICACI), 2018 Tenth International Conference on.* 2018. IEEE.
70. Chen, X., et al., *Control of a 7-DOF Robotic Arm System With an SSVEP-Based BCI.* International journal of neural systems, 2018: p. 1850018.
71. Chi, Y.M., et al. *A practical mobile dry EEG system for human computer interfaces.* in *International Conference on Augmented Cognition.* 2013. Springer.
72. Bin, G., et al., *The SSVEP topographic scalp maps by canonical correlation analysis.* Conf Proc IEEE Eng Med Biol Soc, 2008. **2008**: p. 3759-62.
73. Delorme, A. and S. Makeig, *EEGLAB: an open source toolbox for analysis of single-trial EEG dynamics including independent component analysis.* J Neurosci Methods, 2004. **134**(1): p. 9-21.
74. Mishra, S., et al., *Soft, conformal bioelectronics for a wireless human-wheelchair interface.* Biosensors and Bioelectronics, 2017. **91**: p. 796-803.
75. Lee, Y., et al., *Wireless, intraoral hybrid electronics for real-time quantification of sodium intake toward hypertension management.* Proc Natl Acad Sci U S A, 2018.
76. Bideaux, A., et al., *Synchronization in wireless biomedical-sensor networks with Bluetooth Low Energy.* Current Directions in Biomedical Engineering, 2015. **1**(1): p. 73-76.
77. Mullen, T.R., et al., *Real-time neuroimaging and cognitive monitoring using wearable dry EEG.* IEEE Transactions on Biomedical Engineering, 2015. **62**(11): p. 2553-2567.
78. Goldman, R.I., et al., *Simultaneous EEG and fMRI of the alpha rhythm.* Neuroreport, 2002. **13**(18): p. 2487-92.
79. Wang, Y., et al., *Brain-computer interface based on the high-frequency steady-state visual evoked potential,* in *Proceedings. 2005 First International Conference on Neural Interface and Control, 2005.* 2005. p. 37-39.

80. Chi, Y.M. and G. Cauwenberghs, *Micropower non-contact EEG electrode with active common-mode noise suppression and input capacitance cancellation*. Conf Proc IEEE Eng Med Biol Soc, 2009. **2009**: p. 4218-21.
81. Chi, Y.M., T.P. Jung, and G. Cauwenberghs, *Dry-contact and noncontact biopotential electrodes: methodological review*. IEEE Rev Biomed Eng, 2010. **3**: p. 106-19.
82. Winter, B.B. and J.G. Webster, *Driven-right-leg circuit design*. IEEE Transactions on Biomedical Engineering, 1983. **BME-30**(1): p. 62-66.
83. *Electroencephalography: basic principles, clinical applications, and related fields*. 2005: Lippincott Williams & Wilkins.
84. Krizhevsky, A., I. Sutskever, and G.E. Hinton, *Imagenet classification with deep convolutional neural networks*. Advances in Neural Information Processing Systems, 2012.
85. Kingma, D.P. and J. Ba *Adam: A Method for Stochastic Optimization*. ArXiv e-prints, 2014.
86. Ji, Y., J. Hwang, and E.Y. Kim, *An intelligent wheelchair using situation awareness and obstacle detection*. Procedia-social and behavioral sciences, 2013. **97**: p. 620-628.
87. Nakanishi, M., et al., *Enhancing Detection of SSVEPs for a High-Speed Brain Speller Using Task-Related Component Analysis*. IEEE Trans Biomed Eng, 2018. **65**(1): p. 104-112.
88. Chen, X., et al., *High-speed spelling with a noninvasive brain-computer interface*. Proc Natl Acad Sci U S A, 2015. **112**(44): p. E6058-67.
89. Bevilacqua, V., et al., *A novel BCI-SSVEP based approach for control of walking in Virtual Environment using a Convolutional Neural Network*. Proceedings of the 2014 International Joint Conference on Neural Networks (Ijcn), 2014: p. 4121-4128.
90. Volosyak, I., *SSVEP-based Bremen-BCI interface--boosting information transfer rates*. J Neural Eng, 2011. **8**(3): p. 036020.
91. Lin, Z., et al., *Frequency recognition based on canonical correlation analysis for SSVEP-based BCIs*. IEEE Trans Biomed Eng, 2007. **54**(6 Pt 2): p. 1172-6.
92. Bin, G., et al., *An online multi-channel SSVEP-based brain-computer interface using a canonical correlation analysis method*. J Neural Eng, 2009. **6**(4): p. 046002.

- 93. Constantin, C.P., et al., *Biocompatibility of polyimides: A mini-review*. Materials, 2019. **12**(19): p. 3166.
- 94. Wang, Y., Y.T. Wang, and T.P. Jung, *Visual stimulus design for high-rate SSVEP BCI*. Electronics Letters, 2010. **46**(15).
- 95. Kwon, Y.-T., et al., *All-printed nanomembrane wireless bioelectronics using a biocompatible solderable graphene for multimodal human-machine interfaces*. Nature communications, 2020. **11**(1): p. 1-11.
- 96. Smalley, E., *The business of brain-computer interfaces*. Nat. Biotechnol., 2019. **37**(9): p. 978.
- 97. Obermaier, B., et al., *Information transfer rate in a five-classes brain-computer interface*. IEEE Trans Neural Syst Rehabil Eng, 2001. **9**(3): p. 283-8.
- 98. Shannon, C.E. and W. Weaver, *The mathematical theory of information*. 1949.